Suppression of Fine Ash Formation in Pulverized Coal Flames

DOE Grant No. DE-FG22-92PC92548

Period of Performance: September 30, 1992 to January 31, 1996

Final Technical Report

We have no objection from a patent standpoint to the publication or dissemination of this material.

Mark P. Dvorscak Aug 6 1996

Office of Intellectual Property Counsel
DOE Field Office, Chicago

Date

Prepared by:

JOHN C. KRAMLICH
BLAKE CHENEVERT
JUNGSUNG PARK
DAVID A. HOFFMAN
ERIC K. BUTCHER

Department of Mechanical Engineering
Box 352600
University of Washington
Seattle, Washington 98195-2600

Prepared for:

DOCUMENT CONTROL CENTER

U. S. Department of Energy
Pittsburgh Energy Technology Center
P. O. Box 10940, MS 921-118
Pittsburgh, Pennsylvania 15236-0940

MASTER

Date Submitted: July 19, 1996

~~"U.S./DOE Patent Clearance is not required prior to the publication of this document."~~

HH

DISTRIBUTION OF THIS DOCUMENT IS UNLIMITED

CLEARED BY PATENT COUNSEL

DISCLAIMER

Executive Summary

Coal ash, and particularly fine fly ash, remain one of the principal practical and environmental problems in coal-based power generation. In particular, submicron aerosols are identified with direct inhalation risk.

Submicron ash is thought to arise from mineral vaporization during char combustion, followed by nucleation, condensation and coagulation to yield an aerosol. While aerosols are predominantly made out of volatile alkali minerals, they also can include refractory oxides that are chemically reduced to more volatile forms within the char particle and vaporized. Most of the ash of size greater than 1 μm is generated by agglomeration of mineral as the char particle burns out. These two principal mechanisms are though to account for most of the ash generated in coal combustion.

Previous research has shown that various forms of coal treatment can influence the yields of fine ash from combustion. The research reported here investigates various forms of treatment, including physical coal cleaning, aerodynamic sizing, degree of grinding, and combinations of these on both aerosol yields and on yields of fine residual ash (1-4 μm). The work also includes results from the combustion of artificial chars that include individual mineral elements.

This research shows that these various forms of coal treatment can significantly change ash characteristics. While none of the treatments affected the bulk of the residual ash size distribution significantly, the yield of the ash aerosol mode ($d<0.5$ μm) and fine residual ash mode (1-4 μm) are changed by the treatments. Specific findings include:

- High alkali coals that are either cleaned or sized by aerodynamic classification tend to generate significantly more aerosol upon combustion that the parent coals.

- Aerosol yields from high alkali coals are suppressed when a small amount of excluded mineral matter extracted during cleaning is mechanically mixed into the coal. This suggests that excluded mineral matter will suppress aerosol yields.

- For low-alkali coals, however, the identical coal cleaning process does not change aerosol yields, although it does lead to an increase in the 1-4 μm residual ash mode.

- Particle sizing (specifically the firing of larger-sized particles) leads to an increase in aerosol yields for the low alkali coals. Evidence suggests that the sized fraction requires longer to burn, which yields more time for vaporization of refractory oxides. Note that such a trend may not hold for alkali-rich coals where longer burning times may lead to more alkali capture by aluminosilicates. Again, the refractory oxide vapors do not likely react with aluminosilicates.

- The yield of particles in the 1-4 μm range exceeds that predicted by the breakup model. This mode becomes very significant when the original coal particles have small diameters, and is insignificant for larger-sized coal particles. This suggests that this mode is generated by a process that responds to the specific surface area of the original coal. In one interpretation, these particles result from the release of fine inclusions near the surface of the coal during the initial stages of char combustion. This release occurs only briefly before these particles become absorbed into a surface melt. Thus, one obtains a strong dependance on the initial surface/volume ratio.

- As noted above, cleaning of low-alkali coals leads to an increase in the 1-4 μm mode. Aerosol yields from these coals are dominated by vaporized suboxides and elements derived from refractory oxides. These should not be absorbed by excluded mineral matter since aluminosilicates are unlikely to react with these vapors. Thus, no change in aerosol

yield is expected. However, the cleaning process will strip the surface clean of excluded mineral matter. This may allow small inclusions near the surface to be liberated to a greater degree during the initial stages of burnout than would occur for the straight coal. This would lead to the increased 1-4 μm mode.

- In artificial char experiments, bentonite was demonstrated to be active towards alkali metal capture. Also, pyrite inclusions were observed to fragment during char combustion, but no evidence of the generation of an aerosol was noted.

- Residual ash breakup number is insensitive to temperature or free stream oxygen concentration, but tends to increase for lower-rank fuels (as previously noted in the literature).

A preliminary model of the alkali vaporization/capture process was developed that is based on mass transport control. While this model replicates some of the trends noted in the experiments, it does not yet include finite rate chemistry, which is known to influence some results.

Table of Contents

List of Figures

List of Tables

1.0 Introduction

One of the major obstacles to the economical use of coal is managing the behavior of its mineral matter. Ash size and composition are of critical importance for a variety of reasons. Fly ash size and emissivity affect radiant furnace heat transfer (Gupta, 1983). Heat transfer is also affected by the tendency of ash to adhere to heat transfer surfaces (Walsh *et al.*, 1990), and the properties of these deposits (Field *et al.*, 1967). Removal of ash from flue gas by electrostatic precipitators is influenced by both particle size and particle resistivity (McCain *et al.*, 1975). The efficiency of fabric filter-based cleaning devices is also influenced by ash size (Friedlander, 1977). Both types of devices have reduced collection efficiencies for smaller-sized particles, which corresponds to the size most efficiently retained in the alveolar region of the human lung (Morrow, 1964). This special concern for finer sized particles has led to PM10 and potentially to PM3 regulations.

Laboratory work and studies of full-scale coal-fired boilers have identified two general mechanisms for ash production. The vast majority of the ash is formed from mineral matter that coalesces as the char burns, yielding particles that are normally larger than 0.5 μm. Flagen and Friedlander (1978) proposed a simple model for this residual ash, called the breakup model. In this model, each particle is assumed to yield its mineral matter as a certain specified number of ash particles (usually in the range of 1-5). This latter value is termed the "breakup number." In this way, a known pulverized coal size distribution can be transformed into a projected ash size distribution. The presumed mechanism is that each char particle fragments during combustion, carrying mineral matter with it. The major assumptions used in the model include: (1) all coal particles contain the same percentage of mineral matter, independently of size, (2) all coal particles break into exactly the same number of char particles during combustion, (3) each char particle contains the same amount of mineral matter as the other char particles, and (4) no further fragmentation occurs, which means that each offspring char particle yields its mineral matter as a single ash particle. The breakup number has been identified in more recent work as being influenced by the breakup of the char during burnout, from shedding at the burning char surface (Helble and Sarofim, 1989), and from the fragmentation of discrete included and excluded minerals (Baxter, 1990; Srinivasachar *et al.*, 1990b). Experimental work (Helble and Sarofim, 1989) and elegant site percolation modeling (Kang *et al.*, 1988) indicate that char macroporosity is the single most important factor governing char breakup and residual ash size. Despite the severity of the assumptions, the basic breakup model has proven to be a useful engineering and interpretative tool (Flagen, 1979).

The second major mechanism is the generation of a submicron aerosol through a vaporization / condensation mechanism. When the ash size distribution is plotted in terms of number density, the submicron mode generally peaks at about 0.1 μm. When plotted in terms of mass, this mode is sometimes distinct from the residual ash mode (Flagen, 1979), and sometimes merged into it (Linak and Peterson, 1984). Two sources of mineral aerosols are generally recognized. The predominant mechanism involves the vaporization of volatile alkali minerals, followed by their condensation later in the furnace. In the second mechanism, non-volatile metal oxides are reduced within the char particle to more volatile forms, which reoxidize to aerosols when they are released by the char particle.The features of these two aerosol formation mechanisms are discussed here.

Sodium and potassium are nominally of sufficient volatility to have the potential to fully vaporize during char combustion. Equilibrium considerations suggest that chlorides will be the favored form over the hydroxides (Yuh and Wolf, 1984). In the absence of chlorine, the hydroxides will also vaporize, but at a higher temperature (Srinivasachar *et al.*, 1990a). The presence of aluminosilicates can interfere with alkali release, however. Alkali metals that are originally bound to silicates will not normally vaporize. The capture of alkali vapor by aluminosilicates, both within and outside of the burning char particle, represents an important pathway for alkali metals that competes with aerosol formation.

The mechanism of alkali capture by aluminosilicate is very complex, although the experiments of Gallagher (1992) bring many of the details together. The following represents a summary of Gallagher's findings. The proposed capture mechanism for sodium, released as NaCl(v) is:

$$2NaCl_{(v)} + H_2O_{(v)} = 2NaOH_{(v)} + HCl_{(v)}$$

$$Al_2O_3 \cdot 2SiO_{2(s)} + 2NaOH_{(v)} = Na_2O \cdot Al_2O_3 \cdot 2SiO_{2(s)} + H_2O_{(v)}$$

Thus, the presence of chlorine tends to reduce sodium scavenging by aluminosilicates by driving the first reaction in the reverse direction. If sodium that is initially present as NaCl, features of this mechanism both help and hinder capture by aluminosilicates relative to when it is present as NaOH. First, NaCl must pass through the first reaction to become NaOH, which presents an additional barrier to its eventual adsorption by the aluminosilicate. Second, however, the NaCl will vaporize at a lower temperature than sodium bound to carboxyl groups, which will increase the available time over which it can become complexed.

Modeling suggests that the organically-bound sodium is retained by the organic until the burning char surface reaches the sodium, *i.e.*, the sodium is "burned out" of the char rather than being released within the fuel rich environment in the char matrix. For sodium present as NaCl, the release is faster. For bituminous coals, higher temperatures lead to less sodium retention by the aluminosilicates. This appears to be due to the reduced time available for capture as the combustion temperature is increased. For low-rank coals, the opposite trend is observed. The reasons for this are not as clear. The highly reactive low-rank chars burn in a diffusionally-limited regime, so the characteristic char burning time is only slightly affected by temperature (unlike the bituminous coals). Alternately, the higher temperature appears to directly promote the complexing reaction with the aluminosilicates.

Thus, the implications of the Gallagher work are that alkali vaporization and capture is a complex process involving:

- The original form of the alkali
- The presence of chlorine
- The form of the aluminosilicates
- The char reactivity, insofar as it determines char oxidation time
- The disposition of the aluminosilicates (*i.e.*, between included and extraneous mineral matter)

All of these factors govern the fraction of original alkali minerals that are ultimately released from the char particle, and thus they determine the submicron aerosol yield.

The second aerosol formation mechanism mentioned above is usually a minor contributor except for coals that are unusually alkali-sparse. During diffusion-limited char combustion, the interior of the particle becomes hot and fuel-rich. The non-volatile oxides (*e.g.*, Al_2O_3, SiO_2, MgO, CaO, Fe_2O_3) can be reduced to more volatile suboxides and elements, and partially vaporized (Neville *et al.*, 1981; Senior and Flagen, 1982; Quann and Sarofim, 1982). These reoxidize while passing through the boundary layer surrounding the char particle, thus becoming so highly supersaturated that rapid homogeneous nucleation occurs. This high nuclei concentration in the boundary layer promotes more extensive coagulation than would occur if the nuclei were uniformly distributed across the flow field (Damle *et al.*, 1982). The vaporization can be accelerated by the overshoot of the char temperature beyond the local gas temperature (Quann *et al.*, 1990).

Although these aerosol particles represent a relatively small fraction of the mass, they can present a large fraction of the surface area. Thus, they are a preferred site for the condensation of trace volatile toxic metals later in the furnace. This leads to a layering effect in which the refractory

oxides and/or alkali metals are concentrated at the particle core and the volatile toxic metal oxides reside at the surface (Gladney *et al.*, 1976). This also explains the enrichment of the aerosol by volatile oxides that has been noted in samples from practical furnaces (Linak and Peterson, 1986). These volatile metal oxides include the majority of the toxic metal contaminants, *e.g.*, arsenic, lead and nickel. Risk assessment studies suggest that toxic metal emissions represent a significant portion of the health risk associated with combustion systems (Smith and Goeden, 1990).

Previous work has shown that pulverized bituminous coals that are treated by physical coal cleaning or by aerodynamic size segregation experience a modification in aerosol emissions when burned. Specifically, in some cases the emissions of aerosol for the cleaned and sized coals increased by as much as one order of magnitude. This suggests that aerosol emissions can possibly be manipulated by simple coal treatment, and also that laboratory procedures used to prepare well characterized samples for testing (*e.g.*, sizing) may lead to modifications in ash behavior. The overall goal of this research is to investigate and understand this phenomena, and possibly identify means of exploiting the results to reduce inherent aerosol emissions.

2.0 Objectives

The goals of the work reported here are to:

1. Perform measurements on carefully characterized coals to identify the features of coal treatment which modify aerosol yields.

2. Perform experiments on artificial chars in which the mineral composition and spatial distribution can be varied in order to investigate the mechanism by which treatment influences aerosol yields.

3. Develop a model for use in interpreting the results.

4. Identify whether these mechanisms can be used to reduce aerosol yields from systems burning straight coal.

3.0 Experimental

Initial measurements were obtained in the isothermal flow reactor described in Section 3.1. The bulk of the measurements were performed in the combustion tunnel furnace discussed in Section 3.2. The remainder of this section covers the analytical procedures and the generation of the artificial chars. Fuel properties and preparation are discussed within each of the experimental sections.

3.1 Flow Reactor

The flow reactor consists of a 0.9 m long, 10 cm diameter, alumina tube. The tube is placed in a 3 zone Lindberg electric furnace to provide an isothermal environment. Figure 3-1 shows the furnace, and is divided into two parts, 3-1A and 3-1B. Figure 3-1A shows the upper portion of the furnace where the hot combustion gas is generated in a gas-fired preheater and introduced around a right-angle bend into the furnace through a 2.5 cm venturi. Figure 3-1B shows the lower portion of the furnace where coal is pneumatically injected into the flow at the venturi. The turbulent flow at this point ensures that the coal particles are rapidly dispersed into the furnace gas. As shown on the figure, the combustion temperature, stoichiometry, and gas path length are adjusted to provide the desired O_2 concentration and temperature at the coal injection point. The electrically heated reactor is used to maintain an isothermal temperature for the desired reaction time.

For the present work, the gas flow is generated by a CH_4/air/O_2 flame at a total flow rate of 1.7 gm/s. The stoichiometry is adjusted to provide 10, 20, or 30% O_2 at the coal injection point. The data are collected at two temperatures, 1200°C for the majority of the data and 1350°C for limited tests. This yields mean gas residence times of 1.0 and 0.91 s, respectively. The change in coal residence time due to particle slippage through the gas is estimated to be only about 30 ms. Coal is fed from a screw feeder and is entrained in nitrogen. The coal flow rate is 0.5 g/min, which yields a nominal stoichiometry of 0.07 relative to the free oxygen at the injection point (at 20% O_2). With full dispersion, this yields a coal solids density about 9% of that found in a utility boiler.

3.2 Combustion Tunnel Furnace

3.2.1 Furnace Design

The goal of the combustion tunnel furnace design is to provide a realistic time/temperature history throughout the regions where mineral matter is vaporized and condensed into aerosol. Thus, a non-isothermal design with a longer residence time than is available in the isothermal reactor described in Section 3.1 is needed.

A recasting of the furnace was performed to open the inner passageway to 20.3 cm (8 inches) to provide enough residence time for all of the pulverized coal fractions to be burned. The design is based on a limiting case: to provide complete burnout for the largest coal expected from the aerodynamic sizing process being fired under the lowest planned oxygen concentration. Heat transfer calculations suggest that even with the extensive insulation included in the design, auxiliary heating is needed to maintain the furnace temperature high enough to ensure complete coal burnout, and to provide the desired time/temperature profile. This necessitates the use of two pairs of auxiliary gas-fired burners. These provide a hot gas stream through channels in the refractory that are separated from the main reactor channel. Normally, only one pair of these auxiliary heaters (the upper pair) is needed to maintain a high enough temperature to ensure full coal burnout.

These overall goals were used to develop the following specific furnace design. Based on past experience with similar types of experimental furnaces, a main burner firing rate of 16.1 kW (55,000 Btu/hr) was chosen. Additionally, in order to ensure burnout, the furnace stoichiometry

Figure 3-1A. Reactor Precombustor

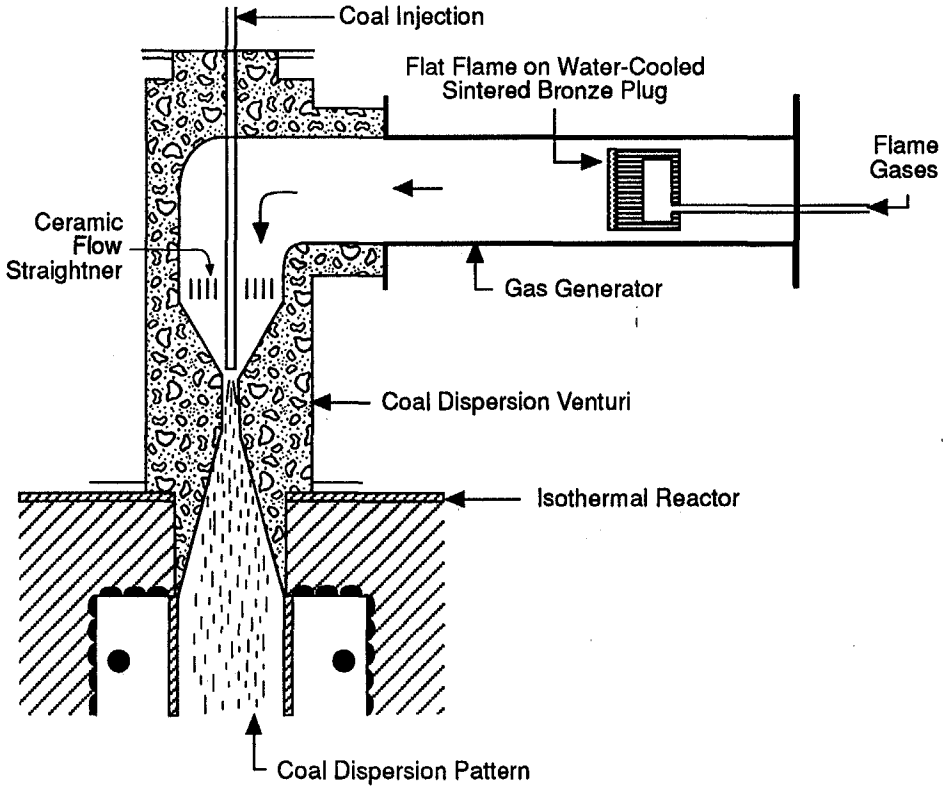

Figure 3-1B. Main Reactor

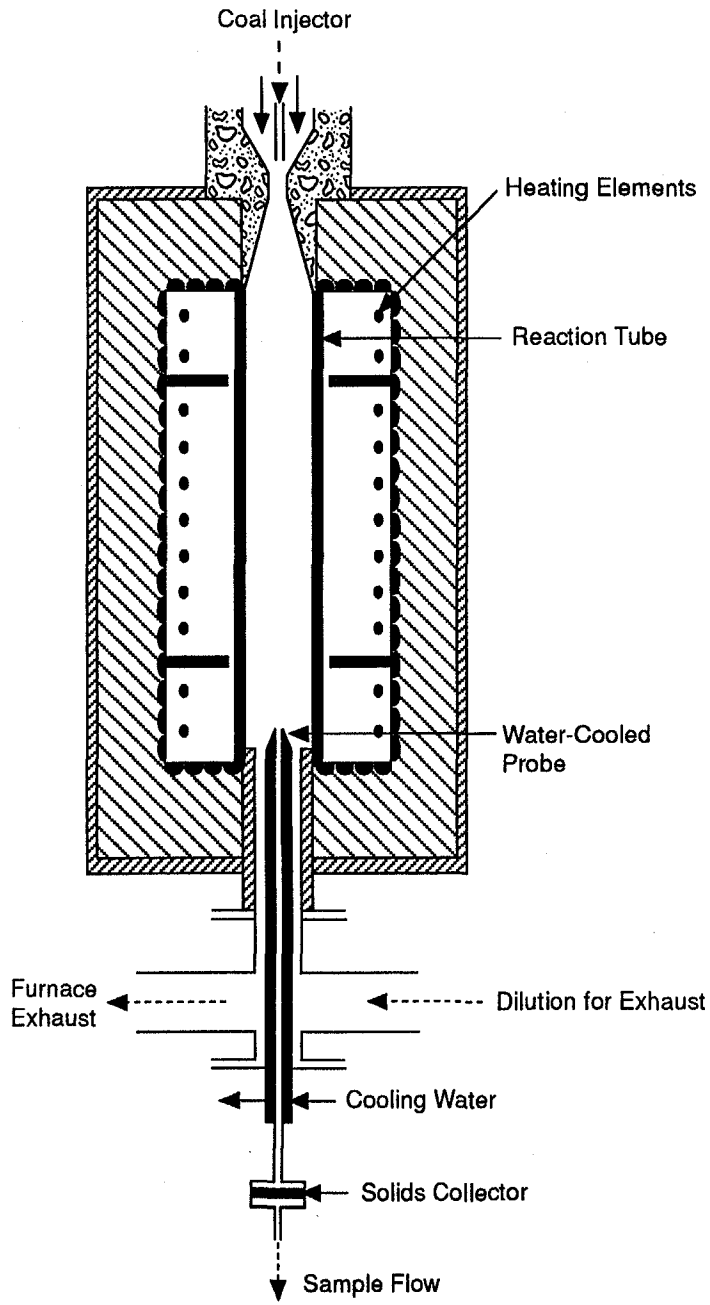

Figure 3-1. Flow reactor system.

was set to provide 7% free oxygen after combustion.

Figure 3-2 shows a sketch of the furnace. The unit has natural gas, air, and cooling water brought into the appropriate accessories. The main burner sits atop the furnace, and the four back-fired burners, forming two pairs of heating channels, can be seen in the middle section of the furnace. Figure 3-3 is a cross-section of the furnace showing the multiple refractory layer design. The inner tunnel diameter is 20.3 cm (8 inches) and the overall outside diameter is 91.5 cm (36 inches). This requires 35.5 cm (14 inches) thickness of insulating material. In spite of this relatively thick layer of insulation, heat transfer calculations show that the combustion gas temperature drops by over 200°C as the gases move down the tunnel and reach the exhaust piping. Thus, the two pairs of backfire burners were included. These are designed to be operated independently to provide whatever inner tunnel temperature profile is desired. Each of the four back-fired burners operates at up to 16.1 kW, but are usually run at lower firing rates. The maximum flame temperature will be 1600°C, and this can be varied by controlling the burner air flow rate.

3.2.2 Auxiliary Systems

In addition to the furnace itself, a number support systems are needed for furnace operation. The following paragraphs give descriptions of these.

Flow System

Furnace operation depends on existing building sources of natural gas and air. The currently available natural gas pressure is about nine inches of H_2O. This low supply pressure restricts the ways in which the natural gas flow is controlled and measured. Specifically, oversized piping, rotameters, and valves are needed to minimize pressure drops. With these precautions, the available natural gas pressure is sufficient to operate burners at necessary levels. The gases are brought to a flow control panel and then routed to the main and backfire burners. Independent control valves allow individual control for each of the five burners at the control panel (shown in Figure 3-4). Rotameters and pressure sensors are placed on line after the control panel to allow accurate monitoring of flow rates and pressures entering the individual burners.

Exhaust System

The flue gas is vented directly into the existing building fume hood. Dilution is used to reduce the temperature in the duct with free flowing air from the laboratory. After passing through mixing baffles, the flow is evacuated through the roof blower. The maximum flue gas temperature - occurring when all four backfire burners and the main burner are fired at their maximum rate - is about 1300°C (2370°F) with a flow rate about 0.032 kg/s (252 lb/hr). At this rate, with the existing fume hood system capable of passing 1.14 kg/s (9052 lb/hr), the flue gas never comprises more than 2.8% of the total flow. Consequently, pure dilution allows a worst-case final exhaust temperature of 60°C (140°F).

During the course of the experiments, the direct spray cooling was eventually used as a way to further reduce the exhaust temperature and decrease the amount of dilution air needed. This is accomplished by adding a twin-fluid atomizer at the point where the furnace flue duct enters the induced-draft fume hood flow. This water spray is directed upstream, and is normally fully evaporated by the flue gas.

Safety System

The large size of the furnace entails a long time constant for responses to changes in temperature. Thus, it requires 24 hour operation during test series. To ensure safety during operation, several precautions are incorporated into the design. The primary safety control system focus on

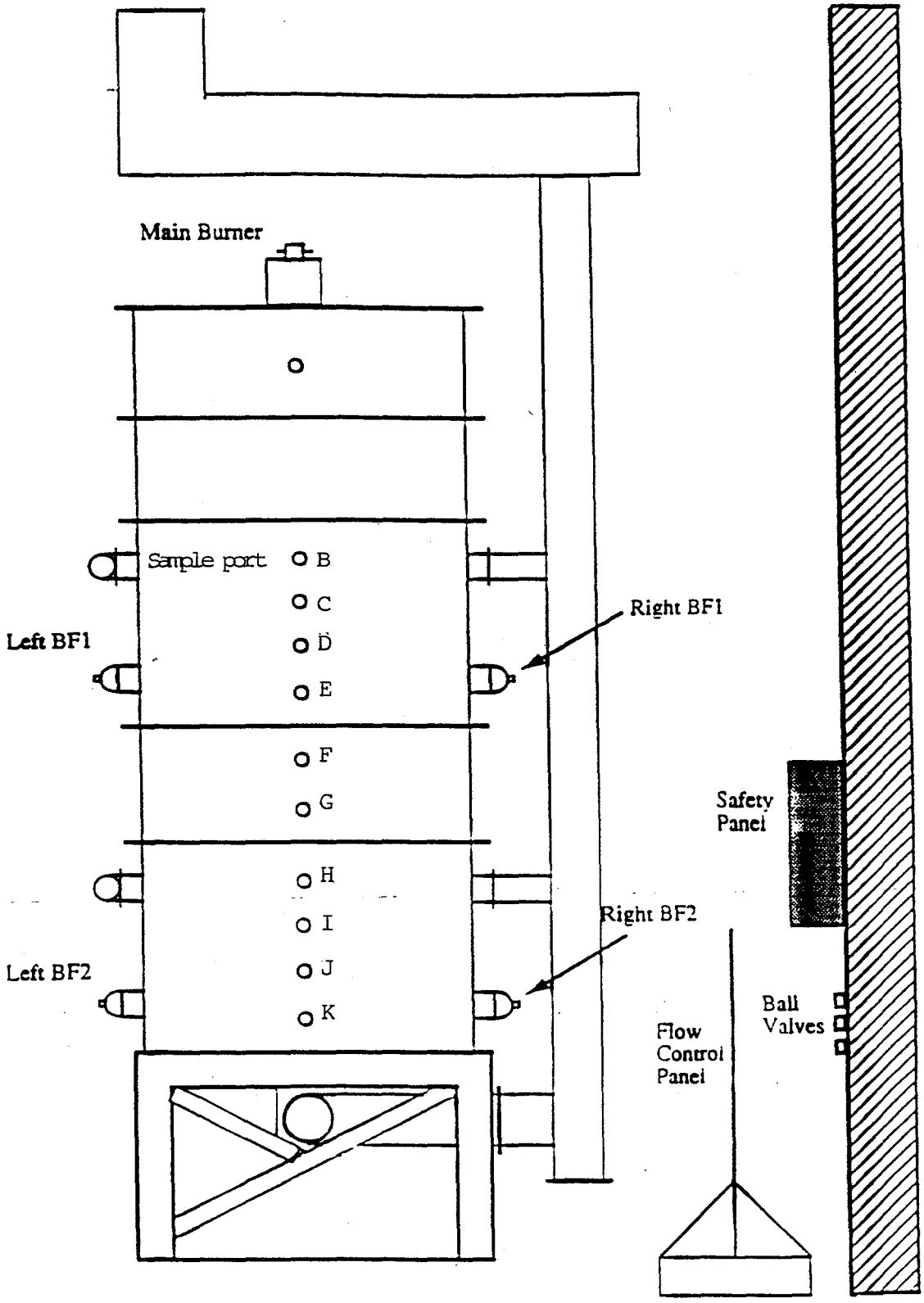

Figure 3-2. Overall reactor schematic.

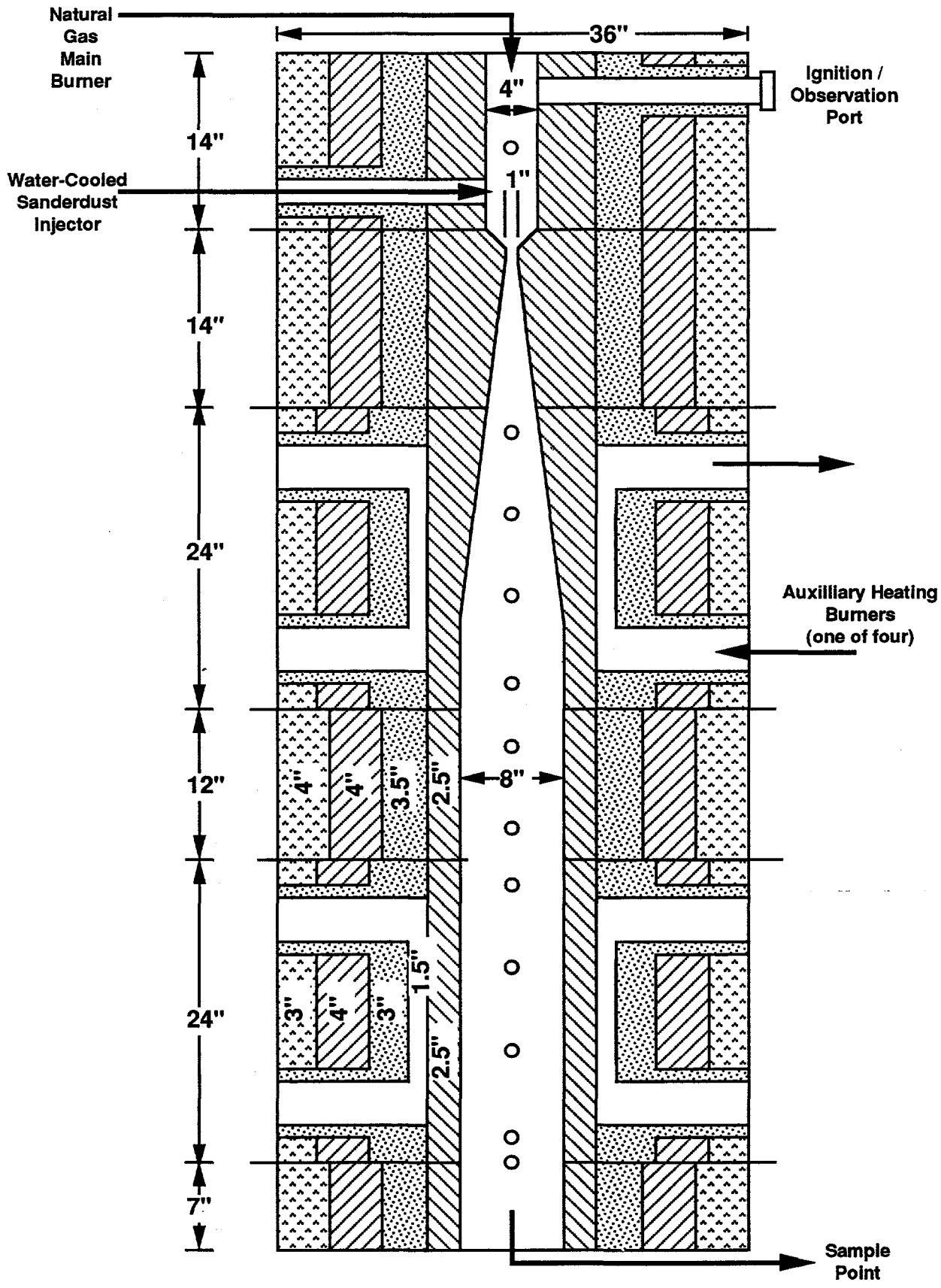

Figure 3-3. Furnace cross-section.

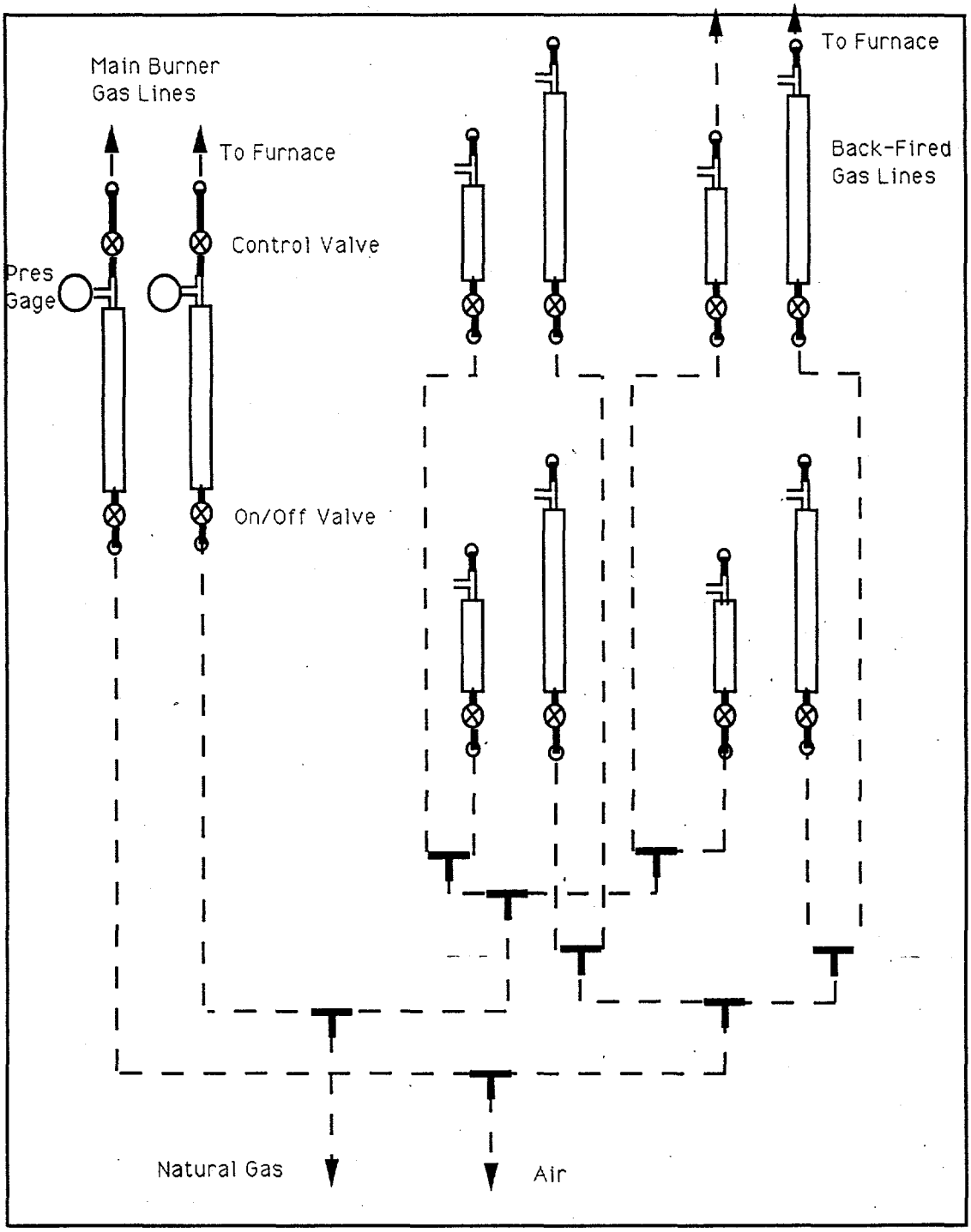

Figure 3-4. Flow panel schematic.

immediate gas shut-off in the event of any abnormal situations. Situations mandating this are:

1. *Loss of flame in any of the five burners* - This is monitored by placing ultraviolet flame detectors near each of the burners.

2. *Loss of either natural gas or air flow* - This is monitored by pressure sensors in the fuel and air lines.

3. *Loss of electrical power* - In the event power is lost in the lab, an electrical trip shuts down the natural gas.

4. *Appearance of combustion products in the laboratory* - A gas sensor in the laboratory capable of detecting methane and carbon dioxide is included to detect natural gas or exhaust products released into the lab.

5. *Loss of building ventilation* - A pressure sensor is placed in the ventilation system to duct draft. The fuel shuts down if ventilation is lost or significantly reduced.

6. *Excessive flue gas temperatures* - Stack temperature will also be monitored with a thermocouple placed in the exhaust duct. A temperature above 130°F in the duct (after the dilution point) shuts the furnace down.

Automatic gas shut-down occurs at a safety valve located on the main gas line into the control panel. This stops the flow to all burners and stabilizes any situation. The air lines and water lines, if burner cooling is required, can be manually shut off without sacrificing safety. A manual bypass of the safety system is provided for start up, enabling a 2 minute window for establishing the flame before the safety systems will execute a shut down.

Since multiple burners are used, it is necessary to provide a system which permits operation with some of the burners off. This requires two elements:

1. A switch on the control panel allows the signal from any of the flame detectors to be disregarded by the control system.

2. If a particular flame detector is disabled, it cannot be possible to send gas to that particular burner without a flame. This necessitates the use of an electronic switch valve on the gas line to that burner. The logic of the system is such that the entire safety system allows operation when a given flame detector is off *only* if the electrical signal from the valve supplying gas to that burner also shows that the gas flow is closed. If that valve is opened, the control system will shut off the gas supply to the entire furnace.

Figure 3-5 shows a basic diagram of the system necessary to satisfy the above conditions. The control panel should centralize all data from the preceding sensors, offering a continual measure for furnace conditions.

3.3 Furnace Characterization

The nominal furnace temperature profile used for the coal experiments is shown in Figure 3-6. This was established by running the main burner at 16.1 kW, the two upper backfires at 16.1 kW each, and leaving the lower backfires off. This measurement is obtained using a high velocity thermocouple (*i.e.*, a suction pyrometer). This suppresses radiant heat exchange with the walls and thus closely approaches the true gas temperature. Coal was not injected during temperature profiling.

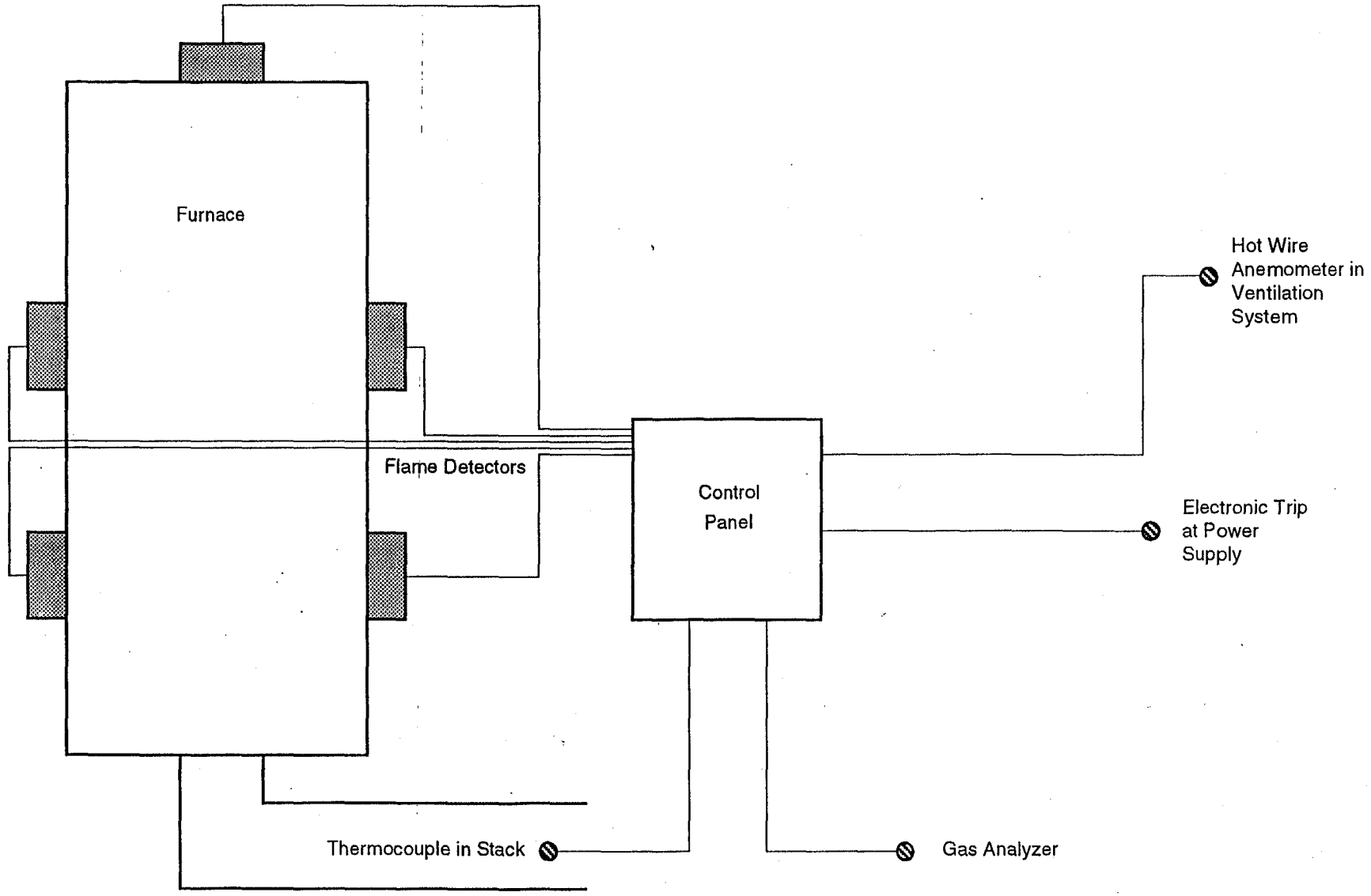

Figure 3-5 General diagram of safety control system.

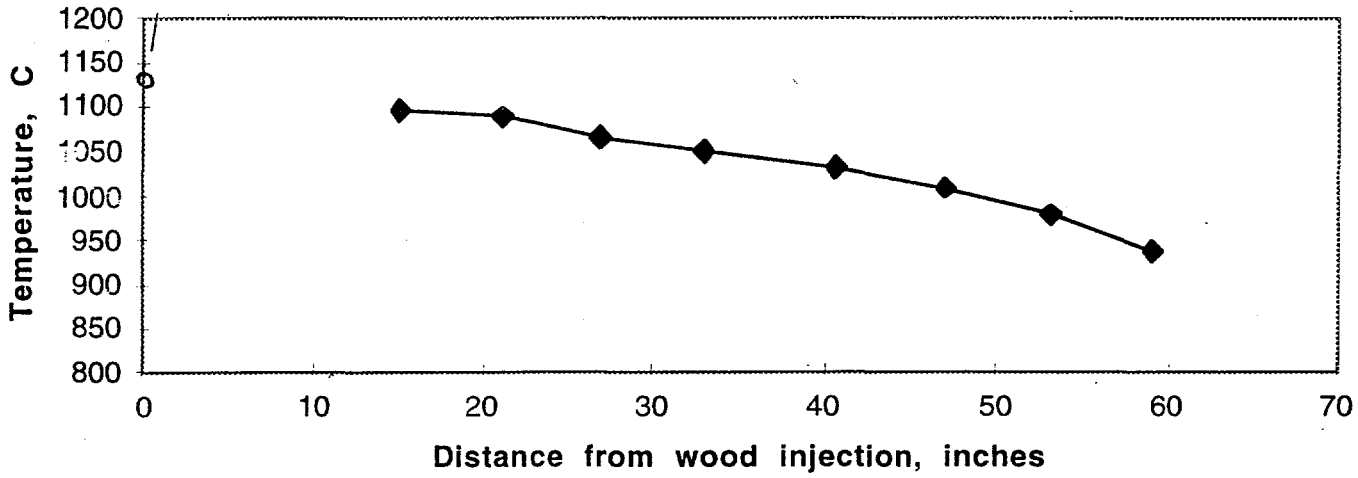

Figure 3-6. Nominal furnace temperature profile (Ports B through I).

Initial tests with the artificial char indicated that higher temperatures were needed to obtain complete burnout. Since the char lacked the macroporosity normally associated with coal, the char did not fragment, and obtaining good burnout became more difficult. To achieve good burnout, the reactor temperature was increased. This is achieved by using all four backfire burner systems, and by increasing the primary furnace firing rate by 32%.

3.4 Coal and Char Injection

The coal samples are metered by an Accurate screw feeder and entrained in air. The particles are injected into the hot furnace gas at a point just ahead of the venturi constriction shown in the Figure 3-3. The constriction is designed to thoroughly mix the coal into the furnace gas. The furnace cross-section then expands to provide the desired residence time, here 1.4 seconds, from the injection port to the sampling port.

The char injector is specially designed and modified due to the small amount of char that is available for each experiment. The screw-drive coal feeder used in previous testing requires 2000 cc or more pulverized coal in order to feed uniformly, so a low volume syringe-drive char injector was designed and constructed as shown in Figure 3-7.

To operate the char injector, pressurized shop air is choked through an orifice to produce a high velocity air jet. Three mechanically driven syringes push the pulverized char perpendicular into the flow stream, where the char is entrained and fed into the water-cooled injector port. Three 10 cc ports were chosen over a single 30 cc port, in order to limit the cavity formation in the char remaining in the syringe. For each experiment, only 6 cc of char is loaded in each syringe to avoid any measurement error.

3.5 Sampling and Analysis

Coal samples are collected by a hot water-cooled probe located at the reactor exit. A heated glass fiber filter is used when collection of the entire coal sample is desired. Alternatively, an 8-stage Anderson viable cascade impactor is used at the probe exit when detailed size analysis of particles below 8 μm is needed.

The Andersen Mark II Cascade Impactor sorts the particles into eight size classes using inertial impaction. The nominal size of a stage is defined as the diameter of a particle having a 50% probability of capture on that stage. Aerosol, which is typically particulate matter on the order of 0.1 μm diameter, is collected on a borosilicate microfiber filter downstream of the final impaction stage. The impactor is fitted with a preseparator, which is designed to prevent large particulate matter (greater than 10 μm in diameter) from entering the size segregating area of the impactor. Without preseparating, oversized particles can bounce through to smaller size cut stages. During testing, 3.5% of the effluent gas and associated particulate matter is pulled through the impactor.

The upper size limit of the impactor is about 8 μm, so an alternative is needed to characterize the size of larger residual ash particles. To do this, the total ash sample is collected on the glass fiber filter and resuspended in a surfactant solution in a sample cell. The size distribution is then measured by laser diffraction using a Malvern 2600 HSD size analyzer. Details of the analysis procedure are available elsewhere (Kramlich and Newton, 1994). It is recognized that particles under 1-2 μm are difficult to resuspend in the liquid, so data reported for the ash below 2 μm cannot be regarded as reliable. This size range is covered by the impactor data.

The procedure for using the cascade impactor is as follows. Each stage of the impactor trays are cleaned thoroughly using acetone, dried in the oven at 110°C for twenty minutes to remove moisture, cooled to room temperature in a desiccator, weighed carefully using a high precision electronic scale, and reloaded into the impactor. Finally, the entire impactor is preheated to 110°C

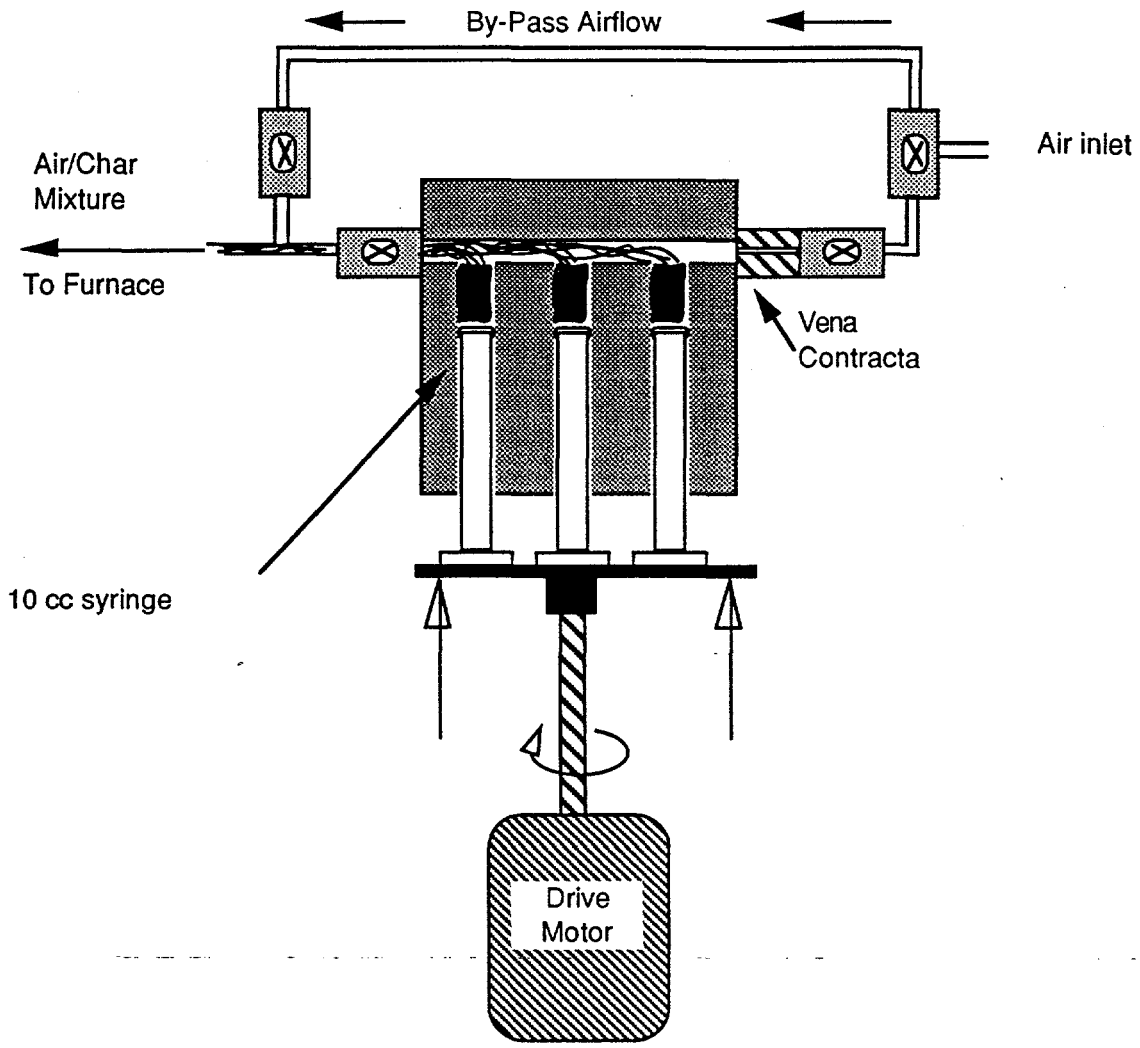

Figure 3-7. Syringe drive char injector system.

for twenty minutes. Throughout the impactor preparation, the trays should be stored in the desiccator unless they are in the oven to remove moisture and contamination. Since the weight of aerosol fraction is in the range of 0.00001 gram, it is critical to avoid contamination from the dirt, moisture, and any stray particles from atmosphere.

The sampling time takes usually about thirteen to fifteen minutes. At this point, the suction pump and the injector are turned off. After carefully removing the impactor from the experiment, each tray is dried again in the oven at 110°C for twenty minutes, and then is placed in the desiccator to cool to room temperature. The weight of ash is measured with the tray to avoid any spill and contamination, then the weight of tray is subtracted from the total weight to obtain the ash weight.

3.6 Artificial Char Procedures

The artificial char is manufactured using the sucrose pyrolysis technique (Neville *et al.,* 1981). This is relatively easy to perform, but still yields a char whose structure resembles natural coal char. Ingredients included in the artificial char are a high purity sucrose, carbon black, and both volatile alkali metals and discrete mineral inclusions. In this experiment, sodium oxalate is used as a source of alkali metal, and iron pyrite, bentonite, calcite are used as mineral inclusions. Sodium oxalate is chosen as a sodium source because of its solubility in sucrose solutions, and its low decomposition temperature (250 - 270°C).

Carbon black is used to provide the microporosity that is present in natural chars. Macroporosity is often generated and controlled by the use of lycopodium spores. This allows one to control char particle breakup during combustion. None were, however, used in the current work. The three minerals used in manufacturing the artificial char are ground to the desired size using a ball mill before being added to the char mixture. The final size after grinding, as well as physical and chemical information on the additives, are shown in Table 3-1.

The size of the mineral inclusions is checked using a sedigraph. The sedigraph records the size of fine insoluble particles by using a measurement of X-ray extinction to monitor the settling time in the known sedisperse liquid. In order to use the sedigraph, the settling rate must be calculated using the information on the solid material and the sedisperse liquid. Information required includes; the density of the material and the sedisperse liquid, approximate starting diameter of the material, and the viscosity of the sedisperse liquid at a known temperature. The rate is calculated from the following equation:

$$\text{Rate} = \frac{211.8(\rho - \rho_o)}{\eta\left[\frac{50}{D_s}\right]^2}$$

where: ρ = density of material in g/cc
ρ_o = density of sedisperse liquid in g/cc
η = viscosity of sedisperse liquid in centipoise
D_s = starting diameter in μm

Rate calculations for the various minerals, other useful information on the sedigraph operation, and the sedigraph datasheets are available (Park, 1995)

The equipment used in manufacturing the artificial char includes a crucible, ultra high purity nitrogen, and an oven which can heat the mixture up to 600°C. The oven is closed to the environment and purged by the high purity nitrogen whose flow is controlled by a rotameter. The artificial char mixture is heated to 600°C under the nitrogen blanket to avoid char oxidation. A

Table 3-1
Summary of Materials used in Artificial Char Preparation

	Chemical Formula	Purity (%)	Size before the ball mill	Size after the ball mill	Time in the ball mill
Sucrose	$C_{12}H_{22}O_{11}$	100.0	N/A	N/A	0
Carbon Black	C	100.0	40 - 60 nm	40 - 60 nm	0
Sodium Oxalate	NaO_2CCO_2Na	99+	N/A	N/A	0
Pyrites	FeS_2	94.5	18 μm	9 - 10 μm	5 Hrs.
Bentonite	(Na, Ca) Montmorillonite*	90+	0.9 - 1 μm	0.9 - 1 μm	0
Calcite	$CaCO_3$	100.0	15 - 17 μm	15 - 17 μm	4 Hrs.

temperature controller, operating off of a thermocouple, is used to control the power to the oven. The entire setup to prepare the artificial char mixture is depicted in Figure 3-8.

The artificial char is prepared from the mixtures of high purity sucrose, carbon black, distilled water, sodium oxalate, pyrite, bentonite, and calcite. Mineral inclusion type, size, and number density can be chosen arbitrarily. Because this research concentrates on how the different amounts and kinds of mineral matter affect the release versus capture of sodium during the char combustion, fourteen different kinds of artificial chars are prepared using different mineral matter compositions. The properties of these chars are summarized in Table 3-2.

The amount of mineral doped into the artificial char was based on the weight ratio that is normally present in raw coal. The sodium loading was selected to be representative of western low-rank coals, which are normally high in sodium. Since about half the coal weight is lost during devolatilization in normal coal combustion, the mineral loadings in the artificial char are designed to be about twice the values expected in the raw coals. The sodium weight percentage in the char is approximately 1% with an assumption that none of sodium and other mineral matter are vaporized during the heating and charring process. For this experiment, the weight ratio of mineral matter to char is chosen at 3.7%, 2.5%, and 1% for pyrite, bentonite, and calcite respectively. The chars containing the exact ratio of mineral matter mentioned above are char #5 for pyrite, #10 for bentonite, and #15 for calcite.

The weight ratio of sodium to mineral matter is determined based on the information in the PSI reports (Boni *et al.*, 1992). The chars that have other composition ratios are prepared to investigate the effect of mineral matter concentration on sodium release versus capture. Three additional chars were prepared for each type of mineral matter. These contain 50%, 150%, and 200% of the baseline mineral concentration.

The procedure for preparing the artificial char is as follows: (1) reagent grade sucrose and sodium oxalate are dissolved in distilled water. (2) Mineral matter is then added to the solution. (3) Carbon black is added to the mixture, with the mass of added carbon black equal to the dry mass of sucrose (except for char #2). The mixture is stirred well throughout the mixing process to prevent settling. Char #2 has a different sucrose/carbon composition ratio to examine how the porosity of the char influences the sodium release. Since char #2 has less carbon black, it is believed to be less porous. (4) The mixture is heated at 40-50°C in a beaker until it achieves a pasty consistency. (5) The mixture is then placed in two crucibles. (6) The mixture is heated in the oven to 600°C at the rate of 15°C/min. under a slight positive pressure (4 psig) in 400 - 500 standard cc/min. ultra high purity nitrogen (certified at 99.9% nitrogen). (7) After charring at 600°C for one hour, the sample is cooled to room temperature under a nitrogen environment. During the charring process, about 50% of the original sucrose/carbon black dry weight is lost. The maximum pyrolysis temperature is chosen to be 600°C to prevent the loss of sodium, which should be completely vaporized by 880°C.

The sample is then crushed down to approximately 50 - 70 μm in the ball mill. Since the char contains mainly carbon, the size cannot be measured by the sedigraph due to the poor absorption of X-rays by carbon. The size is approximately measured by optical sizing. The time required to reach the 50 - 70 μm size range in the ball mill is one hour and fifteen minutes for all the chars except char #2, which requires two hours due to its reduced porosity. Figure 3-9 summarizes the artificial char manufacturing process.

The structure of artificial char prepared using the above process is comprised of carbon black spheres, held together by pyrolyzed sucrose as a binder. Although nitrogen is used to remove the oxygen while charring in the oven, the final product contains no detectable nitrogen, only 0.5 - 1.0% hydrogen, and 0.5% moisture content (Flagan, 1978).

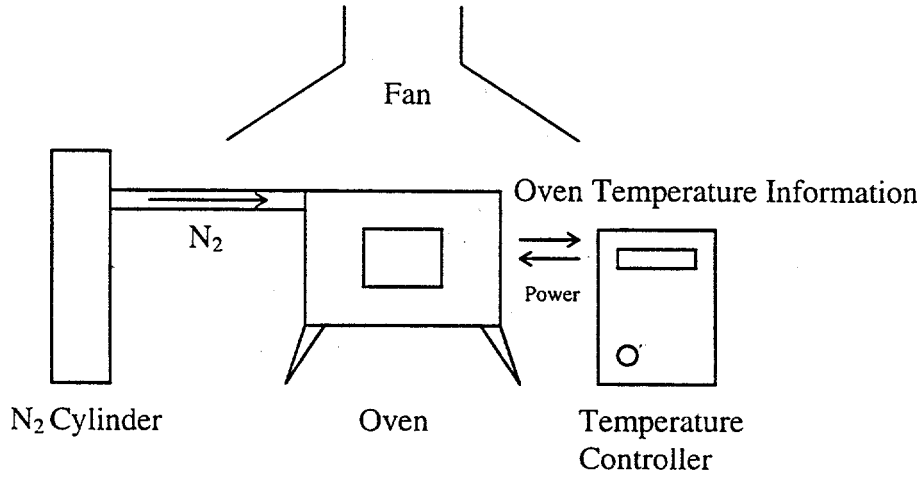

Figure 3-8. Experimental layout for artificial char preparation.

Table 3-2
Artificial Char Composition Matrix

	Sucrose	Carbon Black	Sodium	Pyrite	Bentonite	Calcite
Char #1	50	50	0.5	0	0	0
Char #2	70	25	0.5	0	0	0
Char #3	50	50	0.5	**0**	0	0
Char #4	50	50	0.5	**0.925**	0	0
Char #5	50	50	0.5	**1.850**	0	0
Char #6	50	50	0.5	**2.775**	0	0
Char #7	50	50	0.5	**3.700**	0	0
Char #8	50	50	0.5	0	**0**	0
Char #9	50	50	0.5	0	**1.25**	0
Char #10	50	50	0.5	0	**2.50**	0
Char #11	50	50	0.5	0	**3.75**	0
Char #12	50	50	0.5	0	**5.00**	0
Char #13	50	50	0.5	0	0	**0**
Char #14	50	50	0.5	0	0	**0.25**
Char #15	50	50	0.5	0	0	**0.50**
Char #16	50	50	0.5	0	0	**0.75**
Char #17	50	50	0.5	0	0	**1. 00**

Note 1: Values are in gram
Note 2: Char #1 = Char #3 = Char #8 = Char #13

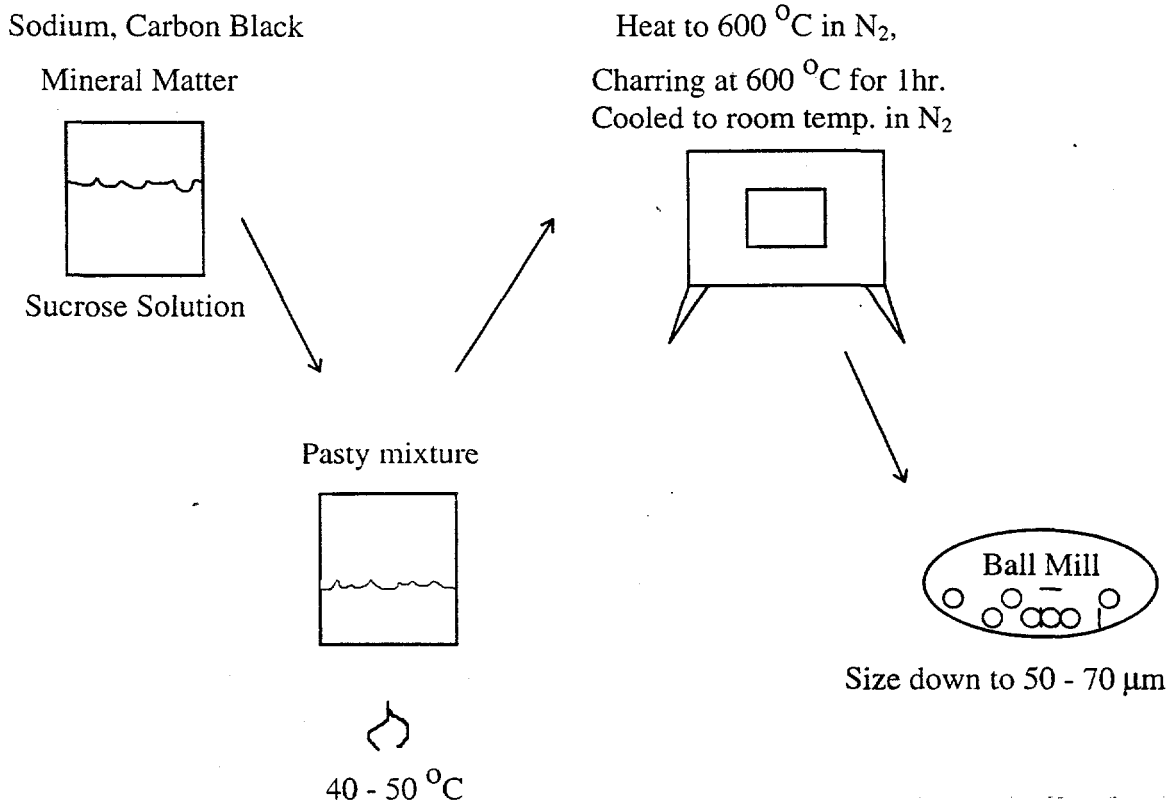

Figure 3-9. Artificial char preparation process.

4.0 Isothermal Results

The results presented in this section are for the *isothermal* experiments involving the raw, sized, and physically cleaned coals.

4.1 Coal Preparation and Properties

Proximate analyses for the coals tested are listed in Table 4-1, along with their nominal ranks. The coals were ground in an industrial-scale recycle Raymond bowl mill to a broad size distribution with a mass median diameter of 30-50 μm. This was designed to be representative of utility boiler practice (70-80% -200 mesh). The size distributions of the coals were obtained using the laser diffraction procedure discussed in the previous section. The procedures for the partitioned coals (cleaning and aerodynamic sizing) are discussed later.

4.2 Residual Ash Size Distributions

4.2.1 Initial Experimental Studies

Figure 4-1 is an example of how the raw data are presented by the laser diffraction system. In this case the plots show cumulative size distributions for ash from the Utah bituminous coal. The cumulative size distribution for the parent coal is also shown in Figure 4-1. For purposes of interpretation, we present the data in terms of the breakup number. Although the model has limitations, it provides a convenient approach for correlating behavior. In the calculations, the assumed densities for the coal organic matter, coal mineral matter and burned ash are 1.3, 2.7, and 2.2 gm/cm^3, respectively.

Figure 4-1 shows two model lines. The first corresponds to a breakup number of 1.0. The second line represents model predictions where the breakup number is adjusted such that the mass median diameter provided by the model matches that of the data; in this case 4.6 is the optimum number. Table 4-2 shows the optimum breakup number developed for each coal, while Figure 4-2 summarizes the correlation between nominal coal rank and the breakup number. The lower rank coals generally show higher breakup numbers, while the high rank coals show numbers much closer to unity. (Note that for the high rank coals, several data points rest at unity, and thus overlie each other. The curve in Figure 4-2 gives an approximate mean of all of the points.) Figure 4-2 also shows the influence of reactor oxygen concentration, which had little consistent effect on the results. Reactor temperature was likewise varied for a limited number of cases (from 1200 to 1350°C), but this yielded no consistent change in behavior. This agrees with literature trends in which the residual ash size distribution was relatively invariant with combustion conditions (Helble and Sarofim, 1989).

After the breakup number is optimized, it is possible to judge the goodness of the fit over the entire size range, *i.e.*, did the shape of the size distribution curve match the shape predicted from the breakup model. In general, the quality of fit was quite good. One deviation was associated with the Australian bituminous No. 2 coal, which yielded a less reactive char that did not fully burn out within the reactor. This was characterized by an overabundance of large particles within the size distribution. In a second deviation, the cleaned Canadian coal appeared to feed as agglomerates due to sticking, which was manifested in calculated breakup numbers of less than 1.0 due to large ash particles and incompletely burned char.

The third deviation appeared in most of the coals. It consisted of an overprediction of the finest ash size, less than 2 μm, and it is shown to a limited extent in Figure 4-1. Examination of this deviation showed it to be due to an inability to disperse ash particles under 2 μm in the surfactant solution when preparing the ash for optical sizing. Since the size range of most interest was that in the lower half of the size distribution, further experiments used the cascade impactor to avoid

Table 4-1

Coal Rank and Proximate Analysis

Coal	Rank	Ash[1] (%)	H_2O[1] (%)	VM[1] (%)	MJ/Kg (dry, ash free)
Utah	HVB	6.3	4.0	40.1	30.7
Illinois No. 6	HVC	8.7	12.0	33.5	28.6
Illinois	HVB	11.8	4.1	34.4	28.4
Aust. No. 1	HVA	16.3	1.4	31.4	29.2
Aust. No. 2	HVA	16.7	1.7	26.8	29.1
Aust. No. 3	Med. Vol. Bit.	12.0	2.7	22.0	30.3
Aust. No. 4	Med. Vol. Bit.	13.5	3.6	25.7	28.9
Canadian[2]	Anthracite	6.9	0.7	16.8	32.1
U.S. -Low S	HVC	12.6	8.1	36.8	28.7
Indonesian	HVC	1.6	3.5	40.0	28.8
62% Ill/38% Ky	HVC	8.7	9.3	35.2	27.3
Eagle Butte	SubC	5.0	24.1	32.9	27.3
Big Brown	SubA	14.5	10.4	39.6	25.0
Beulah	Lignite A	10.5	28.3	29.5	23.7

[1]As received; ranks based on this analysis.
[2]Cleaned coal. Rank reported based on ASTM classification for this analysis.

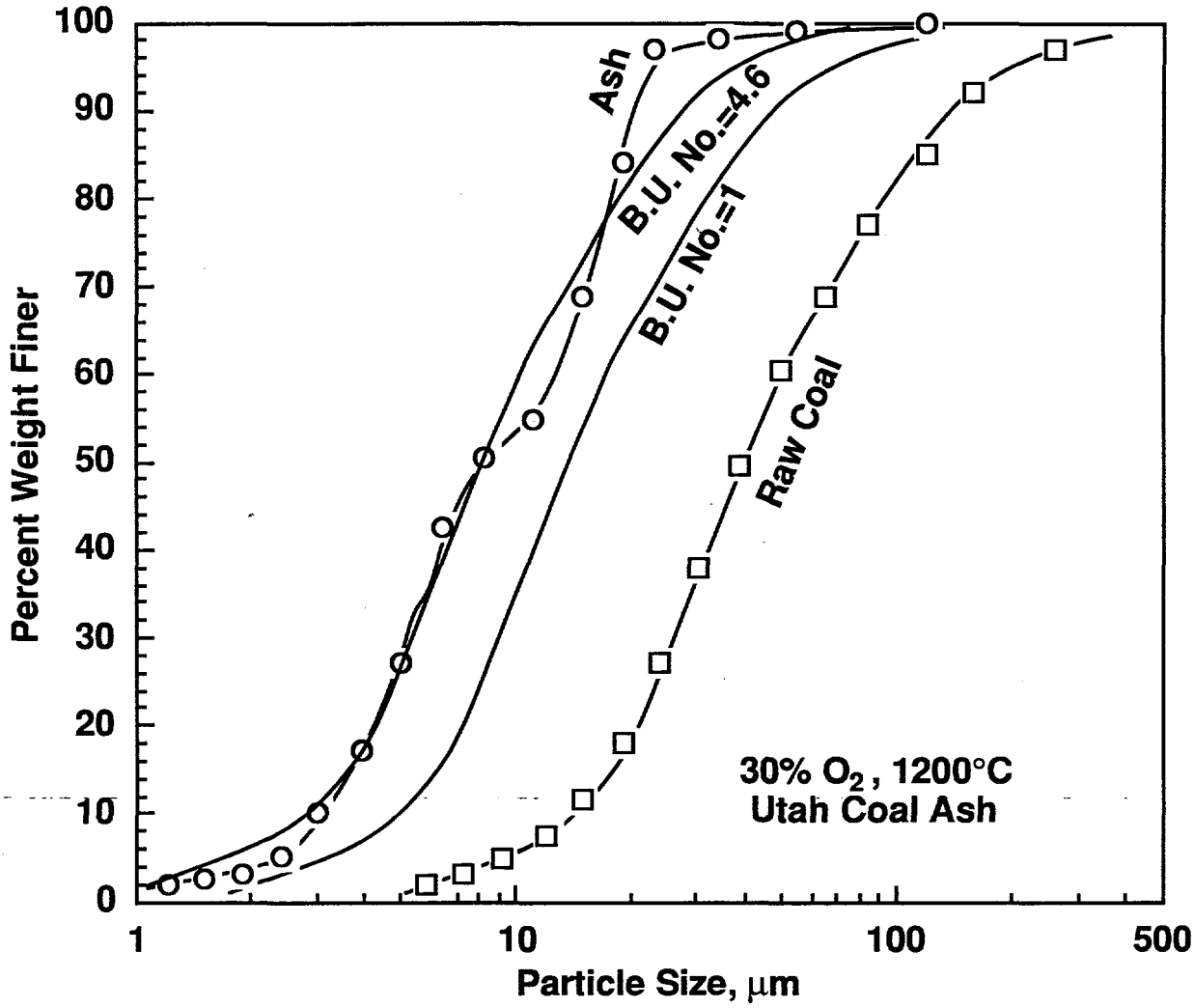

Figure 4-1. Laser diffraction size measurements for Utah coal ash and the parent coal. Also shown are breakup model predictions for breakup numbers of 1 and 4.6.

Table 4-2
Optimum Breakup Numbers at 1200°C

Coal	Oxygen Concentration		
	10 %	20%	30%
Utah	3.1	1.8	4.6
Utah (1350°C)		1.0	2.1
Illinois No. 6		1.0	1.0
Illinois	2.7	3.5	2.2
Aust. Bit. No. 1		2.9	5.0
Aust. Bit. No. 2		1.0	1.0
Aust. Bit. No. 3		1.0	1.0
Aust. Bit. No. 4		5.0	5.0
Cleaned Canadian		0.015	0.125
Illinois/Kentucky Blend	1.0	6.0	6.0
Eagle Butte		5.0	6.0
Big Brown		7.0	8.0
Beulah		11.0	16.0

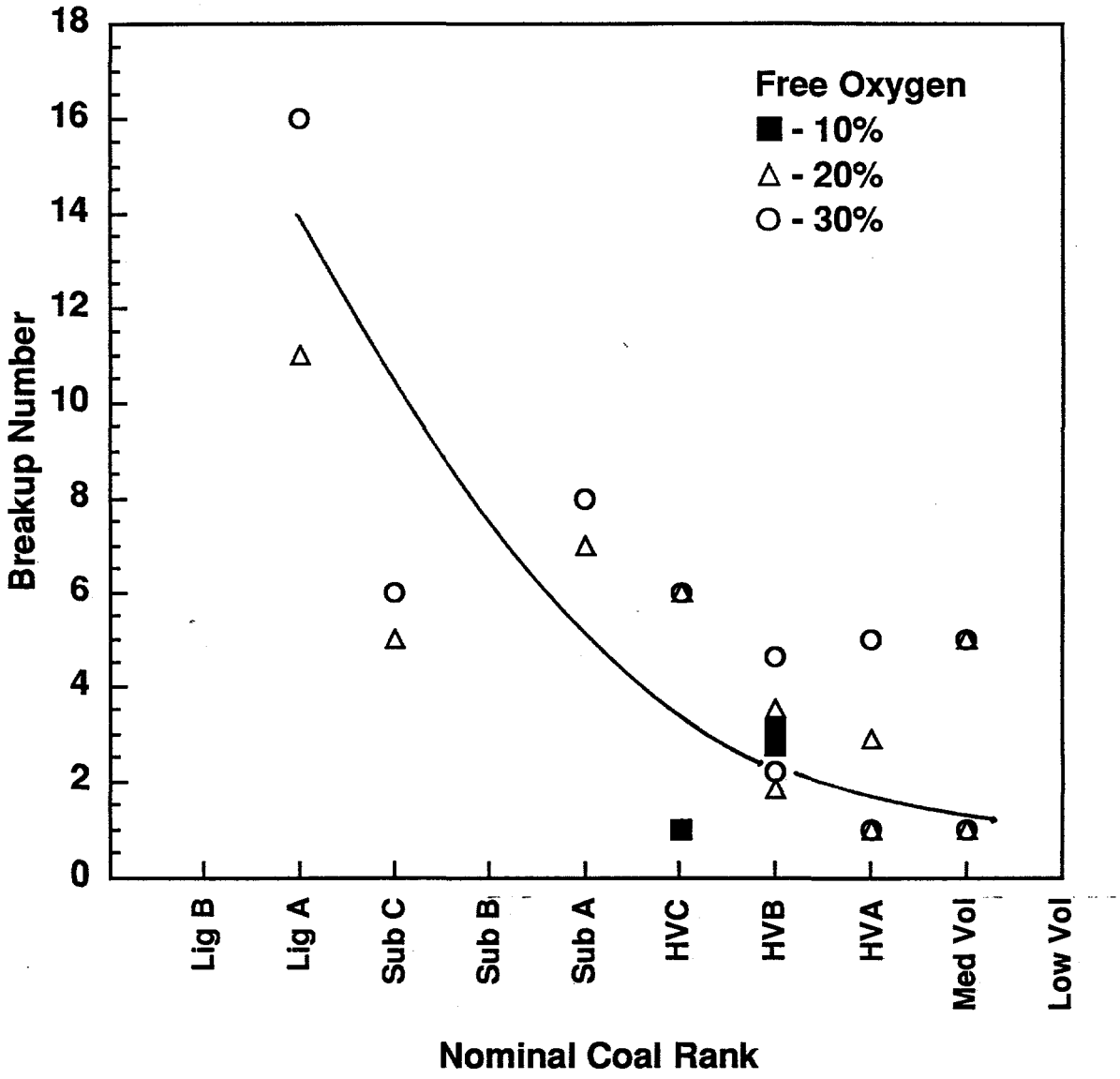

Figure 4-2. Laser diffraction measurements of the dependence of breakup number on coal rank.

biased measurements.

4.2.2 Modified Breakup Modeling

In the original breakup model, (1) all coal particles are assumed to contain the same amount of mineral matter, and (2) each coal particle is assumed to give up its mineral matter as a specified number of equally sized ash particles. Application of the original breakup model to the cascade impactor data for the ash from the raw Utah bituminous coal is shown in Figure 4-3. Here, the breakup number was optimized to match the mass median diameter based on the laser diffraction data. Note that the amount of fine particulate matter considerably exceeds that predicted by the model.

A modified breakup model was developed in which coals of identical size were assumed to produce a distribution of ash particle sizes. This is illustrated in Figure 4-4. This ash distribution resulting from each coal size class is integrated over the entire coal size distribution to complete the transformation of the coal size distribution into a predicted ash size distribution. Note that the Gaussian distribution is truncated such that no ash particle diameter can exceed the diameter of the original coal particle (this presumes that the largest ash particle corresponds to that produced by a coal particle that contains only mineral matter). The distribution is also truncated at D=0, although this has little practical consequence since the size distribution has essentially vanished by this point. The breakup number is set to the value shown in Table 4-2, while the Gaussian standard deviation is adjusted to minimize the error between the predicted and actual distribution (minimizing the sum of the squares).

Although application of the modification improved the fit, significant deviations still exist. To account for these, two additional model modifications were made. First, the tendency of the cumulative size distribution to "level off" between 0.2 and 0.5 μm is due to the bimodal size distribution discussed earlier, with the mode at D≤0.2 μm being aerosol from the vaporization / condensation mechanism. Since this mode is not specifically accounted for in the breakup model, it was assumed that all ash less than 0.3 μm is from the aerosol mechanism, and the measured aerosol yield is used to modify the predicted ash cumulative size distribution. Application of the Gaussian breakup model and the inclusion of the empirical aerosol correction is shown in Figure 4-3.

The second modification involves the tendency of the data to "level off" between 2.5 and 4 μm. A differential plot of measured ash size distributions provides information on which ash particle sizes are most predominate. The data in Figure 4-3 are plotted in Figure 4-5 as differential ash size distributions, along with similar data from other coals. (These curves were generated by differentiating a spline fit to the cumulative impactor data.) All four coals exhibit a peak at approximately 1-2 μm. This is similar to the mass median diameter reported for discrete coal inclusions (Sarofim *et al.*, 1977). This mode has been variously attributed to inclusions released during grinding, and to shedding of discrete inclusion during the initial stages of char burnout. Helble and Sarofim (1989) present visual evidence that this mode could arise due to micro-fragmentation at the perimeter of the burning char particle.

The fate of these inclusions has generated considerable recent interest. Baxter (1990) notes that pyrite inclusions fragment to about half their original diameter during combustion, although such a change could not be easily resolved under the present measurement approach. In the current model, we have accounted for this mode by assuming that all inclusions within a specified distance of the initial char surface are released through shedding without agglomeration. These inclusions are assumed to be released as 2 μm particles, and the depth over which free release occurs is adjusted to fit the data. Figure 4-3 also includes this final model modification in which all inclusions with centers within 1 μm of the original char surface are released.

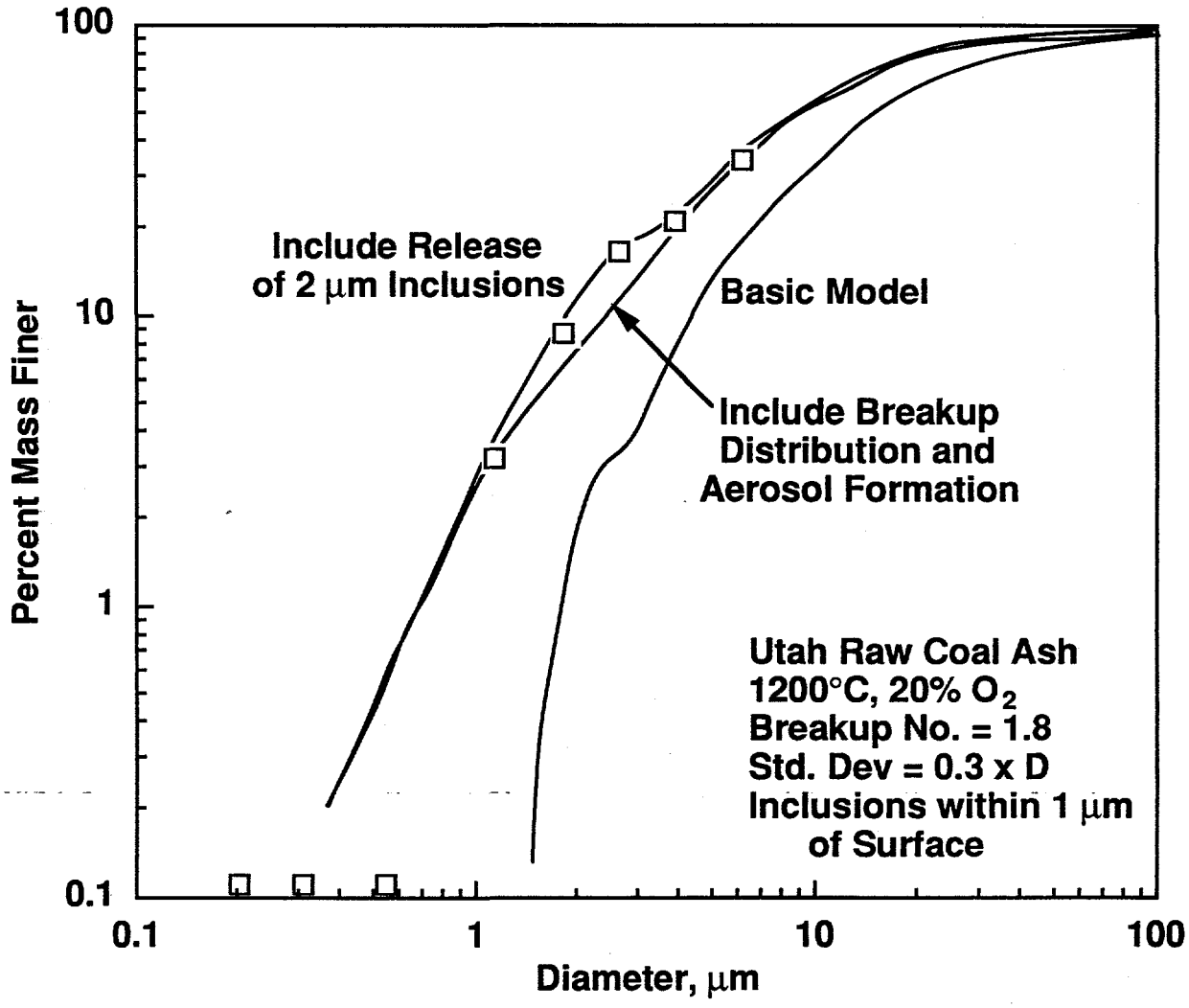

Figure 4-3. Comparison of cascade impactor data with the basic and modified breakup model. The first modification includes aerosol formation and a distribution of particles, and the second modification adds the release of 2 μm inclusions within 1 μm of the surface.

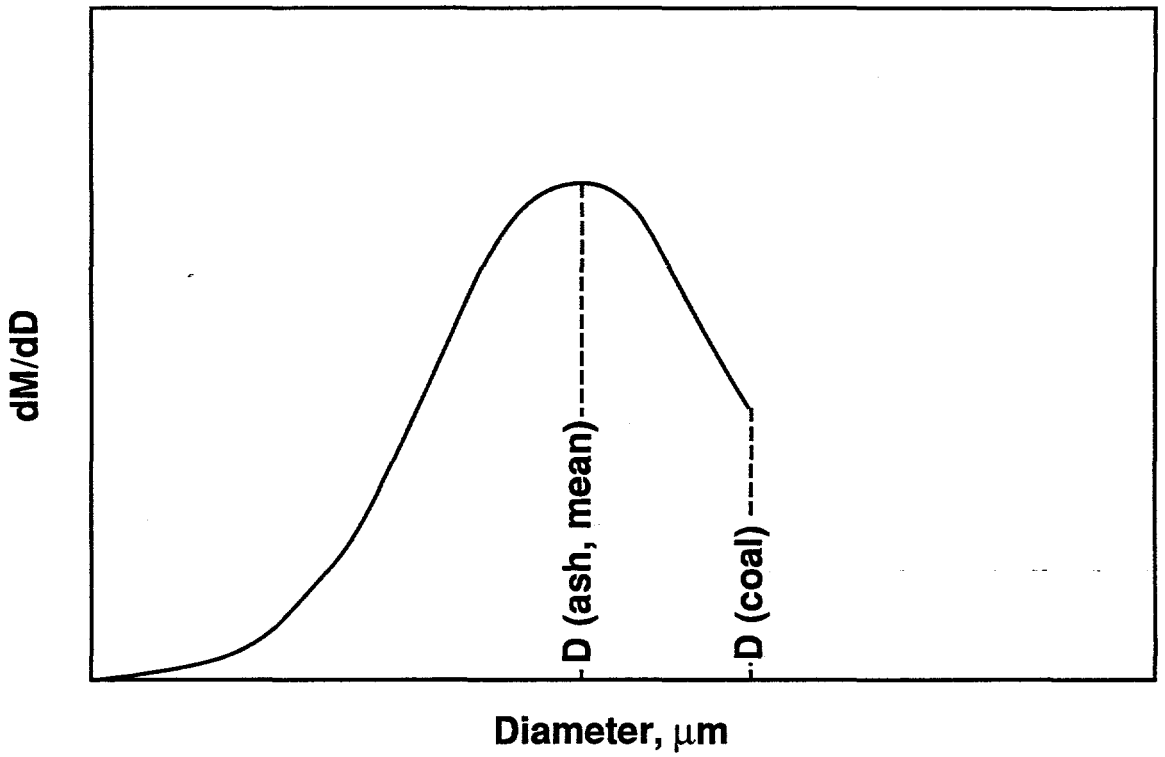

Figure 4-4. Gaussian distribution used in modified breakup model.

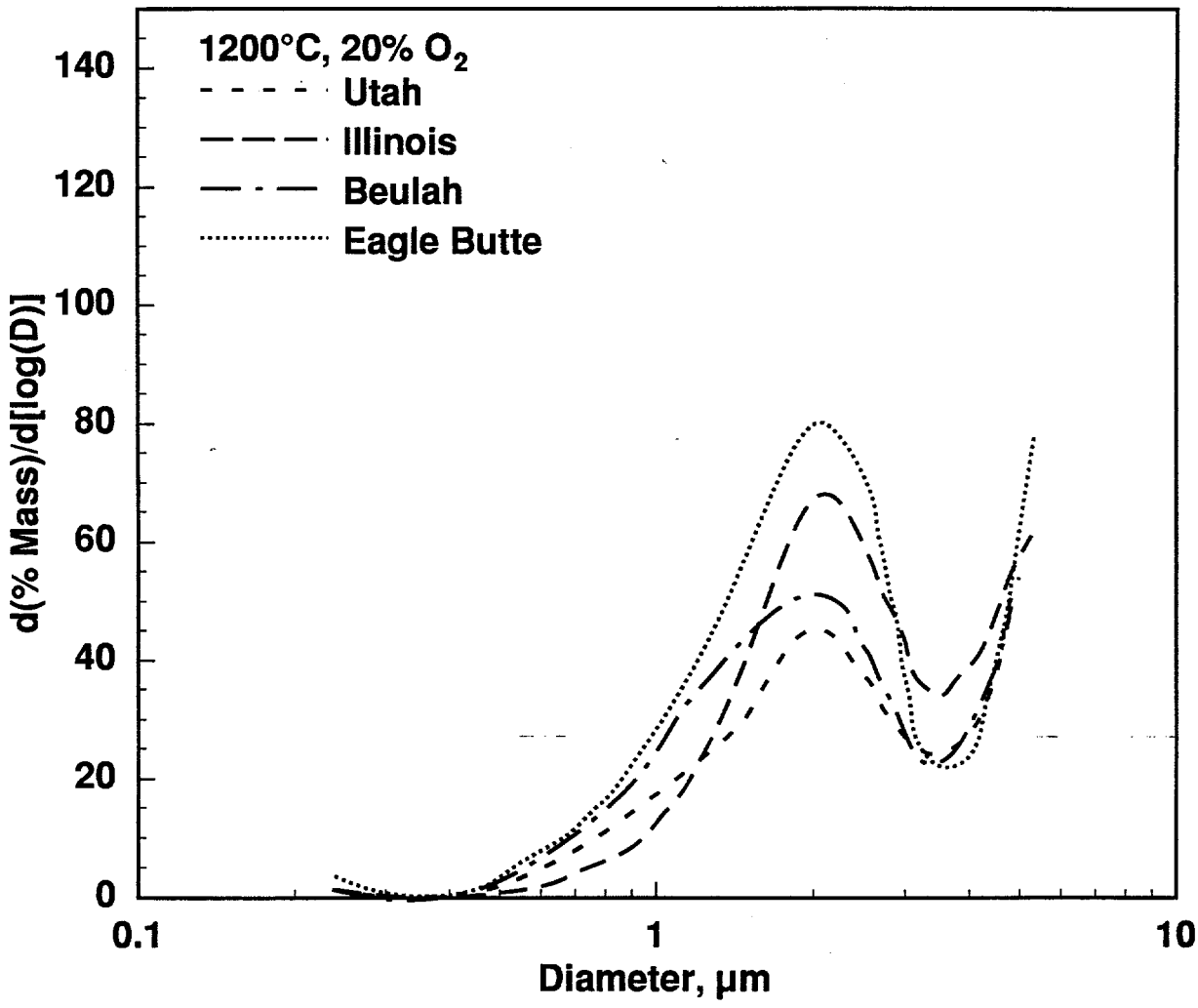

Figure 4-5. Differential size distributions of four raw coals.

In summary, the model includes four empirically determined parameters. These are (1) the diameter at which the mass median diameter from the unmodified breakup model matches the data, (2) the experimentally observed yield of aerosol, (3) the standard deviation on the Gaussian distribution that best fits the data after the first two items have been set, and (4) the depth of the char particle over which 2 μm inclusions are assumed to be released without agglomeration. The first and second items are obtained manually from the data. Items 3 and 4 are obtained by optimizing the fit between the data and the model. This was done by comparing the deviation between the model and the data, using the sum of squares at discrete intervals as the optimization tool. Items 3 and 4 were determined sequentially. First, the Gaussian fit parameter was determined. With this set, the depth of 2 μm inclusion release was found. The algorithm which performed this optimization was written during the course of this program.

4.2.3 Ash from Raw Coals

Predictions by the final model (including ash vaporization, Gaussian breakup, and release of 2 μm inclusions) are plotted in Figures 4-6, 4-7 and 4-8. Predictions which account for both the vaporization / condensation mechanism and for Gaussian breakup (the "No Inclusions" lines in Figures 4-6 through 4-8) are substantially better than those by the simple breakup model. The predictions in Figures 4-6 and 4-7 which account for vaporization / condensation, Gaussian breakup, and for the release of 2 μm inclusions appear at first to offer only a slight improvement over just the dashed lines. The improvement is, however, significant, when the logarithmic axis is considered. Note that agreement between model predictions and data for the Beulah coal, Figure 4-8, is excellent when just the vaporization / condensation and Gaussian breakup mechanisms were included in the model. Accounting for the release of 2 μm included mineral matter would be inappropriate since this coal is known to hold its mineral matter primarily through molecular bonding to carboxyl groups in the macerals, and as very large pyrite particles (Huffman *et al.*, 1990).

Also given in Figures 4-6 and 4-7 are the surface thickness of the char particle over which inclusions are allowed to be released without coalescence. These are 0.5 μm for the Eagle Butte coal and 0.25 μm for the Illinois coal. Many factors could influence this number, including the degree to which grinding has left portions of particles exposed, the number of inclusions released during grinding that are loosely attached to the surface, or the level of perimeter fragmentation. Varying degrees of absorption of small inclusions by excluded mineral matter at the surface could occur depending on the disposition of the large excluded mineral matter. The critical point is that the behavior of the mineral matter within a quite small depth from the surface of the coal particle is sufficient to significantly perturb the size distribution of the fine ash.

4.2.4 Ash from Processed Coals - Cleaned Coals

Two bituminous coals and one lignite were subjected to a physical coal cleaning process (froth floatation, Hazen Research, Inc., Golden, Colorado). The cleaning is applied in the four stages illustrated in Figure 4-9 for the Illinois coal, which resulted in five cuts. Figure 4-9 also shows how 100 gm of original coal, and its associated mineral matter, are distributed between the cuts. The majority of the coal was deposited in the Third Cleaner Concentrate, and its mineral content was reduced to 55 percent of that of the original coal. The other four cuts represent relatively small fractions of the original coal mass and are highly enriched in minerals. Only three stages of cleaning were applied to the Utah coal and the Beulah lignite. Note that this froth floatation process is generally only effective at removing excluded mineral matter from coal; mineral inclusions, and inorganic species that are chemically bound into the organic matrix are largely untouched.

Figure 4-10 compares the differential size distribution plots for the raw Utah coal and the cleaned Utah coal. The results show that the 2 μm mode is undiminished by the coal cleaning process.

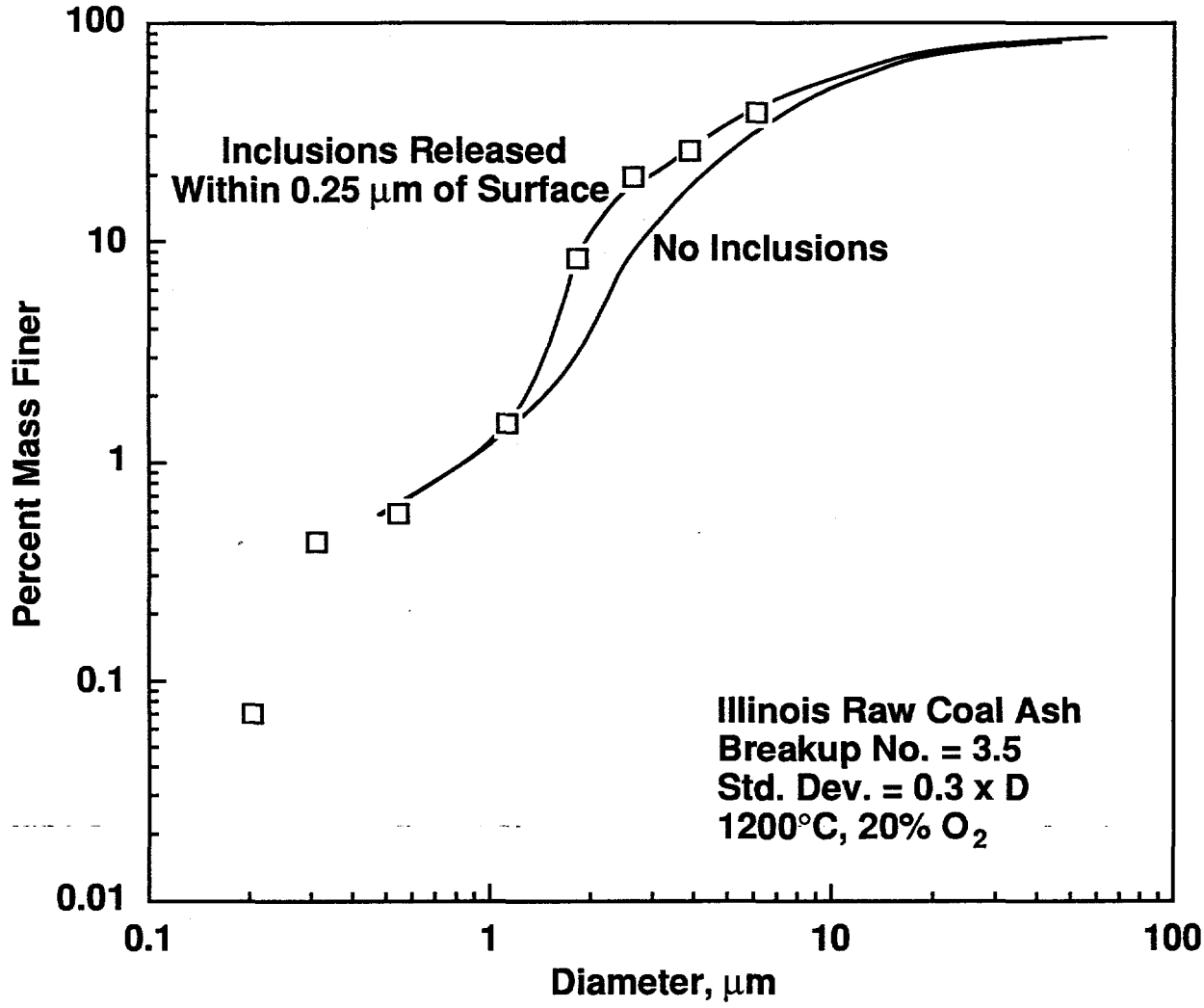

Figure 4-6. Comparison of data from Illinois coal and the modified breakup model.

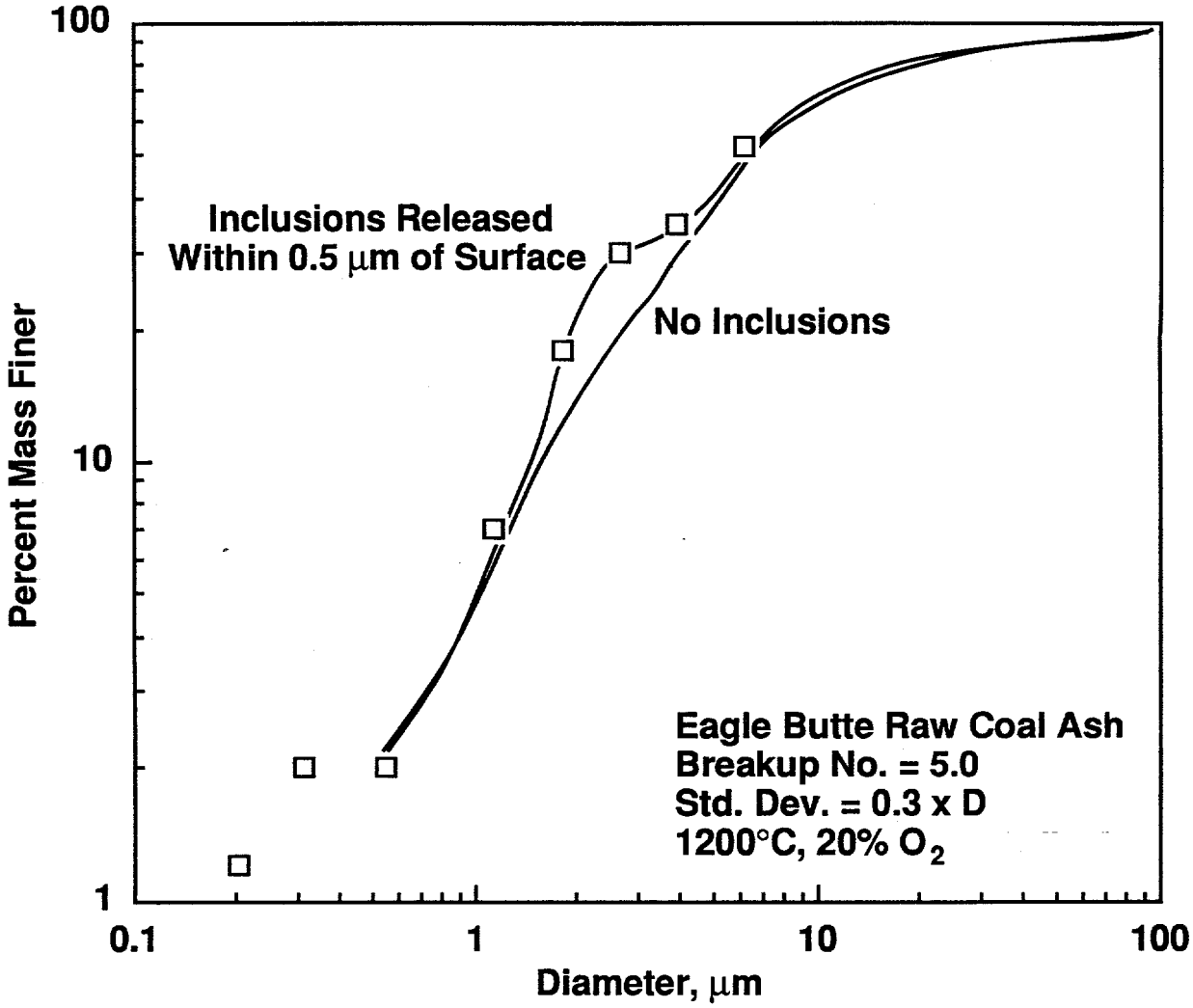

Figure 4-7. Comparison of data from Eagle Butte coal and the modified breakup model.

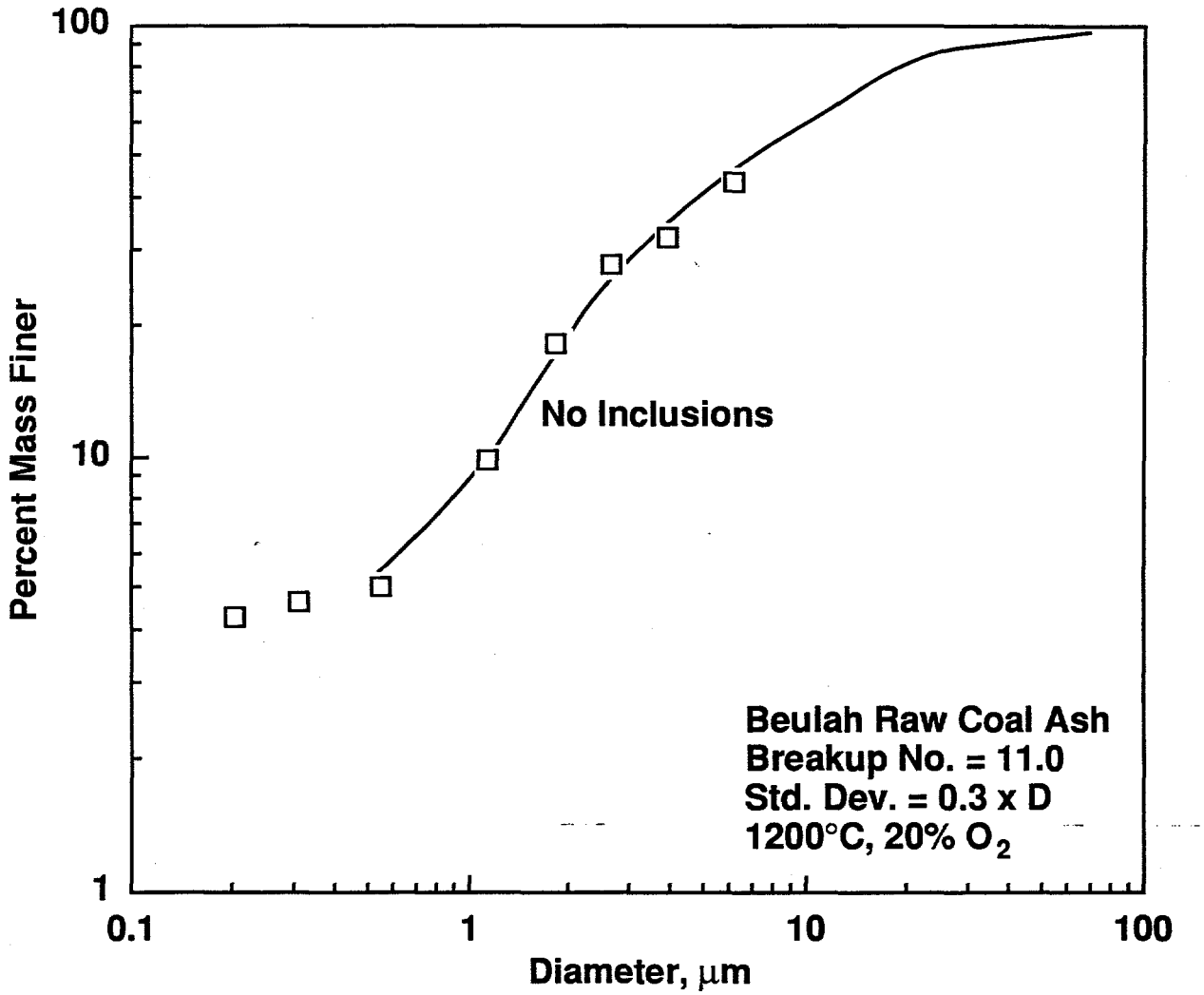

Figure 4-8. Comparison of data from Beulah coal and the modified breakup model.

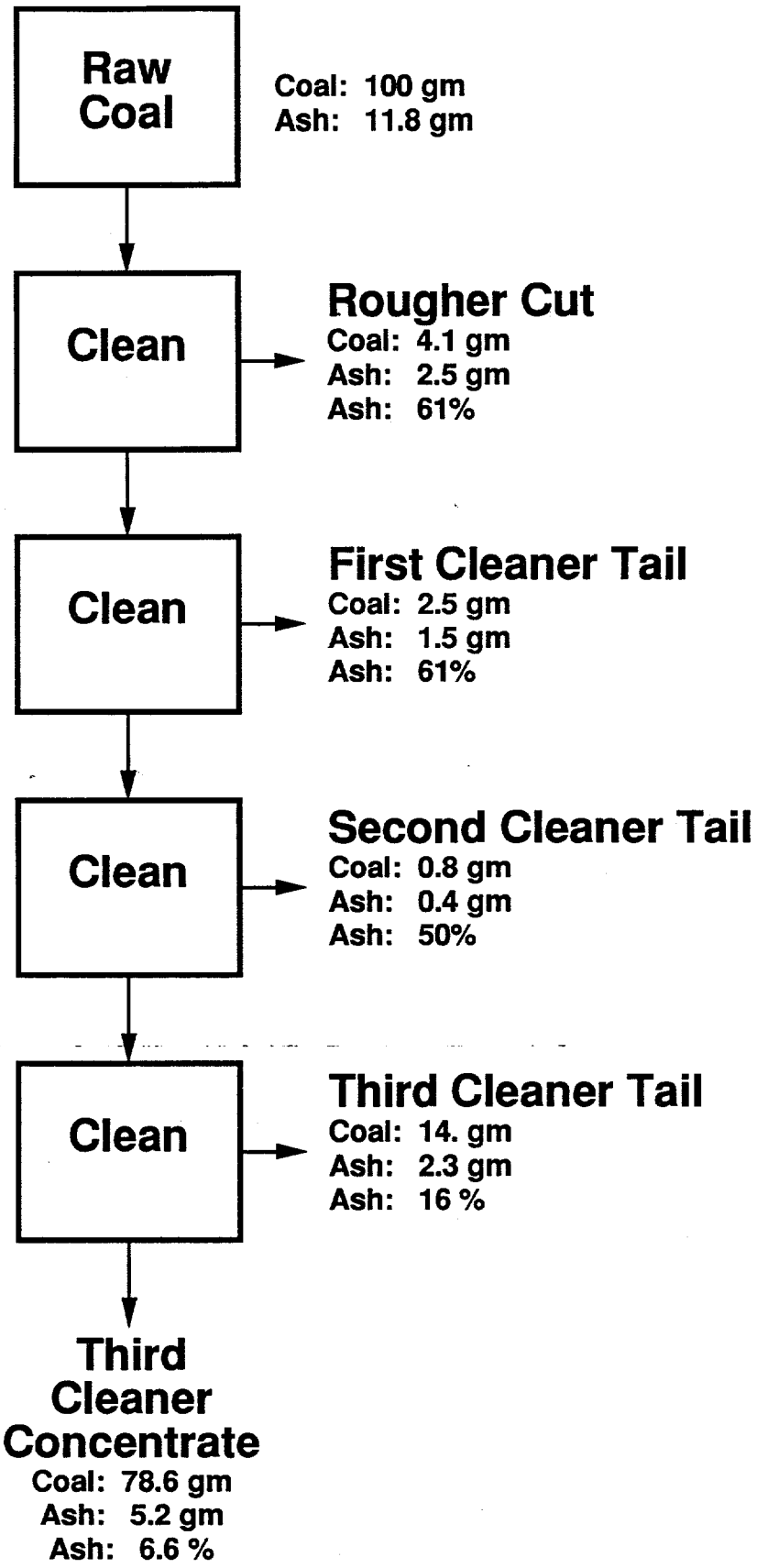

Figure 4-9. Schematic of the cleaning process for the Illinois coal.

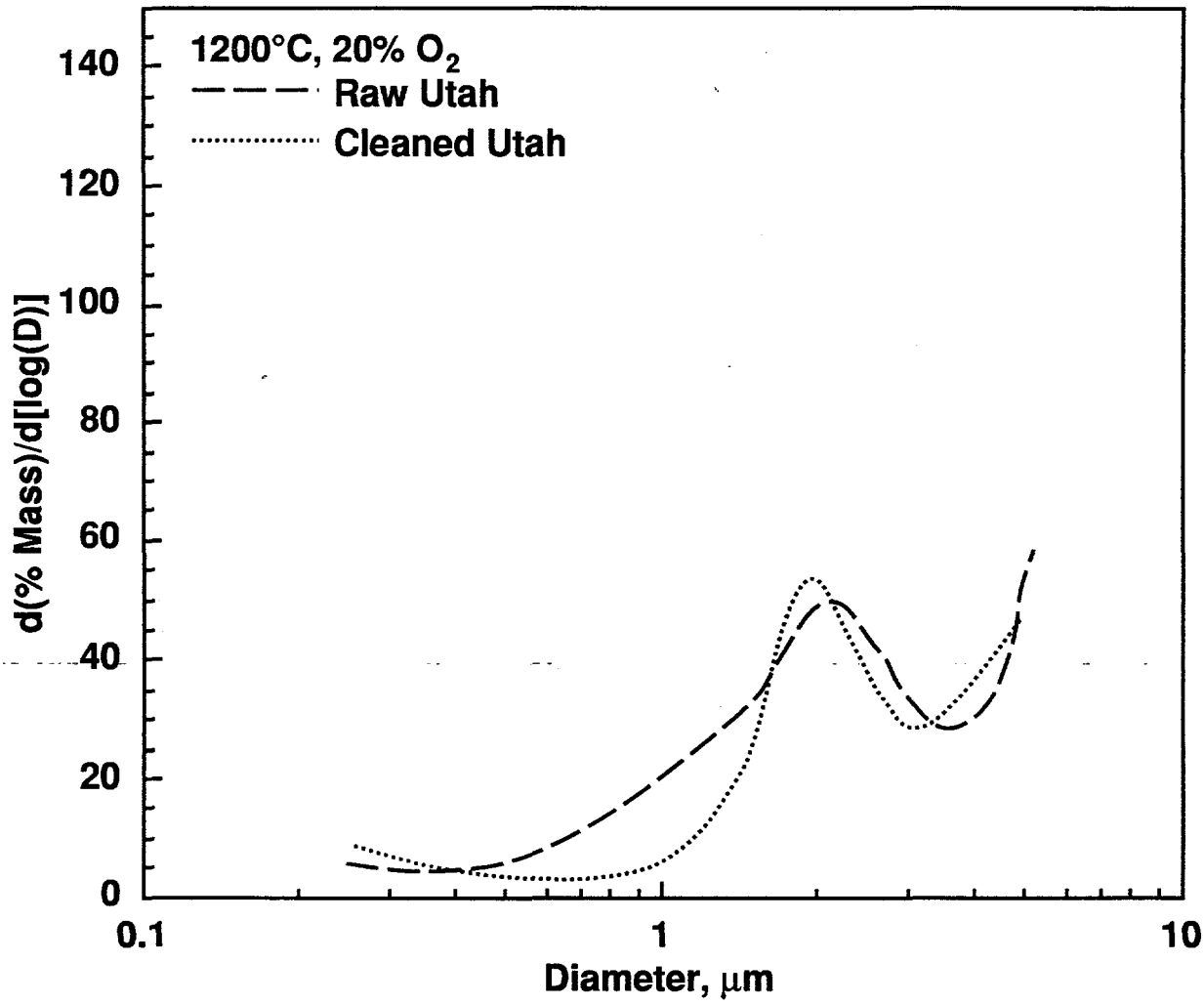

Figure 4-10. Differential size distributions of ash from raw and cleaned Utah coal.

This suggests that this mode is due to included mineral matter that escapes agglomeration, and not due to excluded minerals that would be removed by the cleaning process.

4.2.5 Ash from Processed Coals - Sized Coals

This set of experiments involved separating both the raw and cleaned coals into different size cuts and measuring the resultant ash size distributions. This was done for the raw Utah and Illinois coals and the cleaned Utah and Illinois coals. These coals were nominally sized into -18 μm, 18-37 μm, 37-85 μm, and +85 μm size cuts by aerodynamic classification (Vortec Model C-1 Particle Classifier on 15 kg batches of the original coals). The mass median diameters and ash content of each of the cuts is shown in Table 4-3.

Ash size distributions for the cleaned Utah size cuts are shown in differential form in Figure 4-11. The fraction of ash residing on the topmost stage of the impactor increased with increasing coal size, as would be expected from the breakup model. (This is indicated by the fact that most of the area under the curve for the +85 μm cut is off the right side of the plot.) The 2 μm mode is clearly visible for the smaller size distributions, although it becomes less evident for the larger size cuts. Similar behavior was observed in all the coals tested here. This is generalized in Figure 4-12, which plots the height of the 2 μm peaks as a function of coal size. This figure shows a consistent trend of decreasing peak height as the coal particle size is increased. These observations are consistent with the hypothesis that the source of the 2 μm mode is mineral matter near the surface of the coal particle which is released during the early stages of char combustion, either through shedding or fragmentation. Figure 4-12 also contradicts the hypothesis that the source of the 2 μm mode is mineral matter released during grinding, because this excluded material is removed from the cleaned coals. If this material were the source, then the cleaned coals would not show a 2 μm mode.

Both the original and modified breakup model were applied to the ash size distributions developed from the 16 coals (each size cut of raw and cleaned Illinois; raw and cleaned Utah). Table 4-3 shows the optimum breakup numbers for the unmodified model. The breakup number consistently increases to very large values for the largest coal particles. This tends to reduce, but not eliminate, the difference in ash size distribution between the largest and smallest coal fractions. The difference in breakup number does not, however, explain the disappearance of the 2 μm mode for the largest particles. The variations in the breakup number does, however, suggest the importance of the microfragmentation events noted by Helble and Sarofim (1989). These events, if independent of diameter, would tend to reduce the differences in ash size between coals of various original starting diameters.

The modified breakup model was also applied to each size cut. The fit for all of the smaller sized materials was excellent, while the fit for the larger sized particles was less good. In particular, the larger sized particles appeared to produce more aerosol. This would be expected because the longer burnout times required by the larger particles would provide more opportunity for the vaporization / condensation process to occur.

4.2.6 Ash from Processed Coals - Grinding

The Utah raw coal was ground to four different size cuts: -20 μm, 20-40 μm, 40-80 μm and +80 μm. The process involved grinding four separate batches (initially size greater than 1 cm) through a ball mill until the appropriate size range was reached. The differential ash size distribution resulting from the firing of these coals is shown in Figure 4-13. Some trends in Figure 4-13 are similar to those seen when a single grind of the same coal was aerodynamically sized. In particular, the 2 μm mode appears most prominently for the smaller sized coal particles, as was the case for coal subjected to sizing alone. If the ash size distributions are compared with those of the same coal aerodynamically classified to approximately the same size, one difference is in the yield

Table 4-3.
Properties and Breakup Numbers of Sized Coals

Nominal Size Cuts	<18 μm	18-37 μm	37-85 μm	>85 μm
Coal - Mass Median Diameter (μm)				
Utah Raw	16	30	60	140
Utah Cleaned	17	32	55	133
Illinois Raw	13	30	60	143
Illinois Cleaned	16	28	62	132
Coal - Ash Content (%)				
Utah Raw	7.7	4.9	6.4	5.5
Utah Cleaned	2.3	2.2	2.4	2.9
Illinois Raw	17.1	10.4	9.9	8.9
Illinois Cleaned	7.2	6.4	5.9	5.4
Optimized Breakup No.				
Utah Raw	1.8	7	50	200
Utah Cleaned	1.8	1.8	1.8	50
Illinois Raw	1	9	300	300
Illinois Cleaned	3.5	7	30	100

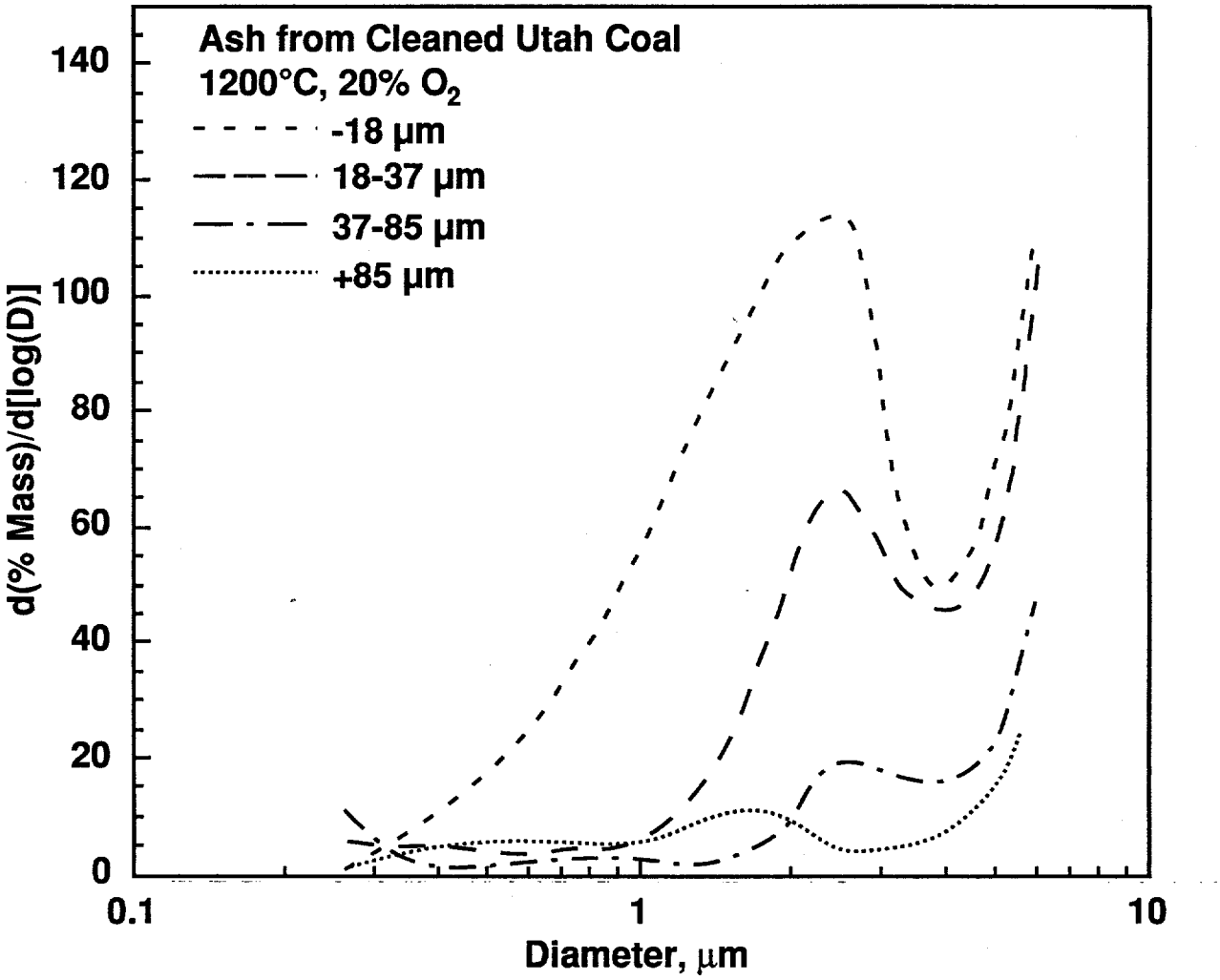

Figure 4-11. Differential ash size distributions for four size cuts of cleaned Utah coal.

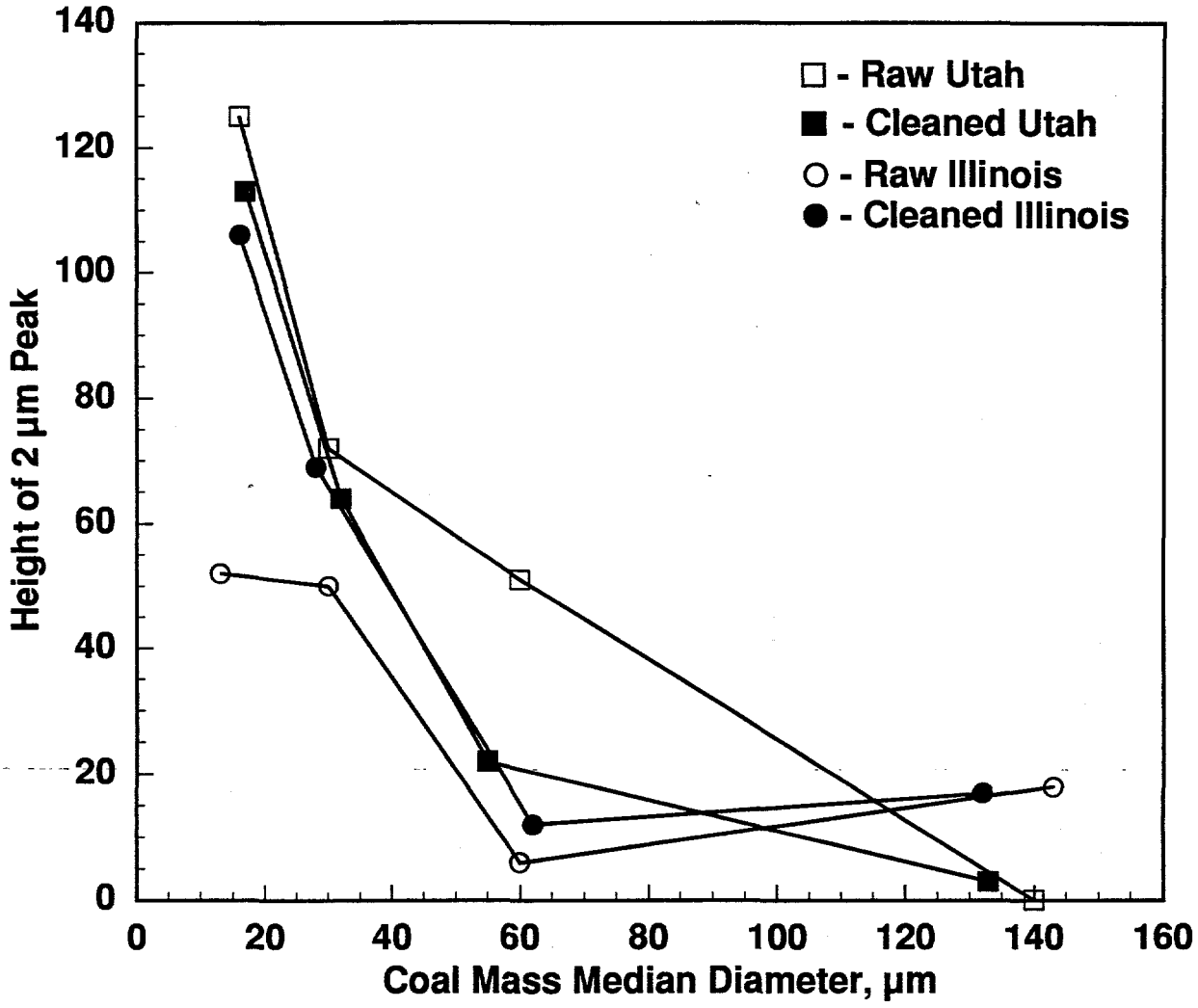

Figure 4-12. Heights of 2 µm peaks from differential size distributions for a series of sized raw and cleaned coals.

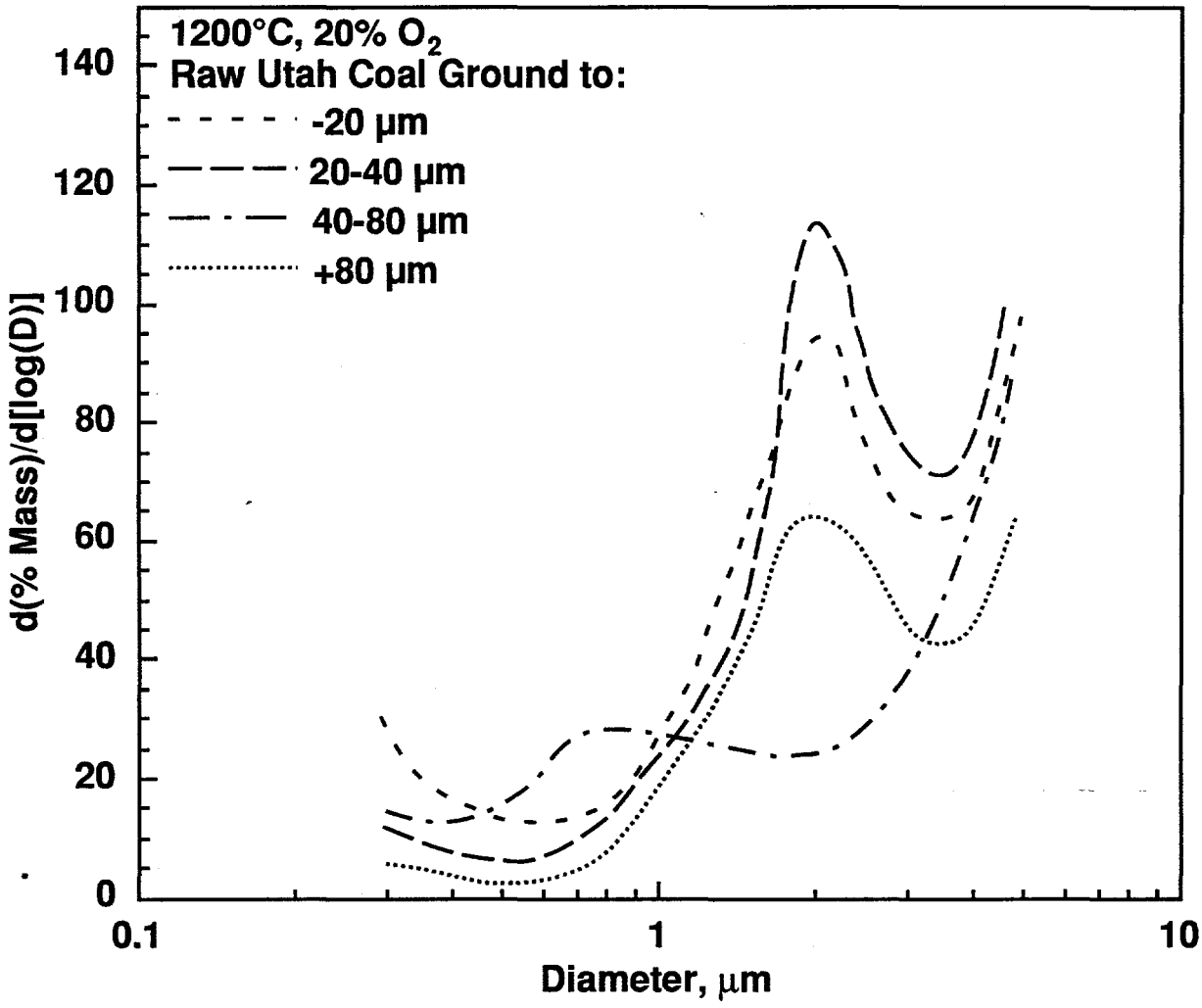

Figure 4-13. Differential size distributions of Utah coal ground to various sizes.

of aerosol. In particular, the smaller coal particles prepared by sizing yielded much more aerosol than the small size cuts prepared by grinding. Analysis of samples shows that much more excluded mineral matter is present in the fine coal prepared by sizing. This occurs because much of the fine excluded mineral matter produced during the initial grinding process is concentrated into the fine coal during size classification, it being ground to a finer size in the recycle mill. As discussed below, the presence of excluded mineral matter acts to suppress aerosol formation.

4.2.7 Discussion of Residual Ash Results

The ash size distribution of a broad range of coals was correlated with the breakup model. Consistent with earlier studies, the breakup numbers are relatively insensitive to combustion temperature and free-stream oxygen, but increase substantially for low-rank coals. Examination of the performance of the model below 8 μm shows that ash yields are significantly higher than predicted. After the breakup model is empirically corrected to account for aerosol production and is modified to allow the production of a distribution of ash particles from each coal particle, a discrete mode at 1-2 μm remained. The persistence of this mode throughout most of the data indicates a specific mechanism is responsible. The similarity between the size of this mode and that of the inherent mineral inclusions suggests a connection.

This 2 μm mode is undiminished in coals cleaned of excluded mineral matter, which shows that the source is not from inclusions that are liberated during grinding. Tests with size classified coals showed the 2 μm mode to be most prevalent from the finest coals. It had largely vanished for coals whose original size was greater than 85 μm. This indicates a phenomena related to the original external surface area of the coal particles (*e.g.*, shedding of inclusions near the original char surface). This suggests that the 2 μm mode is not formed by microfragmentation at the surface of the burning char particle, *unless* the duration of the microfragmentation is limited to only the early stages of char combustion. In this case, the amount of 2 μm material produced would respond to particle diameter (*i.e.*, surface-to-volume ratio) as suggested by the data.

The largest coal sizes developed large breakup numbers, suggesting that the scale of the microfragmentation events noted by Helble and Sarofim (1989) is not a strong function of coal size. Results from grinding the coal to various degrees did not produce a significant difference in the global behavior of the ash, with one exception. The yield of aerosol from the finest *ground* coal exceeded that from the finest *sized* coal. Analysis suggests that the finest sized coal collects a greater share of the excluded mineral matter during the sizing process. The additional excluded minerals apparently act to suppress aerosol formation, as noted below.

These results several practical implications. First, the study shows that several forms of pretreatment can modify the emission and character of environmentally sensitive PM10. In particular, the use of either coal cleaning or coal aerodynamic sizing can substantially increase ash aerosol emissions. Alternately, fine grinding of coal appears to reduce ash aerosol yields due to the liberation of aerosol-suppressing excluded mineral matter during grinding. While the yield of particles in the 1-2 μm range is not affected by cleaning, it is strongly influenced by the size of the coal. Thus, deeper grinding assists the reduction of aerosol emissions, but increases the 1-2 μm mode. One can speculate that the reduction of the hazardous aerosol more than offsets the marginal increase in the 1-2 μm mode, particularly since the latter is more easily captured.

4.3 Aerosol Yields

The previous section showed that coal pretreatment influenced ash behavior. It also suggests that the pretreatment changes aerosol yields. This is further explored in this section, which used the same cleaned and sized coals discussed above.

Figure 4-14 shows the cumulative size distribution that resulted from firing each of the Illinois

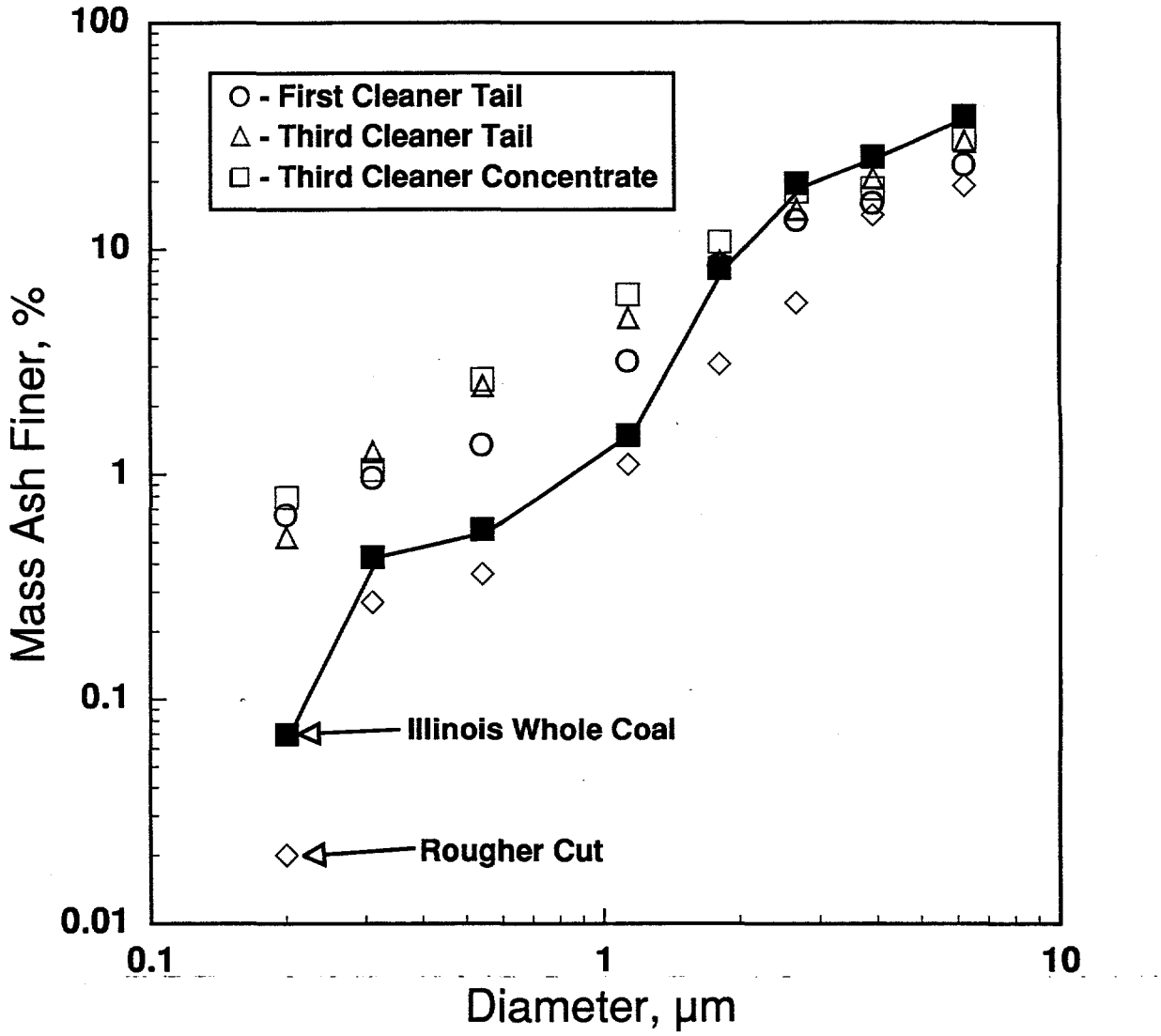

Figure 4-14. Impactor data for the parent Illinois coal and its various cleaned fractions.

bituminous coal cuts (too little Second Cleaner Tail was recovered to permit its firing). The rougher cut (the ash-rich material removed from the initial cleaning step) produced the coarsest ash, while all the remaining cuts yielded similar ash size distributions and substantially more material under 0.5 μm. This is surprising, since the rougher cut and the First Cleaner Tail have identical mineral content - 61 percent - and very similar original particle size distributions. When fired, however, the amount of fines produced by each of these two cuts is substantially different. The whole coal produced a yield of fine particles that was intermediate between that produced by these two cuts.

Figure 4-15 was prepared to determine whether the ash size distribution for the whole coal deviated from that of the weighed sum of the individual fractions. (The experimental uncertainties shown on the figure are based on both the accuracy and precision of the measurement techniques, and on the repeatability observed during duplicate runs.) The figure compares the percent of mass found on each of the impactor stages for the whole coal, with that for the weighed sum of all the individual coal fractions. Thus, if no synergism exists, the sum of the individual fractions should equal that of the parent coal. Figure 4-15 shows that the yield of particles under 0.5 μm has been substantially enhanced. In particular, the catch on the backup filter (nominally plotted as 0.11 μm) shows over an order of magnitude increase due to partitioning of the coal. Figure 4-14 suggests that it is the presence of the rougher cut that is responsible for suppressing fines formation for the whole coal.

Figure 4-16 shows a similar plot for the Utah coal, except here the raw coal is compared against only the cleaned fraction. Again, the cleaned coal exhibits a substantial increase in the formation of particulate matter under 0.5 μm in diameter. Qualitatively, these results are consistent with earlier work showing that the organically bound or included mineral matter is the source of the aerosol (Helble and Sarofim, 1989). The results, however, suggest that the presence of at least certain types of excluded mineral matter can act to suppress the formation of fine particles and aerosol.

Beulah lignite was also cleaned. The resulting fractions had little deviation in mineral content from the parent coal. This is a consequence of the fact that more of the inorganic species are atomically bonded to carboxylate groups in the coal, or are present as very small discrete mineral inclusions (Huffman *et al.*, 1990). The only large mineral particles present are associated with pyrite (Helble *et al.*, 1990). Each of the cleaned fractions yielded essentially identical ash size distributions as the parent coal upon firing.

This western lignite yields substantially more aerosol than the bituminous coals. This is a partly a consequence of the high level of molecularly bonded sodium in the Beulah, which is easily vaporized. In addition, the certain acid minerals in the Utah and Illinois coals can become converted to basic species under the reducing environment within the burning char. This potentially moves the acid/base ratio closer to unity, and thus increases the likelihood for local melting of the ash. The melt can then absorb vapors that would otherwise form aerosol, thus reducing the aerosol yield from the Utah and Illinois coals relative to the Beulah.

Both the Utah and Illinois coals were aerodynamically sized into the following nominal size cuts: >85 μm, 37-85 μm, 18-37 μm, and <18 μm. At the same time, the cleaned versions of both these coals were also size segregated into these same cuts. Figure 4-17 shows the ash size distributions that resulted from the firing of the sized Illinois coal, along with the size distribution of the ash from the firing of the parent coal. It is immediately obvious that the sizing process has caused the individual cuts to yield substantially more fine particulate matter than the parent coal. A similar experiment was performed for the cleaned coal. In contrast, this showed that the ash size distribution for the original cleaned coal was not significantly different from the ash size distribution obtained by taking a weighed average of the results from the individual size cuts. Thus, it would appear that an inherent means of suppressing fines formation is also removed by the sizing process.

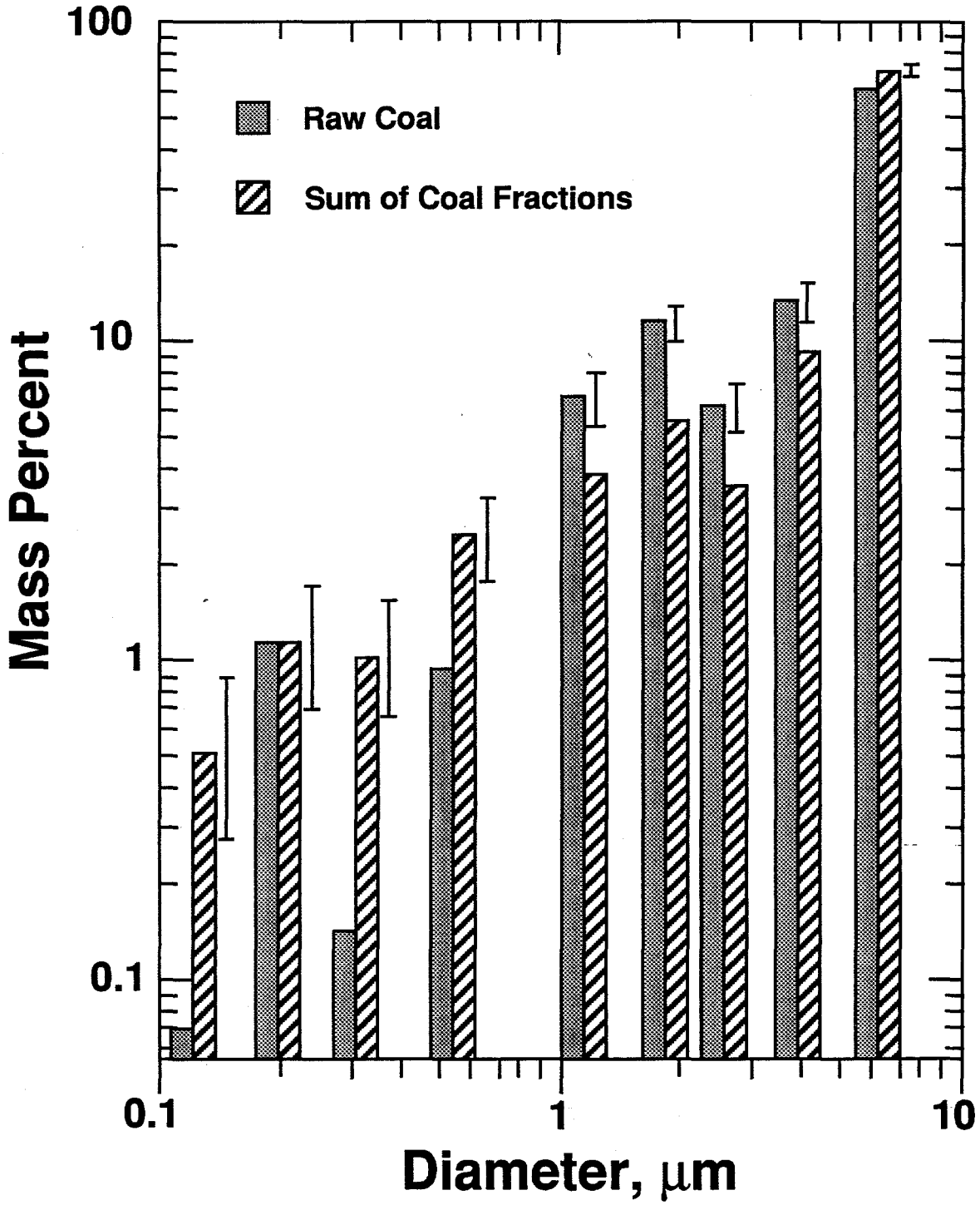

Figure 4-15. Impactor data for ash from the raw Illinois coal and from the weighed sum of the individual coal fractions.

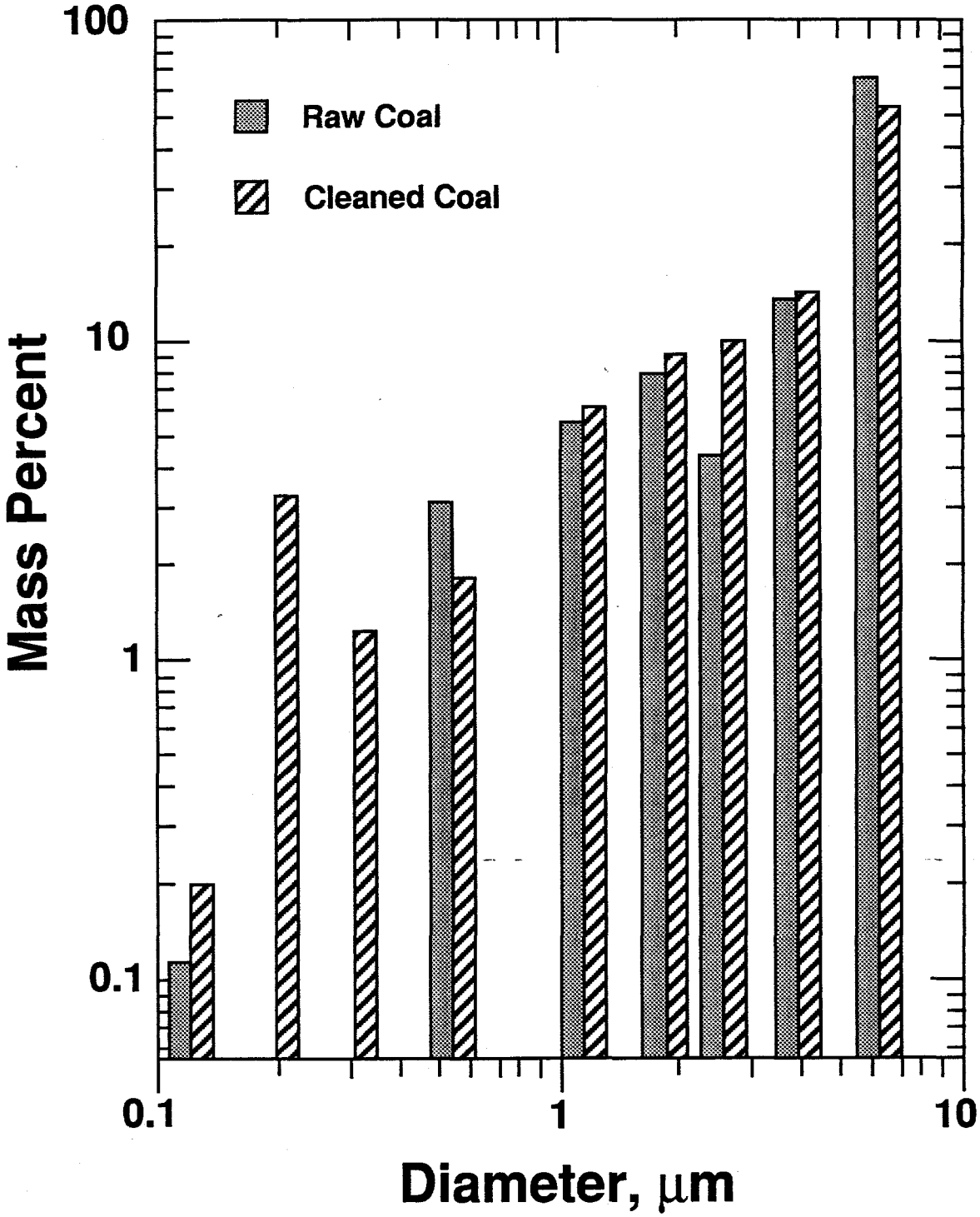

Figure 4-16. Impactor data for ash from the raw Utah coal and the cleaned Utah coal.

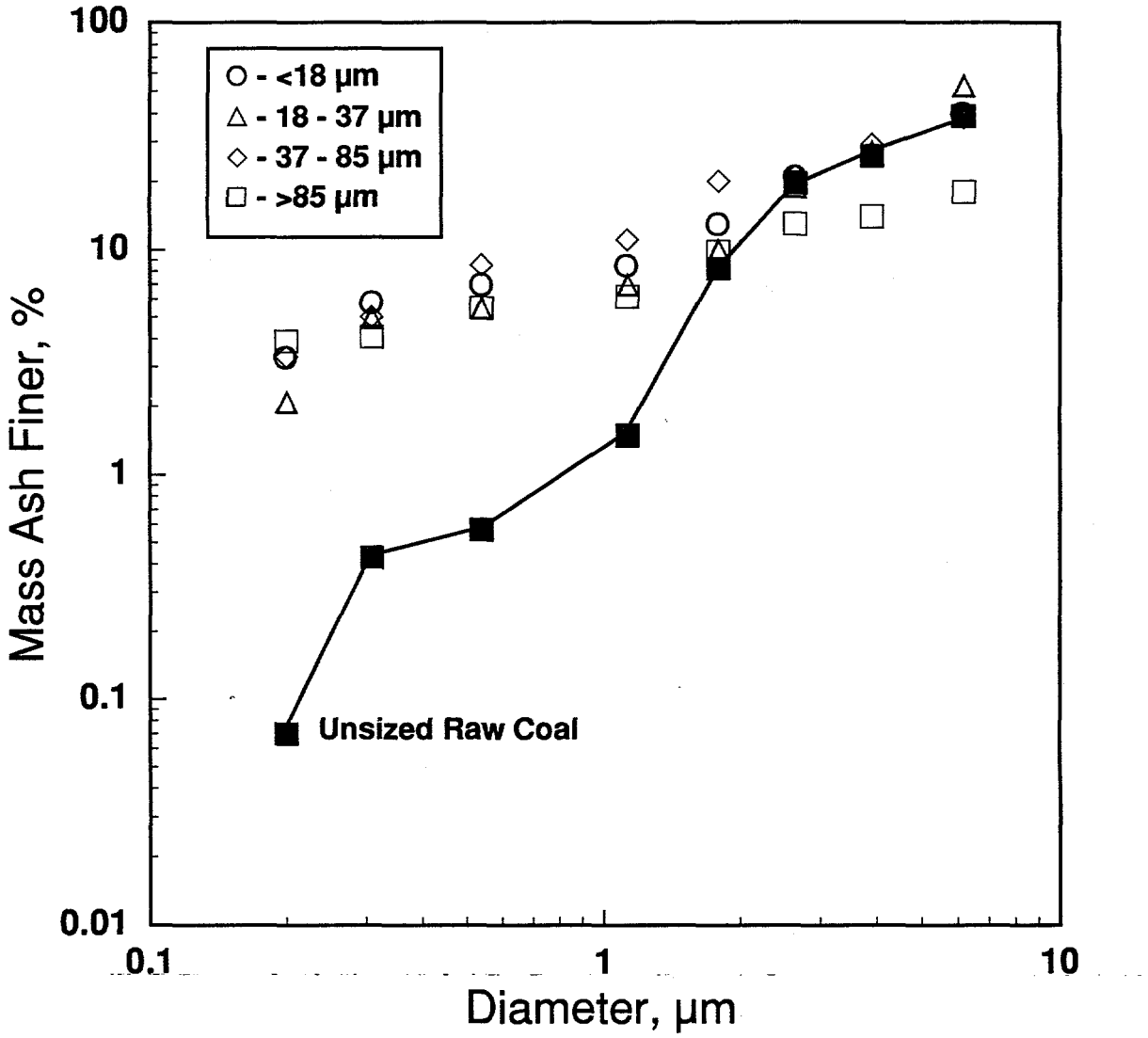

Figure 4-17. Impactor data for ash from the sized Illinois coal and the unsized parent coal.

A special coal mixture was prepared in which 90 percent Beulah lignite was mechanically mixed with 10 percent of the rougher cut from the Utah coal. The ash size distribution for this material was compared with that obtained from the firing of straight Beulah in order to identify whether contacting with the rougher cut would change the Beulah ash size distribution. The Beulah coal is high in minerals that are well dispersed within the macerals, particularly sodium, and yields substantial aerosol upon firing. Thus, it resembles the cleaned bituminous coals in its reduced fraction of excluded mineral matter. Figure 4-18 shows the ash size distribution from firing straight Beulah and the Beulah/rougher cut mix. The results show that the amount of fine material (below 0.5 μm) was reduced by 50 percent, although the rest of the size distribution was unaltered. The degree of fines reduction was not as great as that observed for the bituminous coals, possibly because the degree of contacting between excluded minerals and coal was more "casual," or because of the high sodium content of the Beulah mineral matter. In any case, the presence of the mineral-rich rougher cut acted to suppress fines formation.

4.4 Discussion

The ash size distribution of a broad range of coals was correlated with the breakup model. Consistent with earlier studies, the breakup numbers are relatively insensitive to combustion temperature and free-stream oxygen, but increase substantially for low-rank coals. Examination of the performance of the model below 8 μm shows that ash yields are significantly higher than predicted. After the breakup model is empirically corrected to account for aerosol production and is modified to allow the production of a distribution of ash particles from each coal particle, a discrete mode at 1-2 μm remained. The persistence of this mode throughout most of the data indicates a specific mechanism is responsible. The similarity between the size of this mode and that of the inherent mineral inclusions suggests a connection.

This 2 μm mode is undiminished in coals cleaned of excluded mineral matter, which shows that the source is not from inclusions that are liberated during grinding. Tests with size classified coals showed the 2 μm mode to be most prevalent from the finest coals. It had largely vanished for coals whose original size was greater than 85 μm. This indicates a phenomena related to the original external surface area of the coal particles (*e.g.*, shedding of inclusions near the original char surface). This suggests that the 2 μm mode is not formed by microfragmentation at the surface of the burning char particle, *unless* the duration of the microfragmentation is limited to only the early stages of char combustion. In this case, the amount of 2 μm material produced would respond to particle diameter (*i.e.*, surface-to-volume ratio) as suggested by the data.

The largest coal sizes developed large breakup numbers, suggesting that the scale of the microfragmentation events noted by Helble and Sarofim (1989) is not a strong function of coal size. Results from grinding the coal to various degrees did not produce a significant difference in the global behavior of the ash, with one exception. The yield of aerosol from the finest *ground* coal exceeded that from the finest *sized* coal. Analysis suggests that the finest sized coal collects a greater share of the excluded mineral matter during the sizing process. The additional excluded minerals apparently act to suppress aerosol formation, as noted below.

The mechanism by which coal cleaning and aerodynamic sizing acts to increase aerosol yields is not presently known. To explore the possibilities, the mechanisms of aerosol formation must be briefly reviewed.

Alkali metals, in particularly sodium, are a major source of aerosol. When these are molecularly bonded into the macerals, they can undergo rapid vaporization during char combustion (Raask, 1985). A second means of vapor generation is based on the work at MIT (Quann and Sarofim, 1992; Graham *et al.*, 1991). This model provides for the vaporization of Fe, Si, and Al species from both molecularly bonded species and from inclusions. During char combustion, the interior of the char is fuel-rich, and the minerals at the surface of the inclusions undergo a reaction with CO

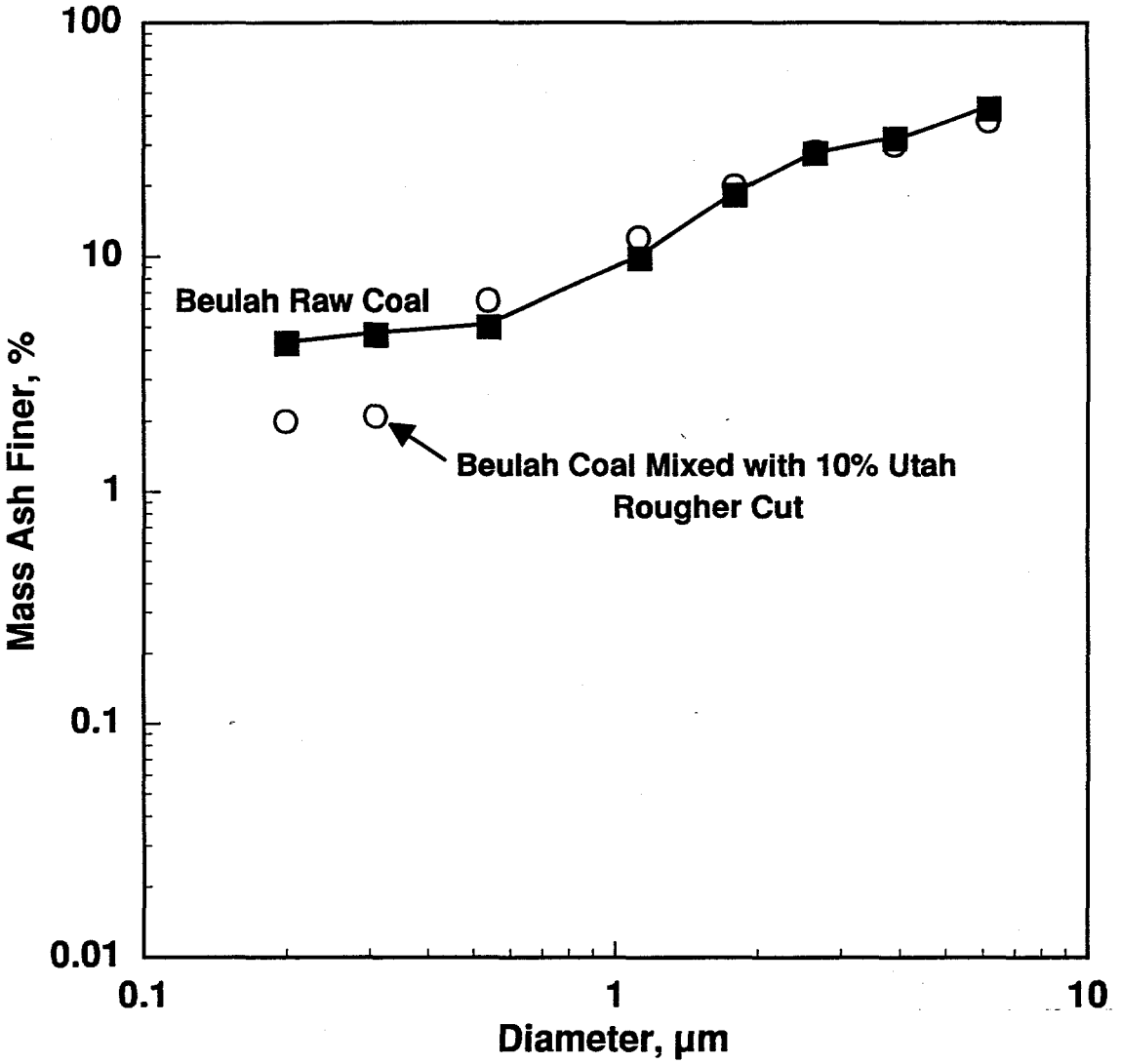

Figure 4-18. Impactor data for ash from raw Beulah lignite, and for the lignite mixed with 10 percent of the Utah Rougher Cut cleaning fraction.

and C to produce an equilibrium vapor pressure of metals and suboxides at the inclusion surface. The rate at which minerals are vaporized and leave the particle becomes a combination of the rate of diffusion from the inclusion into the bulk of the char, and the diffusion rate from the char bulk to the char surface. In both mechanisms, once the vapor is released from the char particle, it is quantitatively oxidized and condensed into aerosol.

The literature shows considerable evidence that sodium that would otherwise be vaporized can become tied up in aluminosilicate complexes and retained in the residual ash (Huffman *et al.*, 1990). Reactions between sodium vapor and silica have been studied in some detail (Linder and Wall, 1990), and the use of clay minerals has been explored as a means of absorbing sodium vapor in low-rank coal from the western U.S. (Gallagher *et al.*, 1991). One suggestion is that the some of the excluded minerals are loosely attached to the coal macerals. During firing, these may form melts on the char surface, and act as sinks for mineral vapor, be it sodium, or other minerals (Si, Al, Fe). Coal cleaning will remove at least some of these loosely attached excluded minerals and reduce this source of vapor absorption.

The second possibility represents a slight alteration on the first. Here, the role of the excluded minerals is to reduce the fusion temperature of the ash. The assumption is that the minerals cannot absorb vapor unless they have melted. Promotion of melting can occur if the excluded minerals act as a fluxing agent. Alternately, the excluded minerals can shift the acid/base ratio away from strongly acidic or strongly basic conditions, and towards unity. In both cases the fusion temperature will be reduced (Huffman and Huggins, 1990). Thus, the removal of the excluded minerals may reduce the tendency of the included minerals to form a melt as the char burns. If a melt is not formed, then vapor cannot be absorbed and aerosol formation will not be suppressed.

An third alternative is suggested by the experiments of Mitchell (1990) who observed a significant correlation between coal mineral content and char burning temperature. The presence of the excluded minerals could significantly reduce aerosol yields since yields depend strongly on char combustion temperature.

Thus, the nature of the mineral matter associated with each of the coals, and the nature of the mineral matter that is removed or disturbed in the cleaning and sizing processes is critical to understanding the mechanism. To this end, proximate analyses were obtained on each of the coals (Table 4-1). In addition, elemental ash analyses were obtained for the original coals, the cleaned coals, and the rougher cut (the first fraction removed in the cleaning process). These are shown in Table 4-4. Although mineral forms were not determined in this study, literature values are available for two of the coals, Illinois and Beulah (Helble *et al.*, 1990). These are shown in Table 4-5, along with brief notes describing the coal minerals.

Cleaning of the Beulah lignite did not change the emission of aerosol. When the lignite was mixed with the rougher cut cleaning fraction from the Utah coal, aerosol yields were suppressed to a degree. This suggests that the excluded mineral matter from the lignite (for the most part large pyrite particles) was ineffective at preventing aerosol formation. The relatively limited success of the rougher cut in reducing aerosol yields may be due to (1) ineffective contacting between the rougher cut and the lignite, or (2) increased difficulty in suppressing aerosol formation when sodium is the dominant source rather than other minerals.

Examination of Table 4-4 shows no consistent enrichment or depletion of any of the mineral elements in the cleaned or rougher cut fractions. Since the elemental composition of the minerals in the various fractions is fairly constant, one mineral element does not appear to be responsible for the behavior. One possibility is that the specific form of the minerals (*e.g.*, as shown in Table 4-5) becomes segregated by the cleaning process, although data are not yet available to test this hypothesis. Alternately, the cleaning process may have disturbed the contacting between the macerals and the excluded minerals such that aerosol suppression is prevented. Evidence is

Table 4-4
Elemental Analysis of Mineral Content by Percent Mass

	Illinois			Utah		
	Raw	Cleaned	1st Tail	Raw	Cleaned	Rough
SiO_2	51.1	53.9	54.4	56.3	50.4	64.7
Al_2O_3	20.0	22.0	21.7	18.4	19.0	16.8
TiO_2	0.94	1.4	0.64	0.88	1.9	0.62
Fe_2O_3	12.9	14.5	12.3	6.1	8.1	5.3
CaO	5.9	1.8	4.1	6.0	5.8	4.4
MgO	1.2	1.4	1.4	1.2	0.53	1.1
Na_2O	1.1	0.93	0.54	2.1	3.9	1.6
K_2O	2.1	2.3	2.1	1.6	1.1	1.1
P_2O_5	0.29	0.27	0.35	0.44	0.81	0.34
SO_3	5.0	1.0	3.1	7.0	5.5	3.6

Table 3
Mineral Composition by Mass Percent
(Helble *et al.*, 1990)

	Beulah	Illinois
Pyrite	26	28
Quartz	12	20
Illite	1	10
Kaolinite	30	6
Calcite	-	7
Montmorillonite	1	-
Mixed Silicates	13	18
Acid Soluble Na (ppm)	7500	2200
Acid Soluble Ca (ppm)	14,000	5800

Notes: Beulah: Consists of molecularly dispersed minerals, very small discrete inclusions, an large pyrite particles.

Illinois: Minerals are generally uniformly distributed among all inclusion size ranges. Pyrite tends to be concentrated into larger particles.

available that supports both of these interpretations, as follows.

Change in Mineral Forms. The fact that the rougher cut, when fired alone, yielded very little aerosol suggests that this cut contains specific minerals that act to suppress aerosol formation. All of the other mineral-rich cuts yielded the same aerosol as the cleaned coal (Figure 4-14).

Disturbance of Contacting. When aerodynamic sizing was applied to the bituminous coals, all of the cuts showed enhanced aerosol yields relative to the parent coal. If one particular mineral was responsible for suppressing aerosol, and if it were concentrated into one cut, then that particular cut would be expected to show reduced aerosol production. The fact that all the cuts showed increased aerosol suggests that the contacting between the excluded minerals and the macerals has been disturbed, rather than a particular mineral has been removed.

These results several practical implications. First, the study shows that several forms of pretreatment can modify the emission and character of environmentally sensitive PM10. In particular, the use of either coal cleaning or coal aerodynamic sizing can substantially increase ash aerosol emissions. Alternately, fine grinding of coal appears to reduce ash aerosol yields due to the liberation of aerosol-suppressing excluded mineral matter during grinding. While the yield of particles in the 1-2 μm range is not affected by cleaning, it is strongly influenced by the size of the coal. Thus, deeper grinding assists the reduction of aerosol emissions, but increases the 1-2 μm mode. One can speculate that the reduction of the hazardous aerosol more than offsets the marginal increase in the 1-2 μm mode, particularly since the latter is more easily captured.

5.0 Coal Results from the Tunnel Furnace

5.1 Test Series Goals

One feature of the work reported in the previous section is the exclusive use of coals that are relatively high in sodium. The Utah coal is typical of western bituminous coals in that it is high in sodium. The Illinois No. 6 is also high in sodium, especially compared with other eastern bituminous coals. This raises the question of the degree to which the observations reported in the previous section are exclusive to high-alkali coals.

Some of the mechanisms associated with sodium release from coal char combustion have been addressed in the recent work by Gallagher (1992) and the review by Linak and Wendt (1993). These works, and the discussion presented above, suggest that sodium release is a complex process in which the fundamental vaporization mechanism competes with sodium capture by aluminosilicate mineral inclusions. Once captured, the sodium becomes complexed and either cannot be again released, or its release is delayed to much higher temperatures. Thus, the amount of sodium that is released as vapor to form aerosol is strongly dependent on the quantity and dispersion of the aluminosilicate inclusions.

This picture of the sodium vaporization process suggests additional interpretations on the work presented in the previous section. Since the sodium content within the mineral matter was relatively high for each of these coals, one hypothesis is that the bulk of our aerosol originated as sodium vapor. In the untreated coals (*i.e.*, before the froth floatation cleaning step) the coals may contain loosely attached aluminosilicate mineral matter on the surface of the macerals. These could act as sinks for sodium vapor. In addition, aluminosilicate inclusions within the char particle could also act as sinks for sodium vapor. In fact, if enough inclusions are present within the particle, the amount of sodium vapor reaching the surface could be significantly reduced.

Thus, a major goal of the present test series is to observe how aerosol yields and residual ash size distributions are altered by coal pretreatment when the parent coals are low in alkali minerals. This will allow a further narrowing of the number of interpretations of the data reported in the previous section.

5.2 Coal Selection

Following review of the Physical Science Technology coal suite analyses (Boni *et al.*, 1992), the following coals were selected for testing. One drum of each was received from Physical Science Technology Co., with the exception of the Beulah coal, where restricted supplies limited the shipment to a single small container. The coals are:

- Upper Freeport: This is a reduced sodium coal. It contains coarse pyrite particles that are readily washed from the coal.
- Kentucky No. 11: Also low in sodium. Contains fine pyrite particles, and is not easily beneficiated.
- Illinois No. 6: Used in previous testing. Relatively high in sodium, primarily as feldspar. Many fine pyrite particles.
- Beulah Lignite: Used in previous testing. Contains very high organically bound Na, so it is a good candidate for blending to test sodium vapor capture hypotheses.

Details of the analysis are provided in the PSI technical reports (Boni *et al.*, 1992).

5.3 Experimental Modifications

At the start of the present test series, the sampling location was changed from the first elbow of the exhaust system to directly below the furnace outlet. The original sampling location was selected for ease of access, while recognizing that some of the larger particles would be lost in the horizontal transition. The loss of the larger particles was not a problem since the work focused on direct aerosol yields. The revised sampling location was adopted out of a desire to obtain accurate size distributions for the measurements involving artificial chars (reported in Section 6).

To accommodate the new sampling location, a vertical probe was mounted into the bottom of the furnace, and the impactor was shifted from a horizontal to a vertical orientation.

Figure 5-1 shows data from a series of runs on Illinois No. 6 coal under both the former and present sampling configurations. No consistent change is noted for the smaller sized particles, but clearly a greater recovery of larger particles is noted for the furnace outlet sampling location. Mass balance calculations on the ash yields from the new furnace sampling location are generally closed to within 80-120%. Thus, the revised sampling location was adopted for all subsequent testing.

5.4 Raw, Cleaned and Sized Coals

This section presents aerosol yield data on the raw Illinois No. 6 coal, the Kentucky No. 11 coal, and the Upper Freeport coal. In addition, the Upper Freeport, Kentucky No. 11, and Illinois No. 6 were aerodynamically sized into four cuts at Vortec in Long Beach, California (using Vortec Model C-1 Particle Classifier into cuts nominally sized at <18 μm, 18-37 μm, 37-85 μm, and >85 μm). Due to high cost, only one of the new coals was cleaned by the froth flotation procedure at Hazen Laboratories in Golden, Colorado. This is the Upper Freeport, which was selected because (1) it has low sodium, unlike the other coals that were cleaned, and (2) it is a readily beneficiated coal. In the present case the excluded mineral consists of pyrite particles, which makes this coal similar to the previously tested Illinois No. 6. The aerosol yields from the cleaned Upper Freeport coal provide a good comparison with that from the cleaned Illinois.

Figure 5-2 shows aerosol yield data for the three raw coals. Each shows a distinct aerosol mode, with little mineral matter associated with the ~0.5 μm size range. The sodium-rich Illinois coal shows the most aerosol yield. The Kentucky No. 11 and Upper Freeport coals have essentially identical sodium contents, but show somewhat different aerosol yields. Figure 5-3 was generated to verify the repeatability of the impactor data. In this case, the Illinois No. 6 coal was run on three separate days. This shows that the experimental variability in the data was less than the major trends observed in the testing.

Figure 5-4 compares the size distribution for the raw Upper Freeport bituminous with that from the cleaned fraction. The cleaned coal shows no enhancement of aerosol yield, but it does show an increase in non-aerosol fine ash. This shows significantly different behavior compared with that obtained for the sodium-rich coals in which the aerosol yield is substantially increased for the cleaned fractions.

Each of the sized coals showed increased aerosol yield relative to the unsized parent raw coal. At present, only one size cut was tested for each of the sized coals: 37-85 μm. Figure 5-5 shows that aerosol yields more than doubled for the Illinois No. 6 sized coal. This same trend holds true for the Upper Freeport (Figure 5-6) and the Kentucky No. 11 (Figure 5-7). Interestingly, for each of the latter two coals, the yield of ash in the 1-2 μm size range was substantially suppressed for the sized coals (see Figures 5-8 and 5-9). Yield of ash in this size range has previously been correlated with the release of unagglomerated mineral inclusions as the char burns (Helble and Sarofim, 1989). The fraction of ash released as these inclusions has been correlated with char size, which has been interpreted as indicating that the ash shedding mechanism is active only

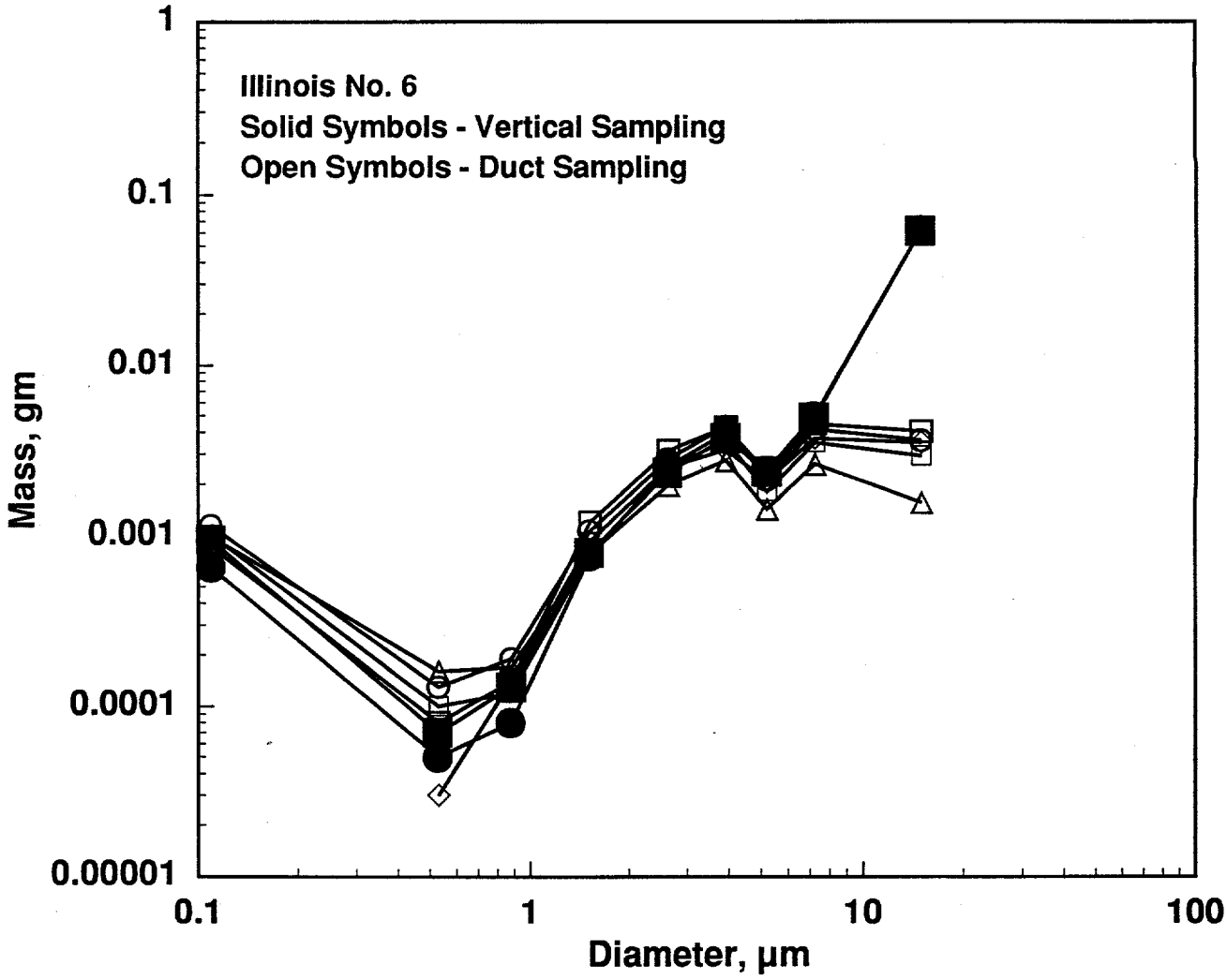

Figure 5-1. Influence of Sampling configuration on impactor stage yields.

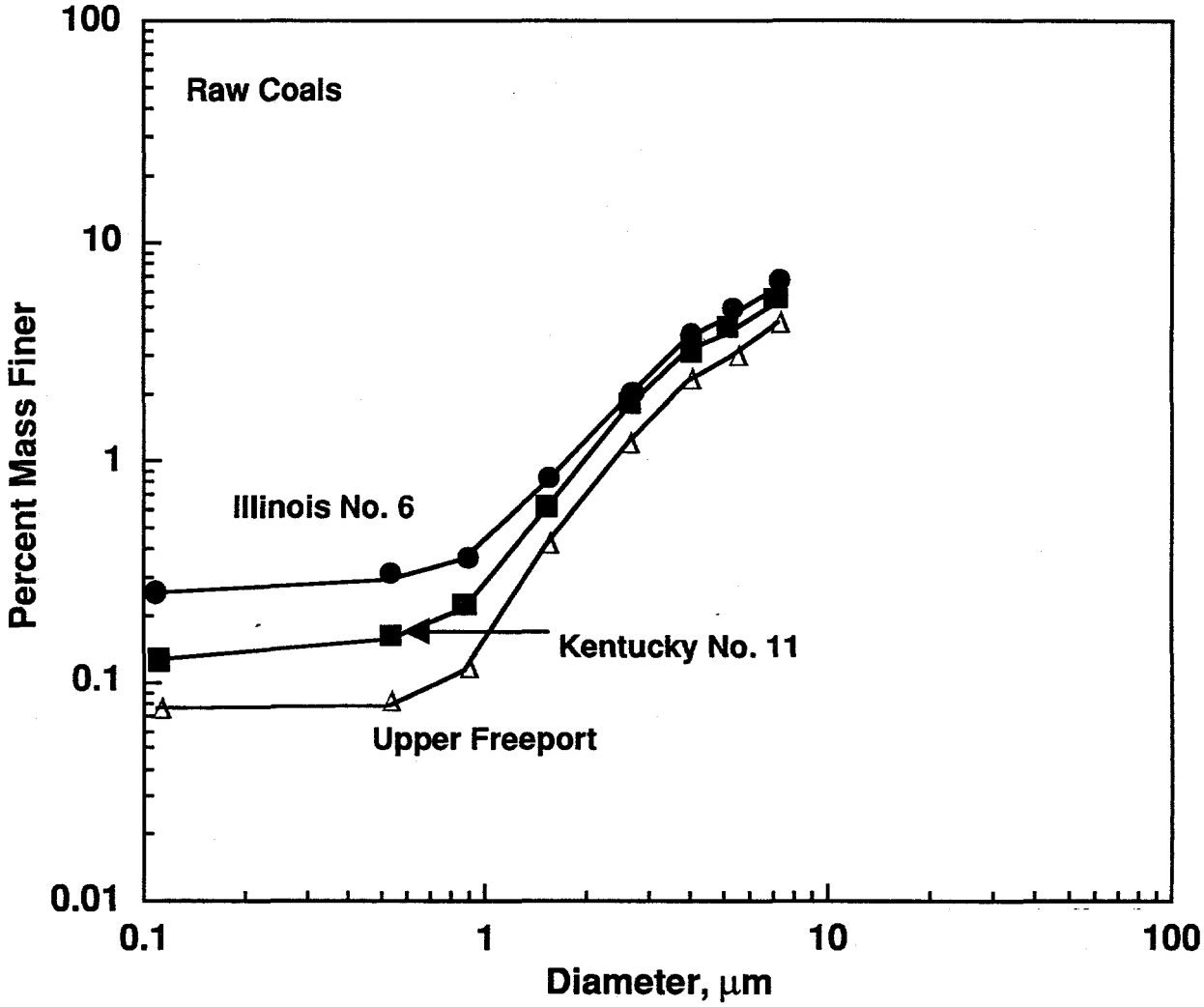

Figure 5-2. Cumulative size distribution data for three raw coals.

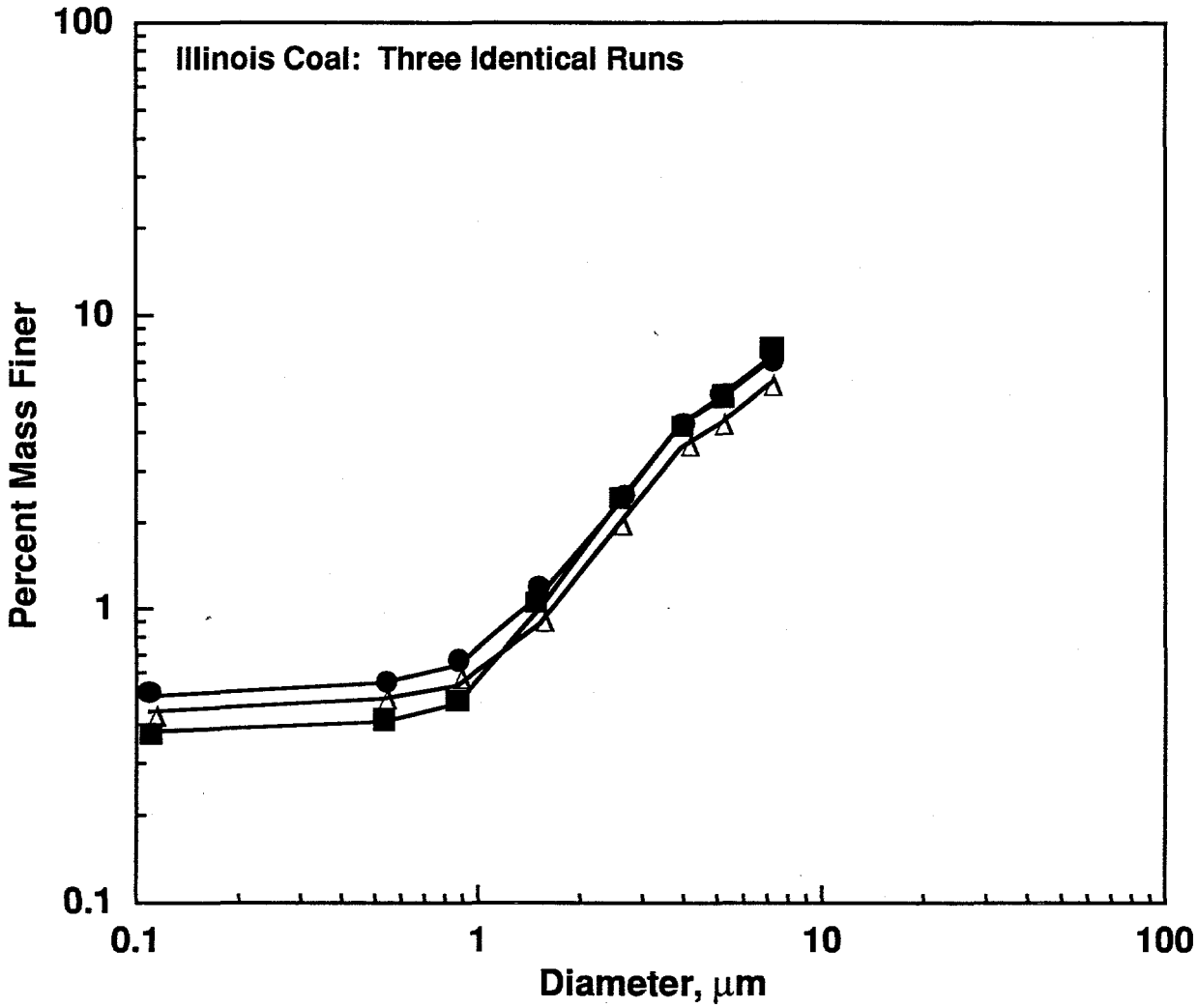

Figure 5-3. Repeatability size distribution test for the Illinois No. 6 coal.

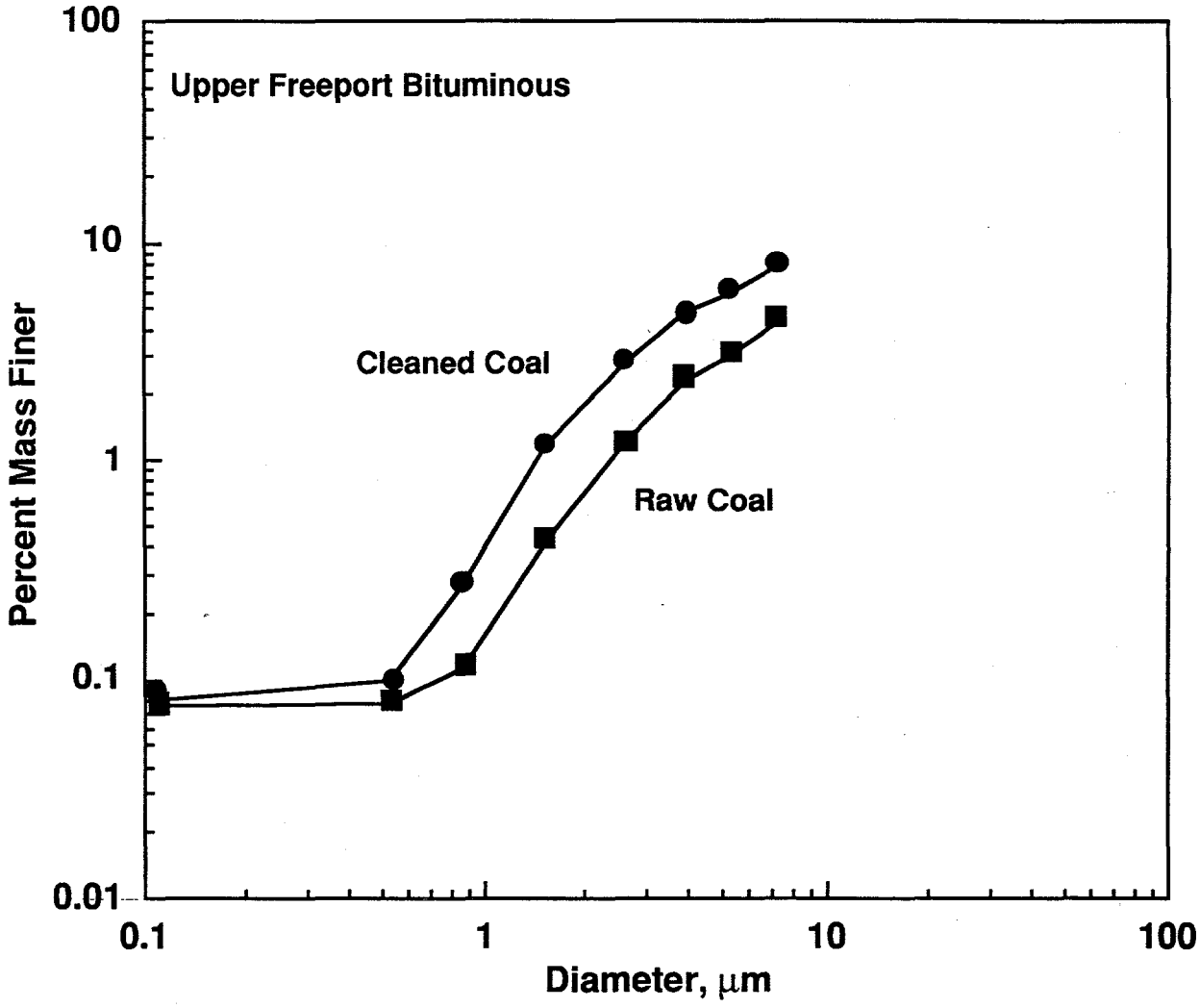

Figure 5-4. Influence of coal cleaning on aerosol yield and fine ash yield for the Upper Freeport coal.

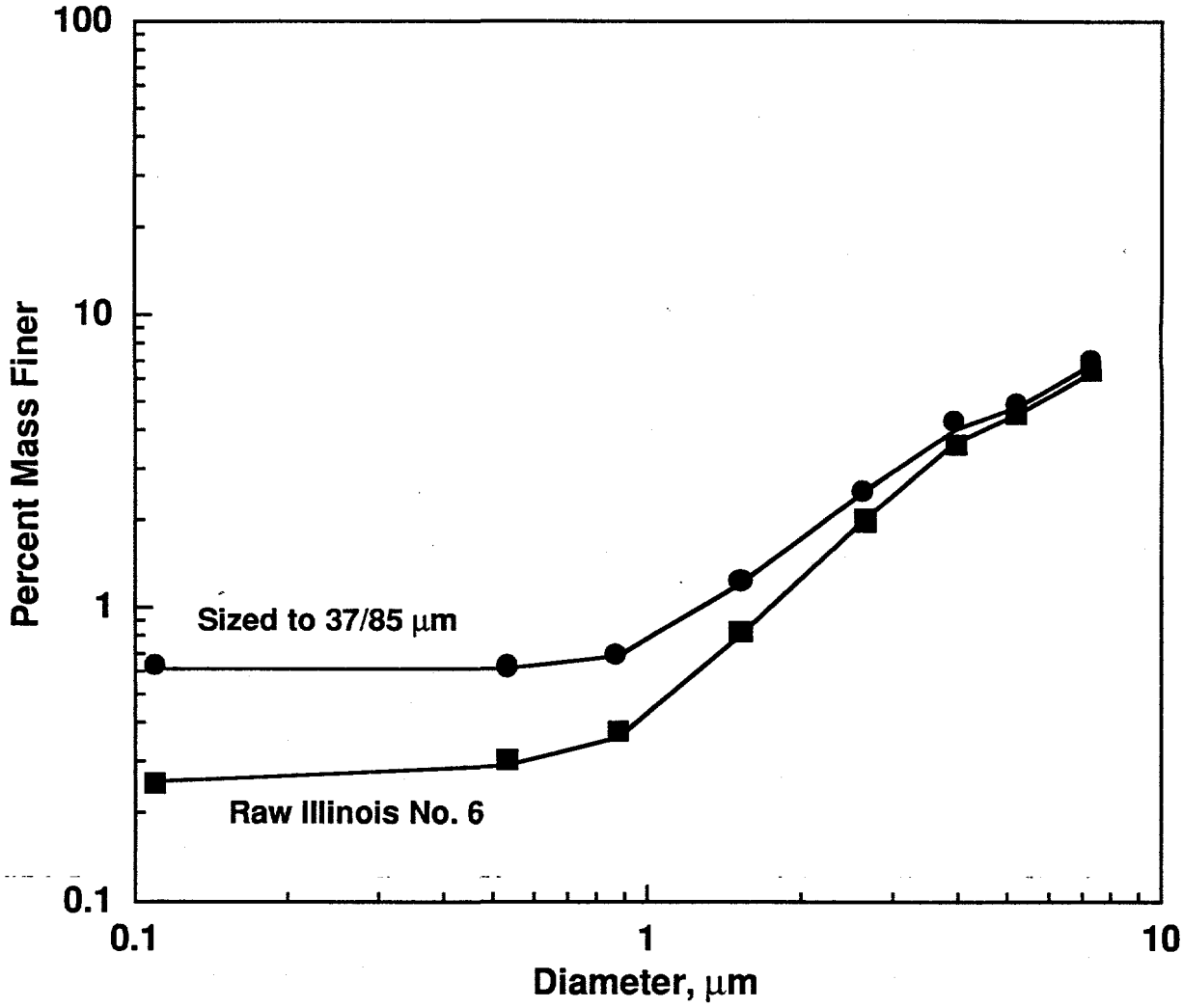

Figure 5-5. Influence of particle sizing on the ash size distribution for Illinois No. 6 coal.

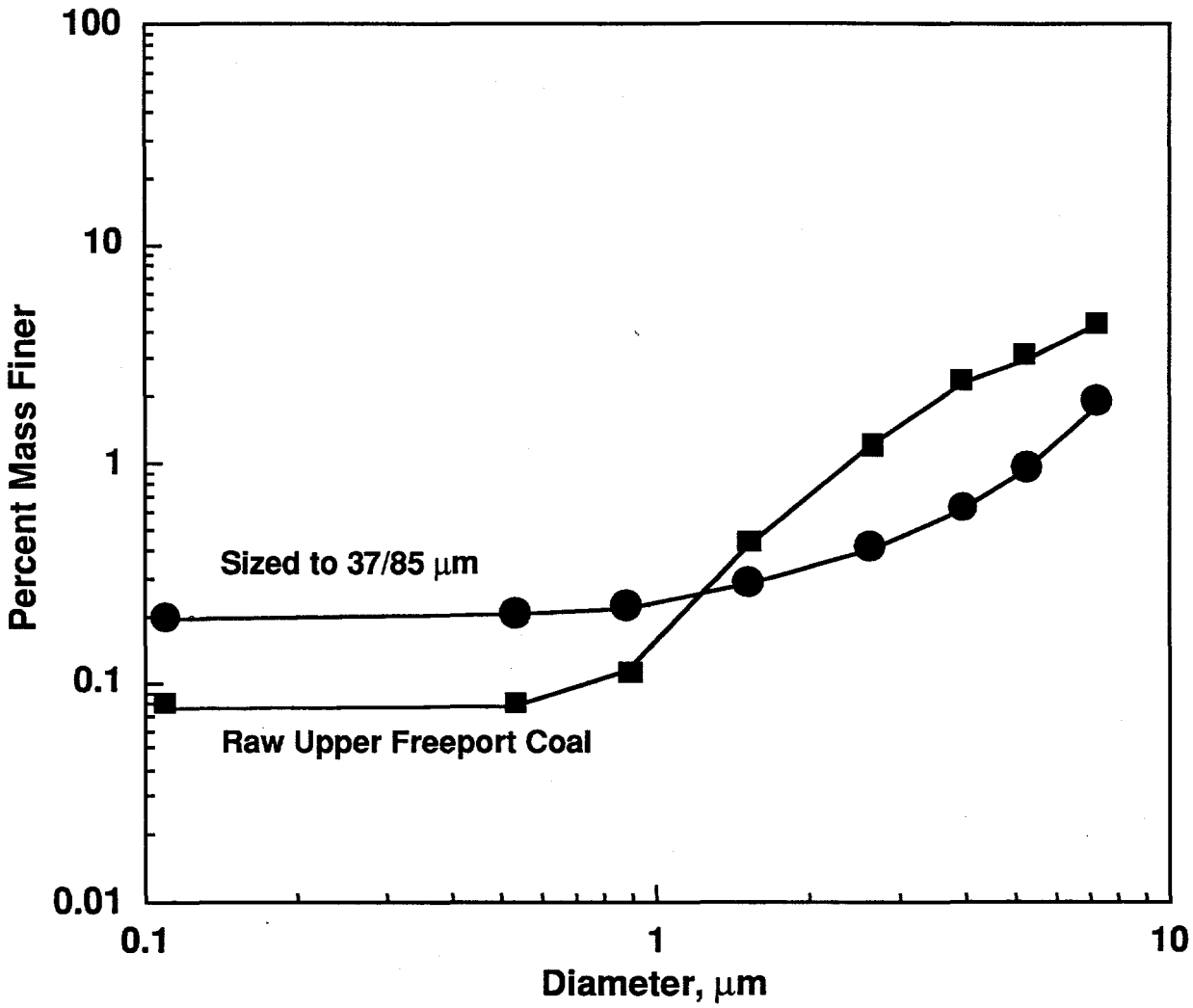

Figure 5-6. Influence of particle sizing on the ash size distribution for Upper Freeport coal.

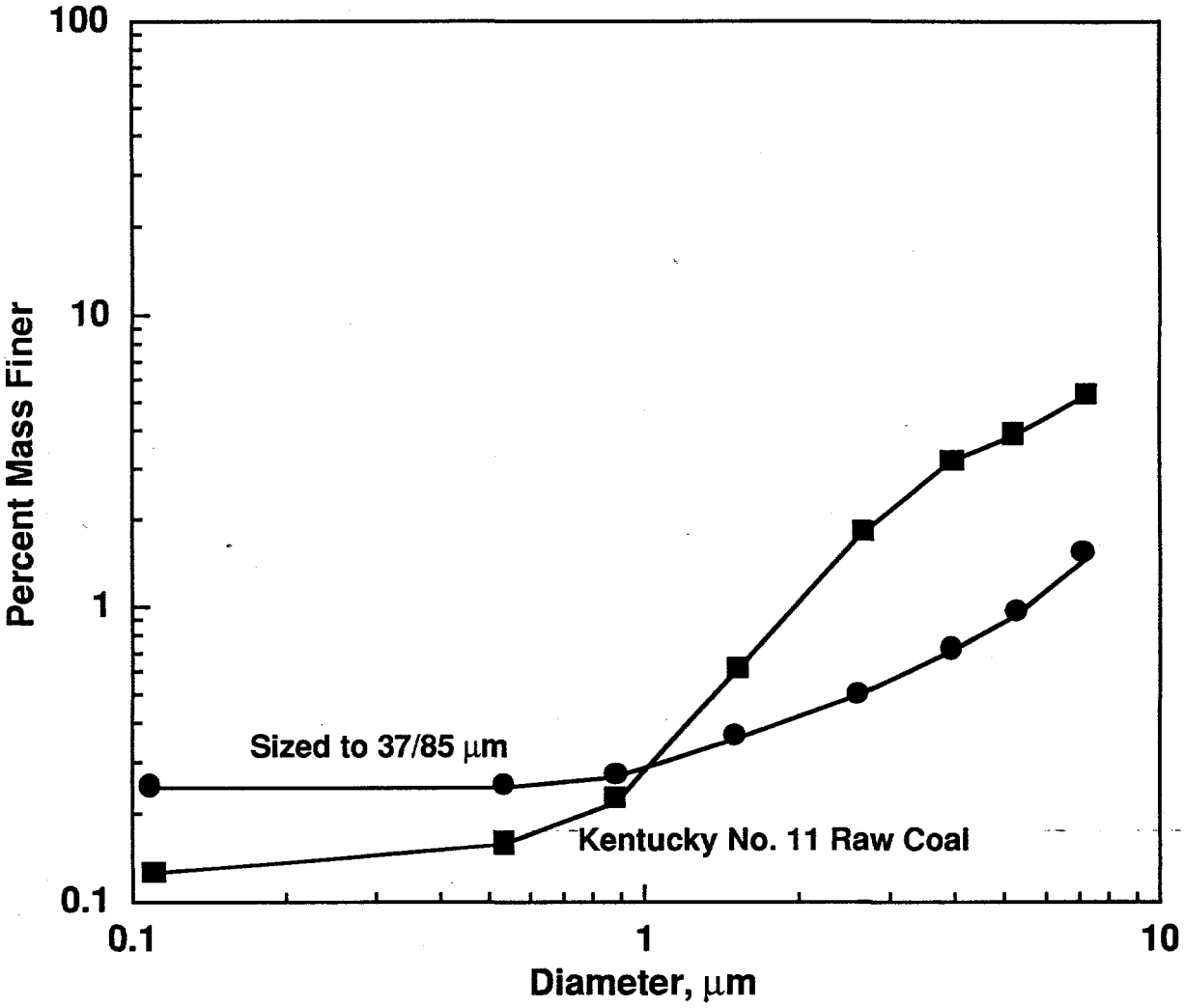

Figure 5-7. Influence of particle sizing on the ash size distribution for Kentucky No. 11 coal.

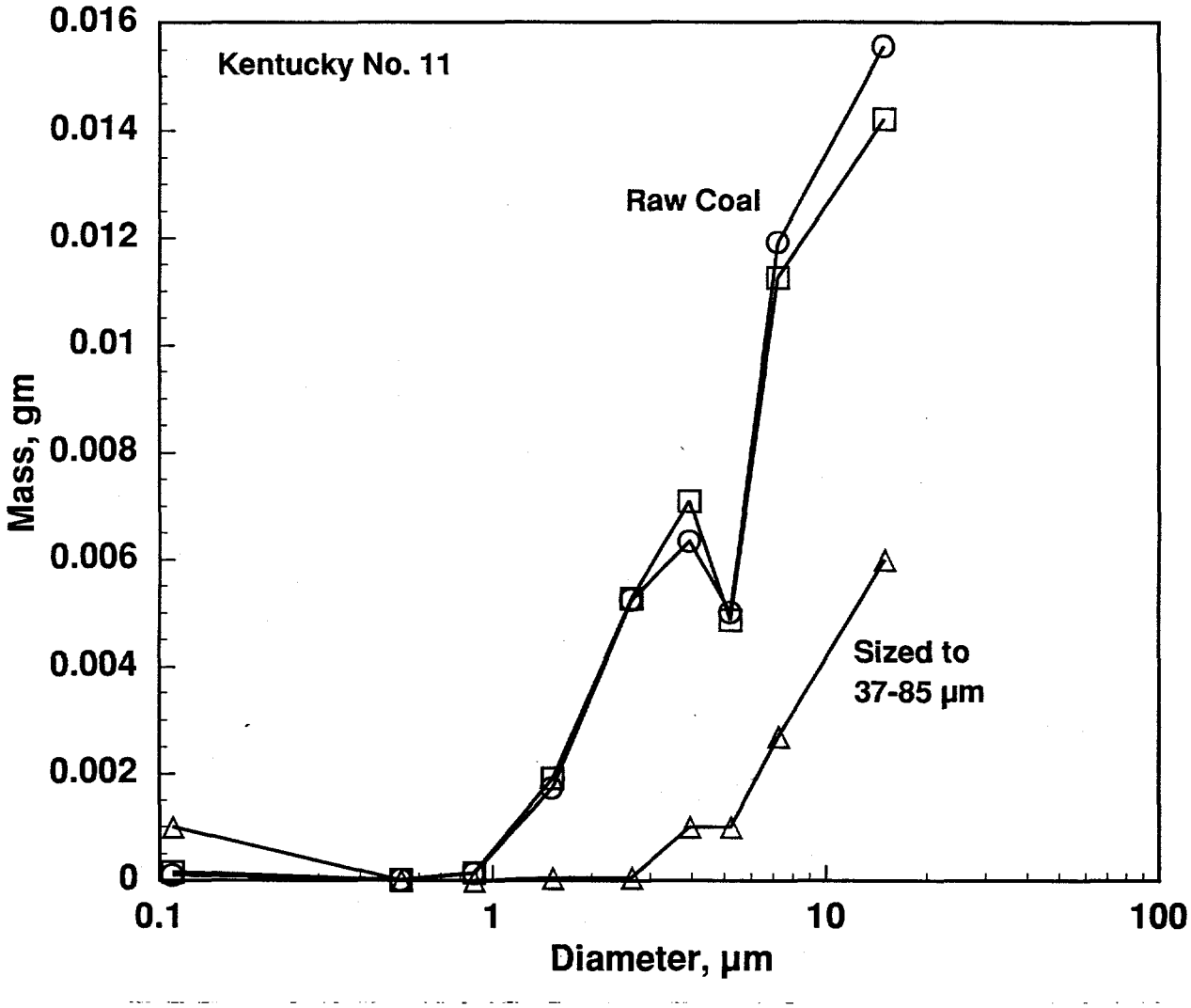

Figure 5-8. Comparison of sized Kentucky No. 11 fraction behavior with that of the original coal.

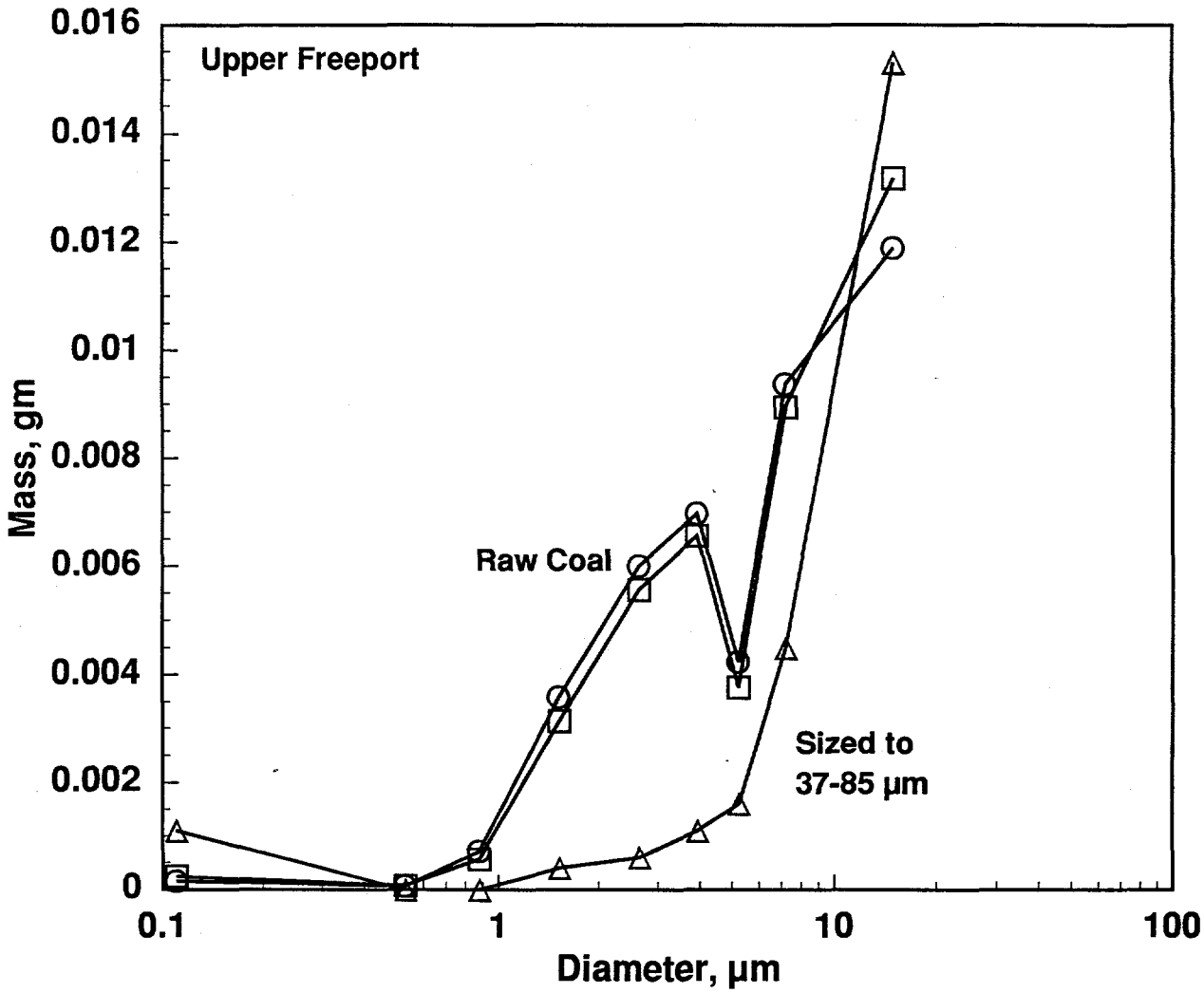

Figure 5-9. Comparison of raw coal behavior with that of one aerodynamically sized coal fraction.

during the initial stages of char combustion (Kramlich and Newton, 1994). It may be that the accumulation of minerals on the char surface as combustion progresses interferes with inclusion release. The present data support this mechanism for the Kentucky and Upper Freeport coals, but do not for the Illinois.

5.5 Furnace Temperature

A brief examination of the influence of furnace temperature on aerosol yields and residual ash size distributions was performed. The nominal temperature at the coal injection point was increased and decreased by about 75°C. Figure 5-10 shows that the residual ash size distribution was not influenced by the change in temperature, but that some variation in the aerosol yields (0.11 μm) was observed. The aerosol yields themselves are replotted in Figure 5-11 directly against injection temperature. These suggest a minimum in aerosol yields at the nominal injection temperature. Gallagher (1992) found that aerosol yields increased with increasing temperatures for bituminous coals. This was attributed to a decrease in char combustion time, leading to less time available for alkali capture by aluminosilicate inclusions. For bituminous coals, higher temperatures lead to less sodium retention by the aluminosilicates. Preliminary modeling suggests the following mechanism for the present data:

- At reduced temperatures the aerosol yield was primarily made up of alkali oxides.
- As the temperature is increased, the various mixed clay mineral inclusions within the coal pass their fusion temperatures, and become active at absorbing alkali vapors. The leads to a temporary reduction on aerosol yields as temperature is increased.
- Higher temperatures lead to an increase in total aerosol yields as other species become active in releasing vapors (*i.e.*, the reduction of refractory oxides to volatile elemental and suboxide forms, followed by their release and oxidation to aerosol).

Thus, there is a minimum in aerosol emissions associated with the beginning of active absorption of alkali vapors by included and excluded minerals. This may have been missed in Gallagher's work due to the range of temperatures selected.

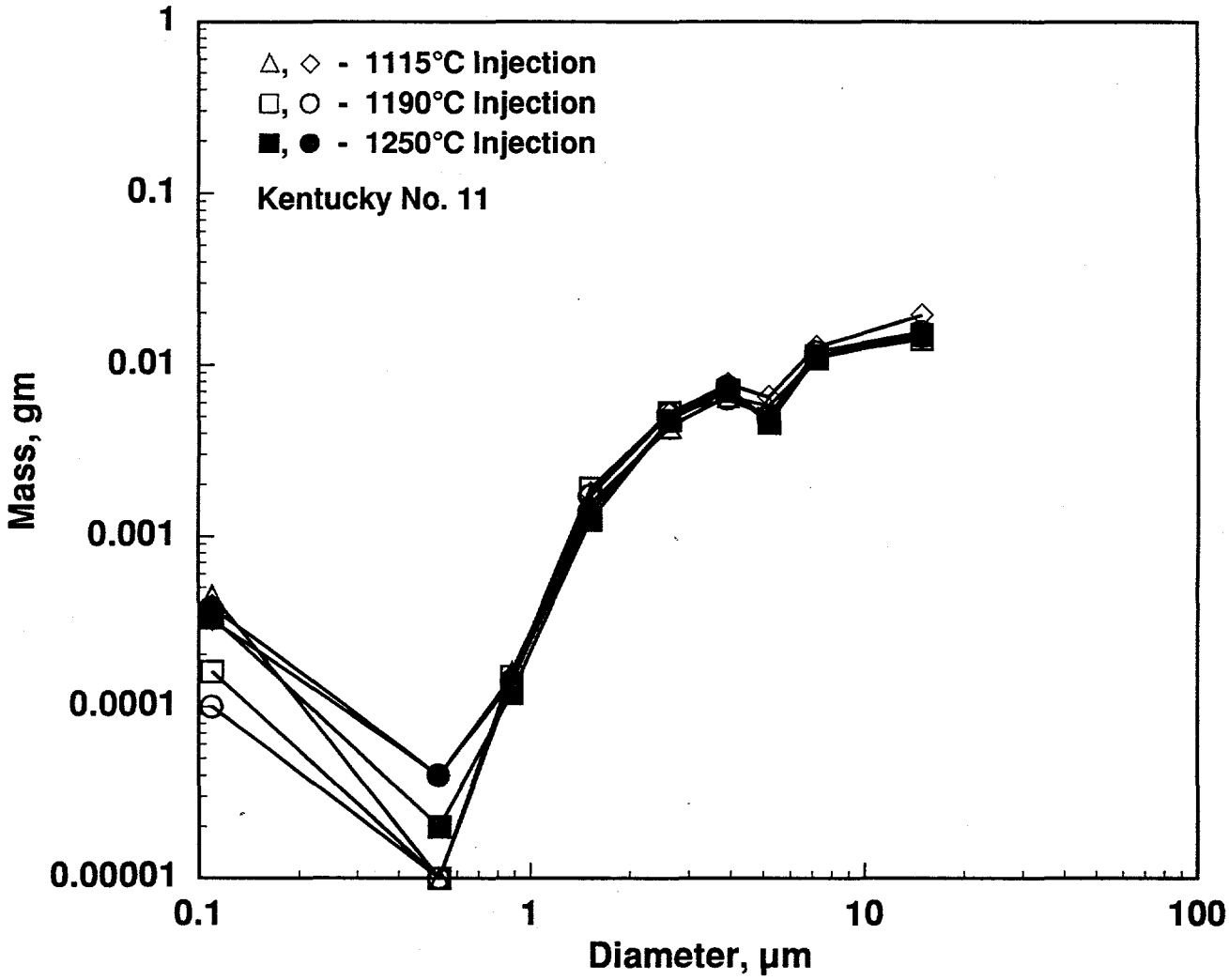

Figure 5-10. Influence of furnace temperature on impactor mass yields.

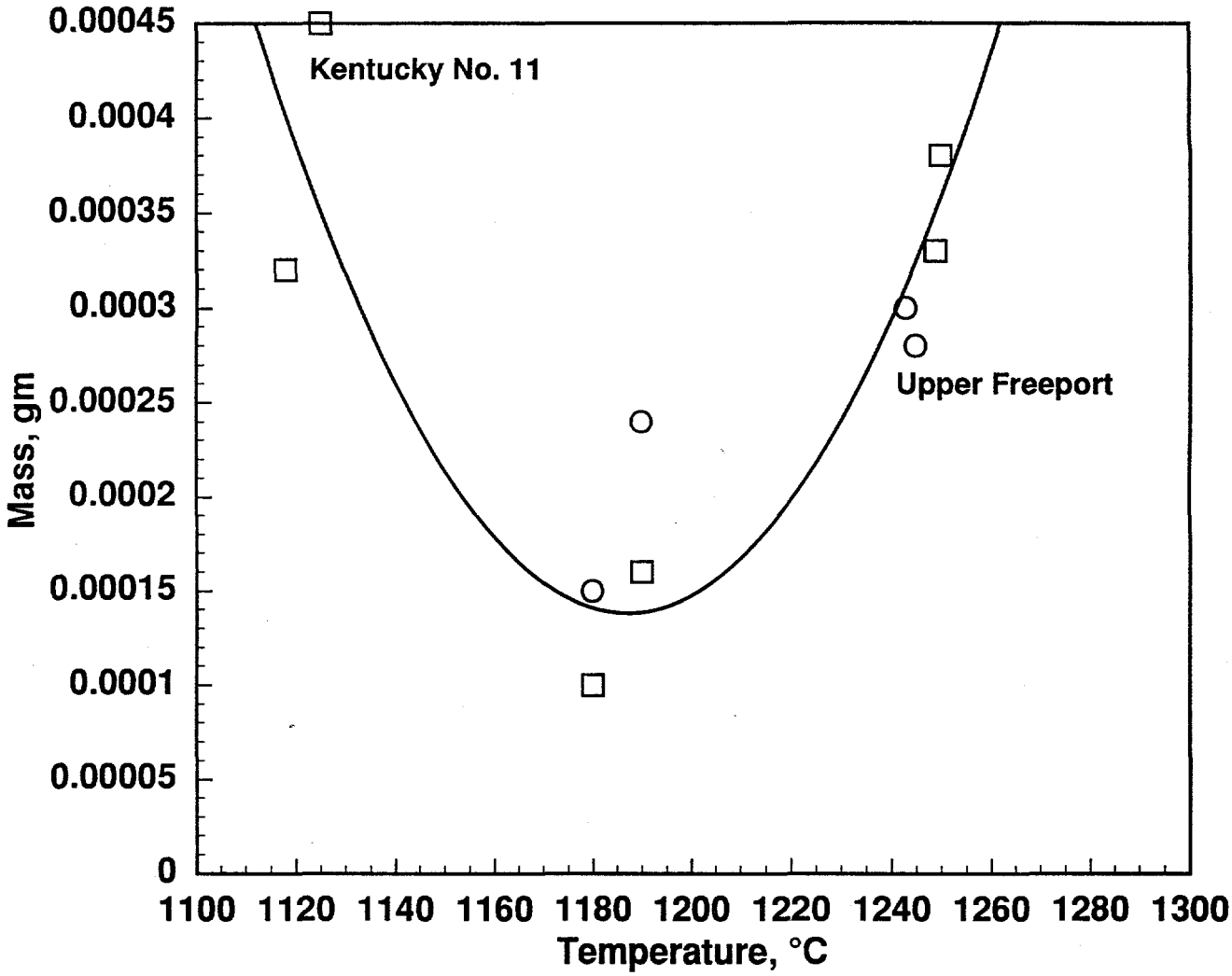

Figure 5-11. Influence of injection temperature on ash aerosol yield for two coals.

6.0 Artificial Char Results

6.1 Experimental Conditions

The temperature of the reactor when both secondary heating systems are turned on as well as the main burner, is about 1210°C at the top of the reactor, precisely at the sample port B, and 830°C at the bottom of the reactor, at the sample port K, as defined in Figure 6-1 (refer to Figure 3-3 to cross-reference sample port identifiers with the reactor cross-section). This profile remains almost a constant throughout the experiments. The complete profile of the reactor temperature is shown in Figure 6-2.

In addition to the temperature profile of the reactor, the conditions shown in Table 6-1 are held constant throughout the experiments. About 18 cc of artificial char is burned for each char in the combustion experiments, and the test duration is approximately 13 - 15 min. All combustion experiments are repeated except for the char with calcite as its mineral matter because the calcite showed very little influence on the capture of sodium vapor. The letters A and B are used to refer to the first and second replicates of each condition in the following tables and discussion. Particles that are larger than the nominal size of the first impactor stage are retained by the preseparator. These large particles are predominantly made up of unburned char. The data suggest a very high level of char burnout (of the order of 99%). Because of the large mass of carbon relative to the minerals in the starting char, the relatively high burnout still leaves the preseparator stage containing 30 - 40% of the collected mass. Most of the mineral mass is, however, associated with char that has fully burned out, and it appears on the regular impactor stages along with some unburned char.

6.2 Results

Tables 6-2 through 6-7 provide a full listing of the data that are presented in the following plots.

For the artificial chars #1 and #2, all the sodium in the char is expected to vaporize because there is no mineral matter to interfere with its release. As shown in Figure 6-3, the line representing the amount of ash captured by the cascade impactor is almost flat from impactor stage 0 through 7, while a relatively large amount of sodium is captured in the filter. The ash in the impactor stages 0 to 7 appears to consist primarily of unburned char, along with a contribution of residual sodium that did not vaporize.

The results shown in Figure 6-3 suggest complex behavior. First, the variability between the repeats is greater than desired. Since earlier data on the coals showed significantly better repeatability, the suggestion is that the source of the variability lies in the artificial chars themselves. Potential issues include variability on sodium content for the chars, and variability in char size distributions. In either case, good characterization is critical.

Figure 6-3 also shows the comparison between the amount of sodium that would be expected in the impactor filter versus the amount of sodium collected. The amount of sodium expected is calculated with assumptions that the impactor sample probe collected about 5.6% of particles and the sodium collected is in the form of sodium carbonate (Na_2CO_3). As Figure 6-3 indicates, the amount of sodium collected is somewhat less than the amount of sodium expected. This suggests that the small amount of residual sodium that did not vaporize appears on impactor stages 0 to 7.

The data indicate that the low-porosity chars (Char #2) tend to have a higher pre-separator yield, a slightly higher yield in the midrange of the impactor, and a higher aerosol yield. The higher pre-separator yield likely indicates poorer burnout, since for sodium injection little pure mineral matter is expected within the size range collected by the pre-separator. This is not unexpected since the low porosity char will be less reactive. Also, earlier testing indicated burnout problems for the

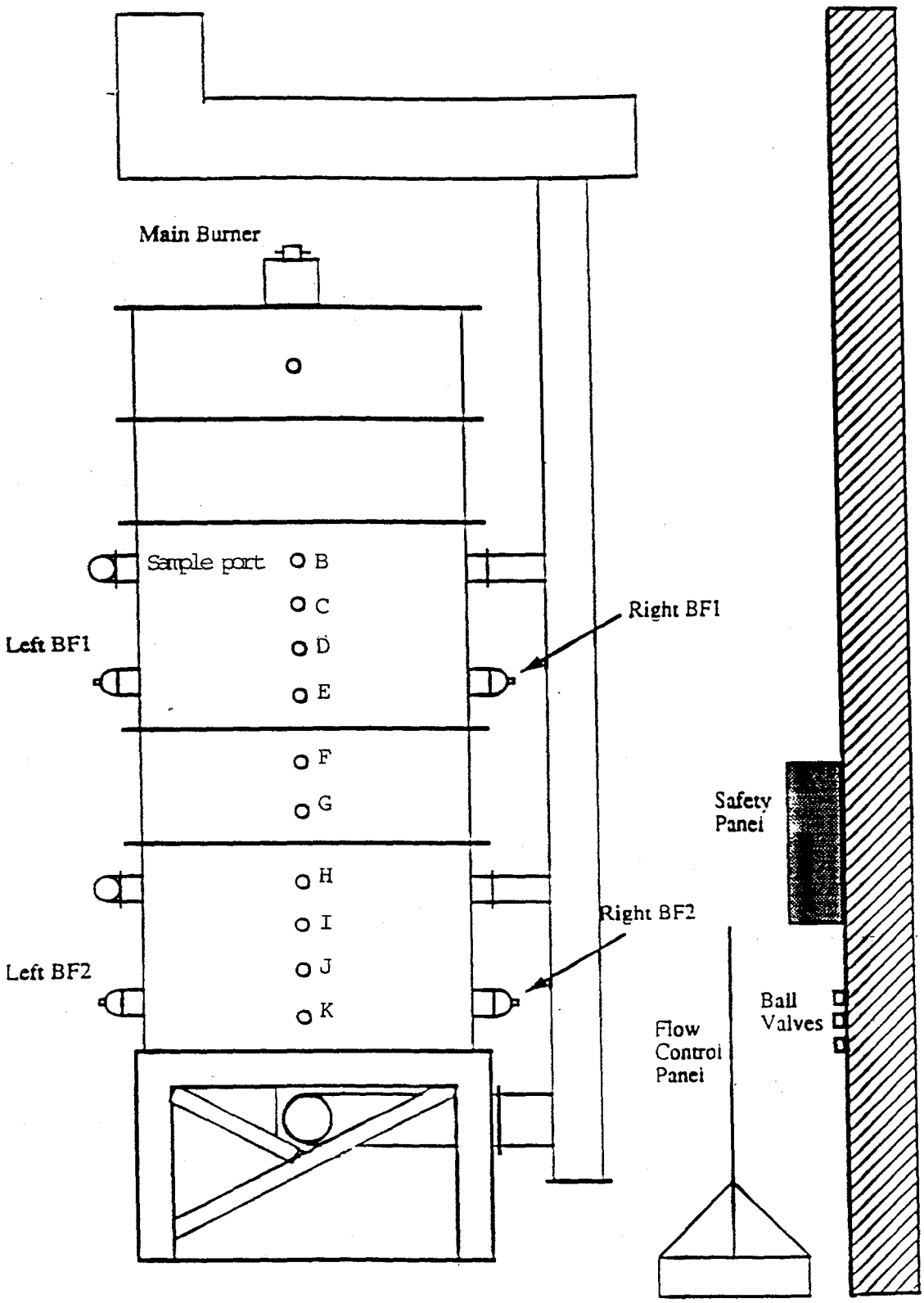

Figure 6-1. Schematic of the reactor, showing ports used for the artificial char experiments.

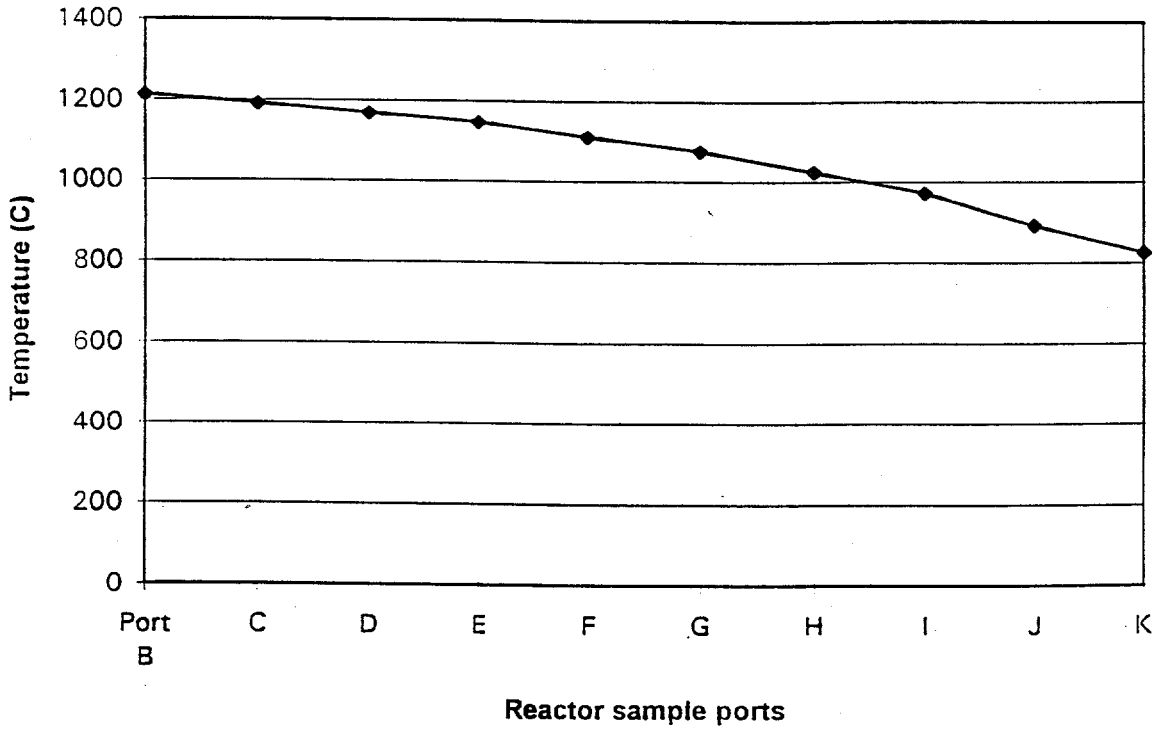

Figure 6-2. Furnace temperature profile used for the artificial char experiments.

Table 6-1
Experimental Conditions used for the Artificial Char Experiments

Reactor Information	
Main Natural Gas Flow (%)	82 - 83
Main Air Flow (%)	47 - 48
Main Air Pressure (psig)	33 - 33.5
Back Fire Burner 1	
Natural Gas Flow (%)	44
Air Flow Left (SCFM)	3.7 - 3.8
Air Flow Right (SCFM)	3.7 - 3.8
Back Fire Burner 2	
Natural Gas Flow (%)	20
Air Flow Left (SCFM)	2.6 - 2.8
Air Flow Right (SCFM)	2.6 - 2.8
Injector Information	
Feed Rate(Machine Setting)	5-90
Rotometer Flow (%)	20
Rotometer Pressure (psig)	44
Temperature Information (^{o}F)	
Duct	100 - 112
Over the Reactor	95 - 131
Probe Coolant	140 - 150
Other Information	
Atom. Air Flow (units)	Full
Atom. Air Pressure (psig)	Full
Atom. H_2O (mm)	180
Vac. Rotometer Flow (%)	72
Vac. Rotometer Pressure (inHg)	9.5 - 9.6
Probe Coolant Flow (mm)	145
Purge Flow Pressure (psig)	7

Table 6-2. Mass of ash in char #1 and char #2 (in gram)

	Char #1A	Char #2A	Char #1B	Char #2B
Presep	0.00095	0.00179	0.00169	0.00316
0	0.00037	0.00039	0.00029	0.00084
1	0.00014	0.00034	0.00016	0.00075
2	0.00016	0.00027	0.00012	0.00067
3	0.00016	0.00032	0.00015	0.0008
4	0.00025	0.00035	0.00018	0.00069
5	0.00021	0.00027	0.00017	0.00041
6	0.00012	0.00017	7E-05	0.00016
7	7E-05	0.00011	1E-05	8E-05
Filter	0.00125	0.00187	0.00098	0.00151

Table 6-3. Mass of ash in pyrite A series (in gram)

	Char #3	Char #4A	Char #5A	Char #6A	Char #7A
Presep	0.00095	0.00103	0.0016	0.00405	0.00463
0	0.00037	0.00029	0.00038	0.00115	0.00081
1	0.00014	0.0003	0.00038	0.00089	0.00089
2	0.00016	0.00024	0.00033	0.00078	0.00069
3	0.00016	0.00046	0.00049	0.00109	0.00109
4	0.00025	0.0005	0.00058	0.0011	0.00111
5	0.00021	0.00037	0.00031	0.00062	0.00079
6	0.00012	0.00014	9E-05	0.00022	0.00017
7	7E-05	8E-05	4E-05	8E-05	9E-05
Filter	0.00125	0.00109	0.00086	0.0012	0.00155

Table 6-4. Mass of ash in pyrite B series (in gram)

	Char #3	Char #4B	Char #5B	Char #6B	Char #7B
Presep	0.00169	0.00236	0.00398	0.00649	0.00263
0	0.00029	0.00054	0.00056	0.00192	0.00072
1	0.00016	0.00042	0.00049	0.00123	0.00073
2	0.00012	0.00038	0.00045	0.001	0.0004
3	0.00015	0.00044	0.00064	0.0015	0.00086
4	0.00018	0.00047	0.00062	0.00136	0.00091
5	0.00017	0.00035	0.00039	0.00079	0.00056
6	7E-05	0.00012	0.00013	0.00023	0.00018
7	1E-05	0.00013	2E-05	0.00012	1E-04
Filter	0.00098	0.00111	0.00109	0.0015	0.00117

Table 6-5. Mass of ash in bentonite A series (in gram)

	Char #8	Char #9A	Char #10A	Char #11A	Char #12A
Presep	0.00095	0.004849	0.00353	0.00484	0.00683
0	0.00037	0.00144	0.0009	0.00119	0.0021
1	0.00014	0.001012	0.00097	0.00109	0.00139
2	0.00016	0.001035	0.00076	0.00106	0.00114
3	0.00016	0.001226	0.00132	0.00178	0.00154
4	0.00025	0.00117	0.00126	0.00179	0.00134
5	0.00021	0.000641	0.00071	0.00077	0.00078
6	0.00012	0.000281	0.00022	0.00024	0.00031
7	7E-05	0.000124	9E-05	0.0001	0.0002
Filter	0.00125	0.001552	0.00096	0.00047	0.00079

Table 6-6. Mass of ash in bentonite B series (in gram)

	Char #8	Char #9B	Char #10B	Char #11B	Char #12B
Presep	0.00169	0.00216	0.00268	0.00768	0.00874
0	0.00029	0.0005	0.00079	0.00157	0.00231
1	0.00016	0.00046	0.00079	0.00126	0.00178
2	0.00012	0.00039	0.00063	0.00133	0.00136
3	0.00015	0.00065	0.00112	0.00203	0.00188
4	0.00018	0.00073	0.00107	0.00183	0.00152
5	0.00017	0.00037	0.00056	0.00085	0.00076
6	7E-05	0.00013	0.00018	0.00027	0.00018
7	1E-05	7E-05	5E-05	0.00011	1E-04
Filter	0.00098	0.00106	0.00061	0.00039	0.0007

Table 6-7. Mass of ash in calcite series (in gram)

	Char #13	Char #14	Char #15	Char #16	Char #17
Presep	0.00095	0.00361	0.00162	0.00194	0.00235
0	0.00037	0.00043	0.00028	0.00045	0.0005
1	0.00014	0.00025	0.00015	0.0002	0.00037
2	0.00016	0.0002	0.00015	0.00022	0.00022
3	0.00016	0.00012	0.00011	0.00019	0.0002
4	0.00025	0.00019	0.00023	0.00019	0.00033
5	0.00021	0.00017	0.00022	0.00025	0.00023
6	0.00012	7E-05	6E-05	5E-05	6E-05
7	7E-05	7E-05	9E-05	5E-05	1E-05
Filter	0.00125	0.00098	0.00114	0.00106	0.001

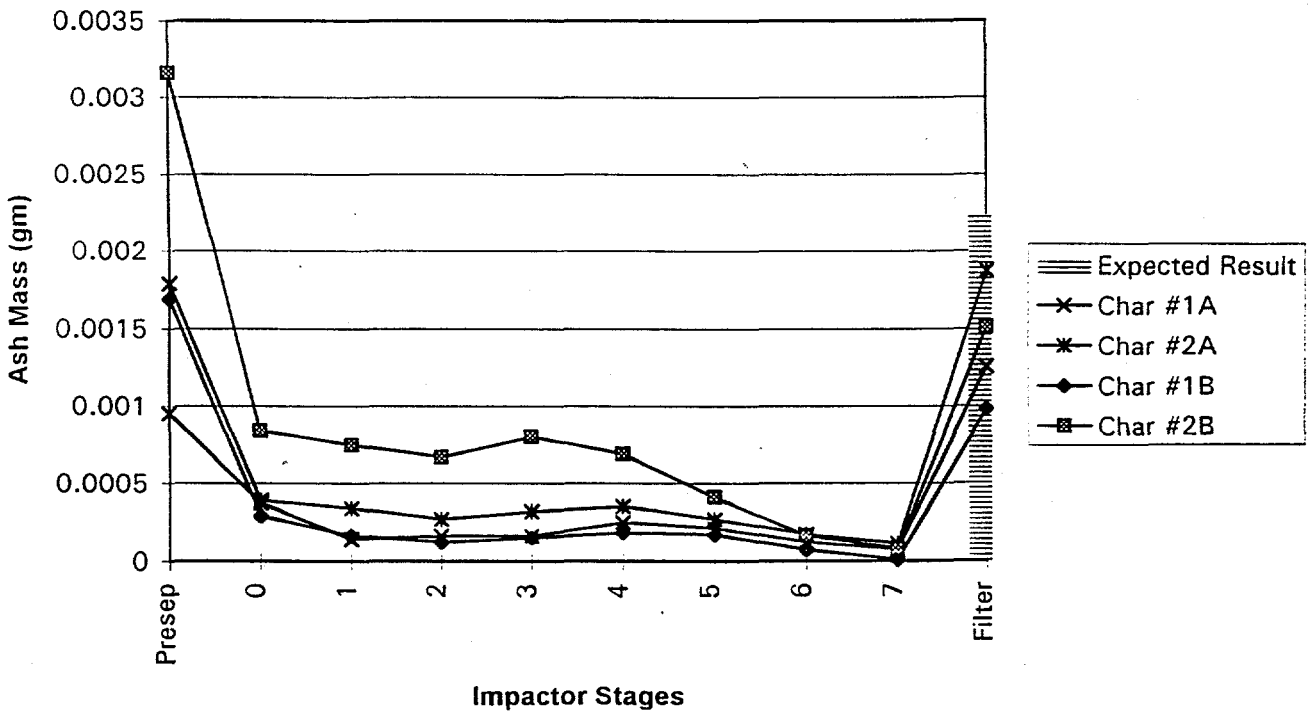

Figure 6-3. Ash yields for chars #1 and #2.

artificial chars. This led to the increase in furnace temperature for the final data sets.

The reason for the increased aerosol yields for the less reactive char is not clear. One speculative suggestion is that a fraction of the sodium is not vaporizing, and thus these experiments represent a competition between sodium vaporization and the formation of residual sodium particles. In the low-porosity char, the longer burning time may provide additional opportunity for sodium to vaporize.

Figure 6-4 shows the results from the pyrite series A and Figure 6-5 is for pyrite series B. For both figures, the data from char #1 is included to compare the influence of pyrites on the sodium vaporization.

For the pre-separator and the impactor stages, the general trend of Figures 6-4 and 6-5 is that increased amounts of pyrite lead to increased residual ash formation. This is not unexpected since pyrite has a relatively high melting point (1171°C), and thus would not be expected to have enough volatility to undergo significant vaporization. Thus, most of the pyrite would be expected to be found in the pre-separator and on the impactor stages rather than on the backup filter.

Note in Figure 6-4 that the loading on the preseparator and on the impactor stages correlates with the amount of pyrite added to the char. The same correlation carries through to Figure 6-5 with the exception of char #7B, which shows much less ash generation than is expected based on the other chars. Interestingly, the added mass appears as a proportional increase in all the stages (except the filter stage), rather than only in the preseparator. Given the relatively large size of the raw pyrite particles (9 - 10 μm), it would not be unexpected for all the additional mass to be found on the preseparator and on stage zero. Pyrite is, however, well known to fragment during char combustion, and the degree of fragmentation and mechanism continue to be of research interest elsewhere.

In spite of this clear increase in mineral content, the yield of aerosol on the backup filter does not correlate well with the amount of added minerals. Figure 6-6 shows a plot of mass recovered at the filter stage against the amount of pyrite added to the chars. This can be taken as an indication of aerosol yield. The results do not suggest any consistent change in sodium vaporization as the pyrite loading on the char is increased. In retrospect, the relatively large size of the pyrite particles (9 - 10 μm) may be responsible. The reduced surface/volume ratio of these particles compared with the native pyrite found in coal (1 - 2 μm) would be expected to diminish any sodium capture, even if such a mechanism were active.

There are some indications in very recent data obtained elsewhere that pyrite will itself undergo vaporization during char combustion. This is unexpected due to the low volatility of pyrite and other related iron compounds. There is speculation that the vaporization is due to the presence of a reactive intermediate that occurs during pyrite oxidation. With the large particles used in this study, no evidence of pyrite vaporization was seen.

Figure 6-7 shows the results from bentonite series A and Figure 6-8 shows the same data for bentonite series B. The data from char #1 are included to compare the influence of bentonite on the sodium vaporization. For both Figure 6-7 and Figure 6-8, the results shown in the impactor stage 0 through 7 show the similar trends as in pyrite series. Thus, it is assumed that the particles captured in the stage 0 through 7 are primarily residual bentonite particles and a small amount of residual sodium that did not vaporize.

It is interesting to note that although the raw bentonite particles were much smaller than the raw pyrite particles, the size distribution of the residual ash for the two were similar. The added bentonite appears as both an increase in the preseparator stage and in each of the aerodynamic impactor stages. This suggests that the pyrite was strongly fragmented during char combustion,

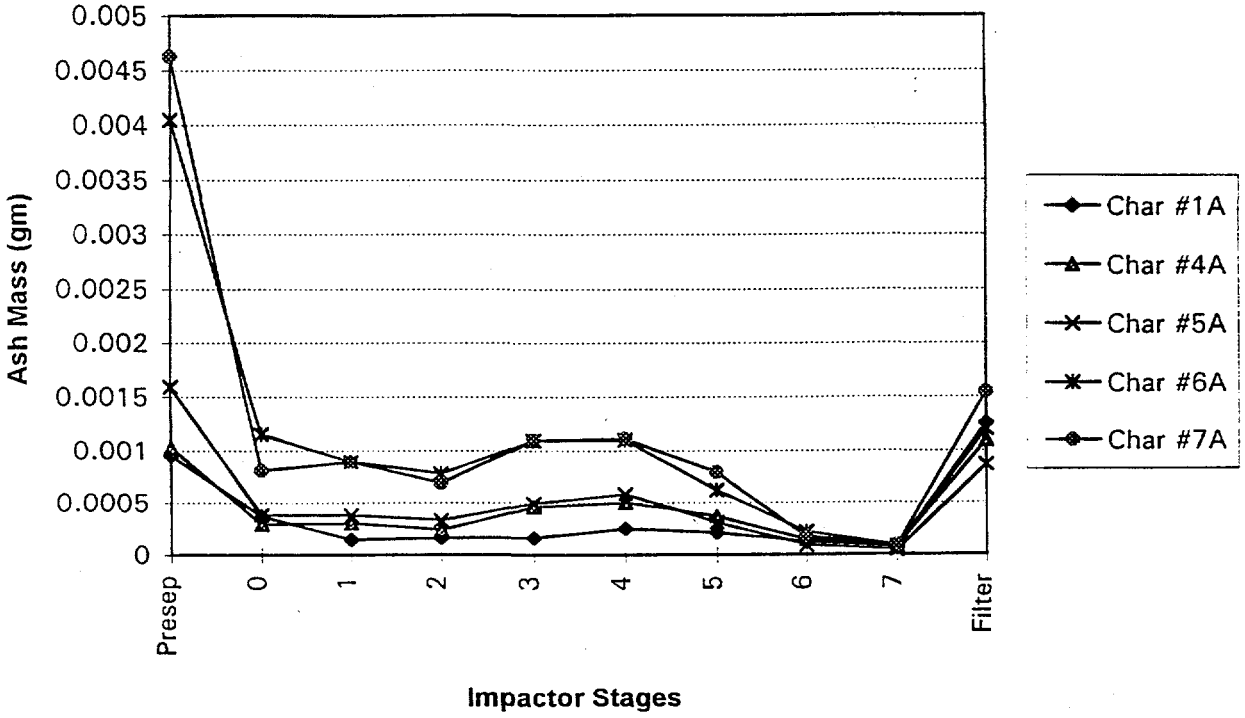

Figure 6-4. Char #1A and pyrite A series (char #4 - char #7)

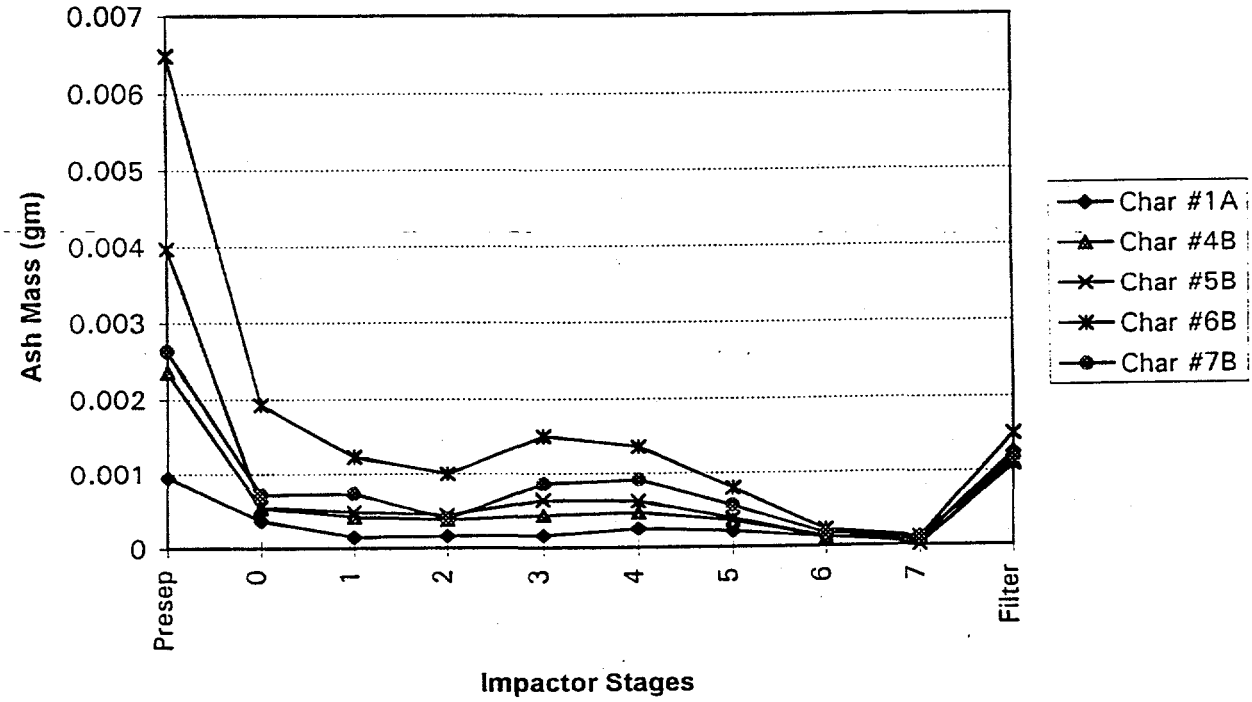

Figure 6-5. Char #1A and pyrite B series (char #4 - char #7)

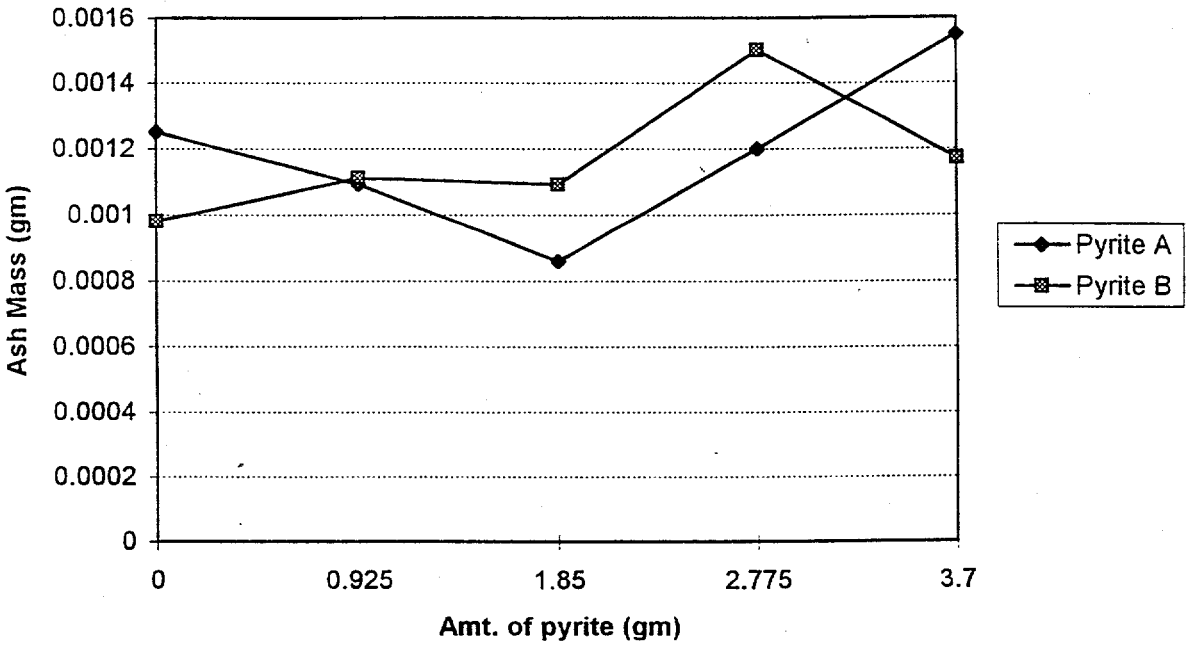

Figure 6-6. Summary of aerosol yields for the pyrite series.

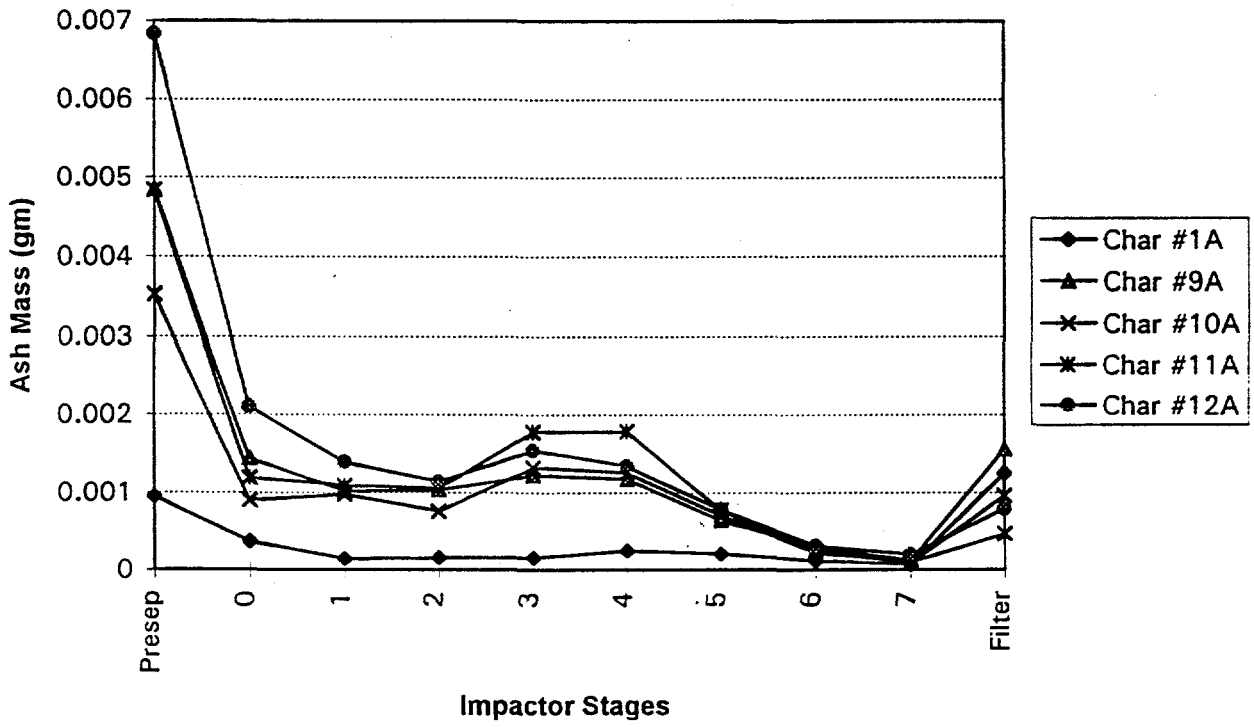

Figure 6-7. Char #1A and bentonite series A (chars #9 - #12).

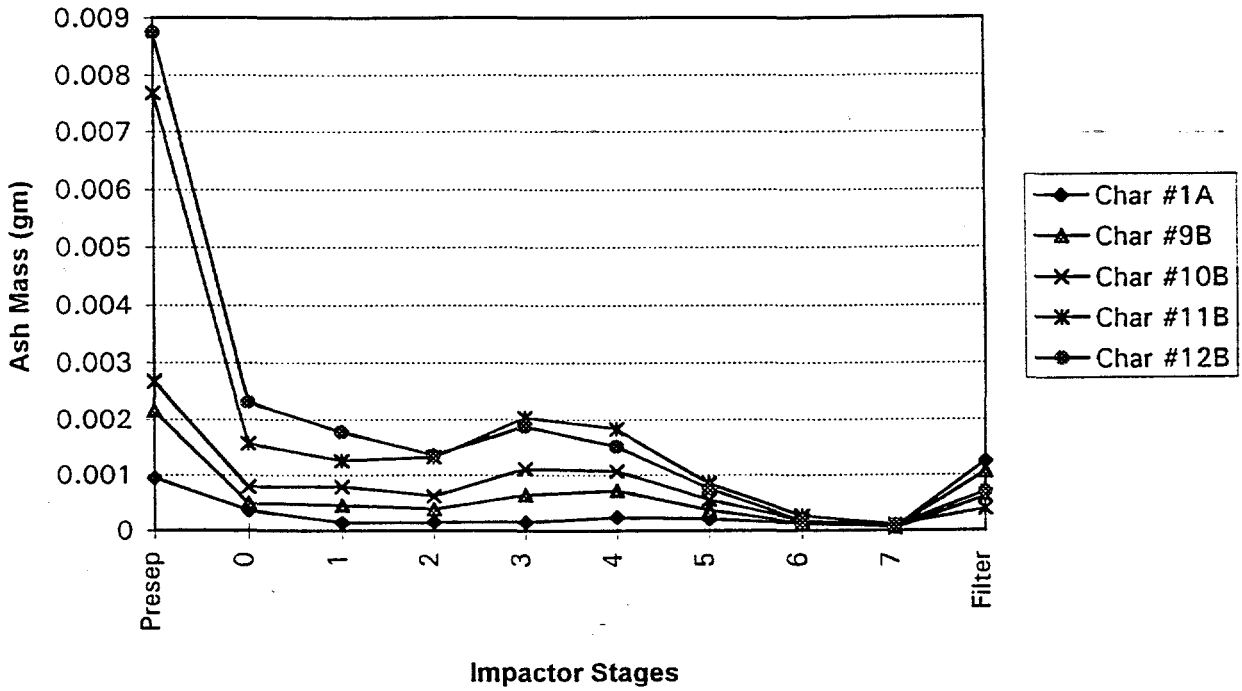

Figure 6-8. Char #1A and bentonite series B (chars #9 - #12).

something that has been suggested elsewhere.

Figure 6-9 is a plot of the filter yield (aerosol fraction) as a function of the amount of bentonite in the chars. In each case, the general trend is for reduced aerosol yields as the amount of bentonite increases. It is interesting that in each case the lowest bentonite doping gave an increased aerosol yield over the straight sodium char.

Figures 6-10 and 6-11 show the results from calcite series. As shown in Figure 6-10, the addition of the calcite to the artificial char had little effect on the loading on any of the impactor stages, with the exception of the preseparator. This indicates that the relatively large calcite particle (15 - 17 μm) did not fragment during char burnout. This is in contrast with the pyrite particles, which were of nominally a similar size but which yielded a much finer size distribution.

Figure 6-11 shows that the addition of the calcite had essentially no effect on the aerosol yield. This result was likely due to the large size of the particles used. As with the pyrite, the low surface to volume ratio would reduce the effectiveness of the additive for the capture of the sodium. In addition, calcite undergoes calcination to CaO at about 900°C, and the melting point of CaO is 2580°C. This suggests that the crystalline form of CaO would not exhibit much mobility at normal char combustion temperatures. Thus, it is likely that CaO would not effectively complex sodium, even if an increased surface area were made available.

6.3 Discussion

Artificial char provides one means of understanding the interactions of minerals in coal combustion. For the present studies, the artificial char is used to provide data on the suppression of sodium vaporization via the capture of the sodium vapor by mineral inclusions. Three minerals, pyrite, bentonite, and calcite, are incorporated into a char matrix that also contains atomically dispersed sodium. The results suggest that suppression of sodium vaporization does occur, but that it is a complex process governed by the type of mineral and the mineral size distribution.

For chars #1 and #2 (containing only sodium as a mineral), all the sodium is expected to vaporize, and appear as mass on the filter stage of the impactor. For this case, that ash yields on stages 0 through 7 are very low, meaning that most of the sodium is vaporized. Also, the aerosol mass on the filter stage is high, meaning that vaporized sodium is captured in the filter. The mass of large particles appearing in the preseparator appear to be associated with unburned char, although char burnouts of greater than 99% are indicated. However, the variability between series A and B is larger than expected based on earlier coal results, and the amount of ash at the filter is less than the expected mass of ash.

The results of combustion experiments for the pyrite series of artificial chars generally agree with the expected result. Because of the high melting point of the pyrites and a very short residence time, the pyrites are not believed to be vaporized, and are captured in the pre-separator and the impactor stages. As a result, ash yields on impactor stages 0 through 7 are higher than that for char #1. Since the original pyrite particles are so large, the appearance of additional mass on stages 0 through 7 indicates substantial pyrite fragmentation. On the filter stage, most of the pyrite series chars yield less aerosol than char #1. This indicates some sodium capture, although the level of capture is not large.

In the combustion experiments for the bentonite series, the results are similar to those of the pyrite series. Again, the ash collected in the pre-separator and the impactor stages are believed to be bentonite particles and a small amount of sodium that did not vaporize. Here, a significant aerosol reduction occurred as the loading of bentonite increased. Since the particle size for bentonite is small, it is believed that those bentonite particles present a sufficiently large surface area to be effective for sodium capture.

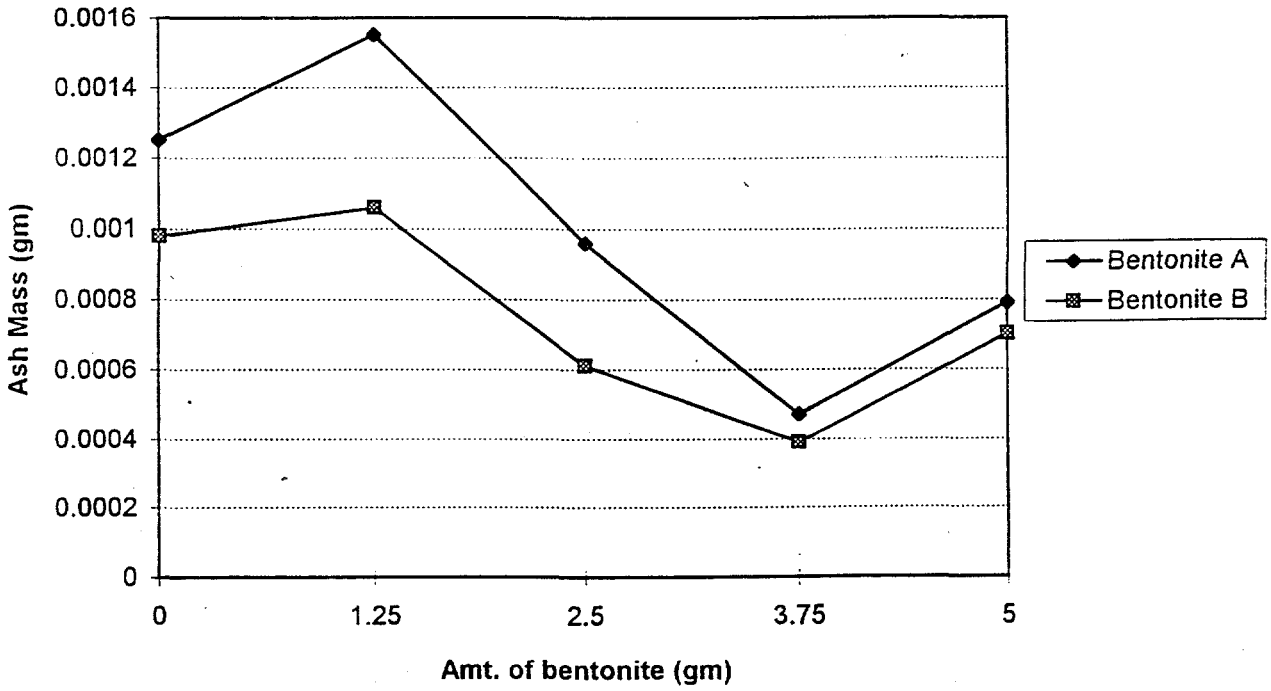

Figure 6-9. Summary of aerosol yields for the bentonite series.

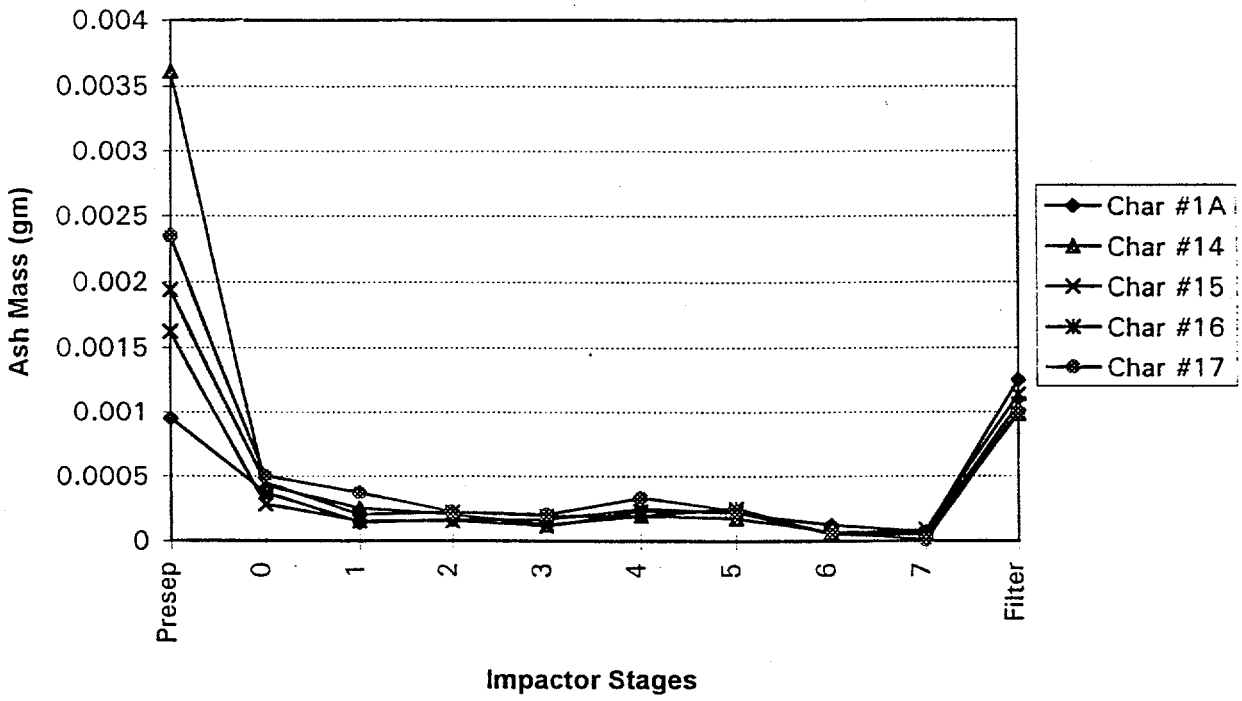

Figure 6-10 Char #1A and calcite series (char #14 - char #17)

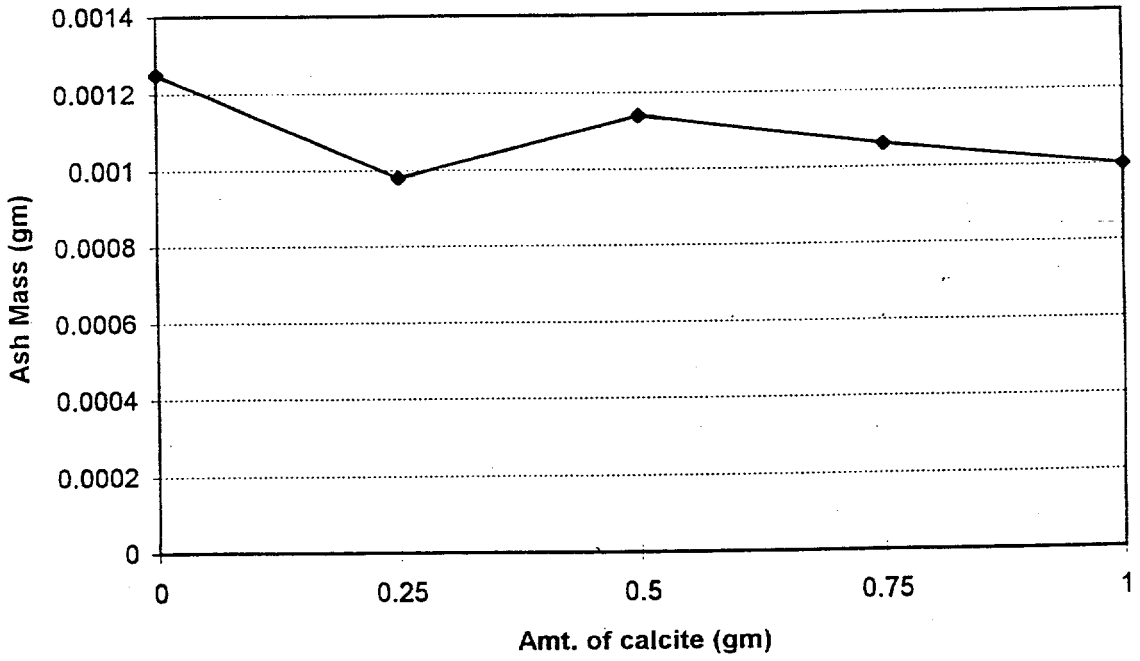

Figure 6-11 Ash yield at the filter vs. amount of calcite for calcite series.

Addition of calcite shows no significant effect on sodium aerosol yield. All the data points lay near the char #1 and char #2 data. In addition, the aerosol yield in terms of amount of calcite in the artificial char, Figure 6-11, does not show significant variation. Possible causes of this are: (1) the large size of the calcite particles, or (2) the poor reactivity of calcite towards sodium vapor.

In addition, unlike the pyrite and bentonite data, there is essentially no change in the mass on the intermediate stages. This indicates that all the additional calcite mass was appearing as particles in the preseparator. For the bentonite, the original particle size was small enough to place particles on these stages. For pyrite, the large original particles probably fragmented during char combustion.

7.0 Sodium Release and Capture Model

To provide a preliminary evaluation of the data presented above, a simple model was formulated. This model serves as a basis for more advanced model development and further interpretation of data developed during this project. The goal of the model is to describe the following features:

- The release of char bound sodium, assuming the sodium is always present at its equilibrium vapor pressure within the char, and assuming the all processes are transport limited.
- The capture of sodium by mineral inclusions that are present within the char.
- The capture of sodium by excluded mineral matter resident on the char surface.

Details are described in the following paragraphs.

7.1 Model Description

The model assumes a spherical char particle that has completed devolatilization. Since the organic sodium is released before the char reaches ignition temperature, free oxygen is assumed to be available throughout the interior surfaces of the particle. Sodium is assumed to be organically bound, *i.e.,* bound to carboxyl groups. Due to the molecular dispersion of the sodium throughout the char, no chemical reaction resistance to the sodium entering the vapor phase is assumed. Thus, at any point in the char, the partial pressure of the sodium is equal to the equilibrium pressure over the bound sodium at the local temperature. This holds at all points where sodium remains in the solid phase, but not where the sodium has become depleted.

Before including aluminosilicates in the model, we will discuss the implications of the assumptions listed above on sodium release behavior. This is illustrated in the following simplified example. Consider a spherical char particle that contains no mineral matter except molecularly dispersed sodium. As illustrated in Figure 7-1, initially sodium is present throughout the particle at its equilibrium partial pressure. Since the partial pressure of sodium at the surface of the particle is also at the equilibrium value, the vaporization rate will be governed by the diffusion film resistance between the surface of the particle and the free stream. This situation will hold only momentarily, however. Due to vaporization, the bound sodium in the shell near the surface will become depleted and the sodium will have to diffuse from within the particle to reach the surface, as is also shown in Figure 7-1. Thus, in general, the vaporization rate will be governed by the combination of the diffusion resistance in the char and the external film resistance. The depletion of sodium with time is represented by a shrinking core within which the equilibrium partial pressure of sodium is maintained. The diffusion can be considered to be fast compared to the rate of core shrinkage, so the problem can be treated as a quasi-steady-state solution. The instantaneous vaporization rate can then be evaluated as the rate at which sodium vapor arrives at the surface of the char particle.

As noted in the literature, this simplified picture must be modified to account for the absorption of sodium by aluminosilicates to form complexes. Once absorbed into these complexes, the sodium release will be delayed, if it occurs at all. These complexes will typically occur in two forms: (1) as discrete inclusions scattered within the char particle, and (2) as excluded mineral matter loosely attached to the char surface. In the work of Quann and Sarofim (1982) on the vaporization of refractory oxides, the inclusions were regarded as sources of refractory mineral vapor. Here they are regarded as sinks for sodium.

To accommodate this, the sodium release model is modified in the following two ways:

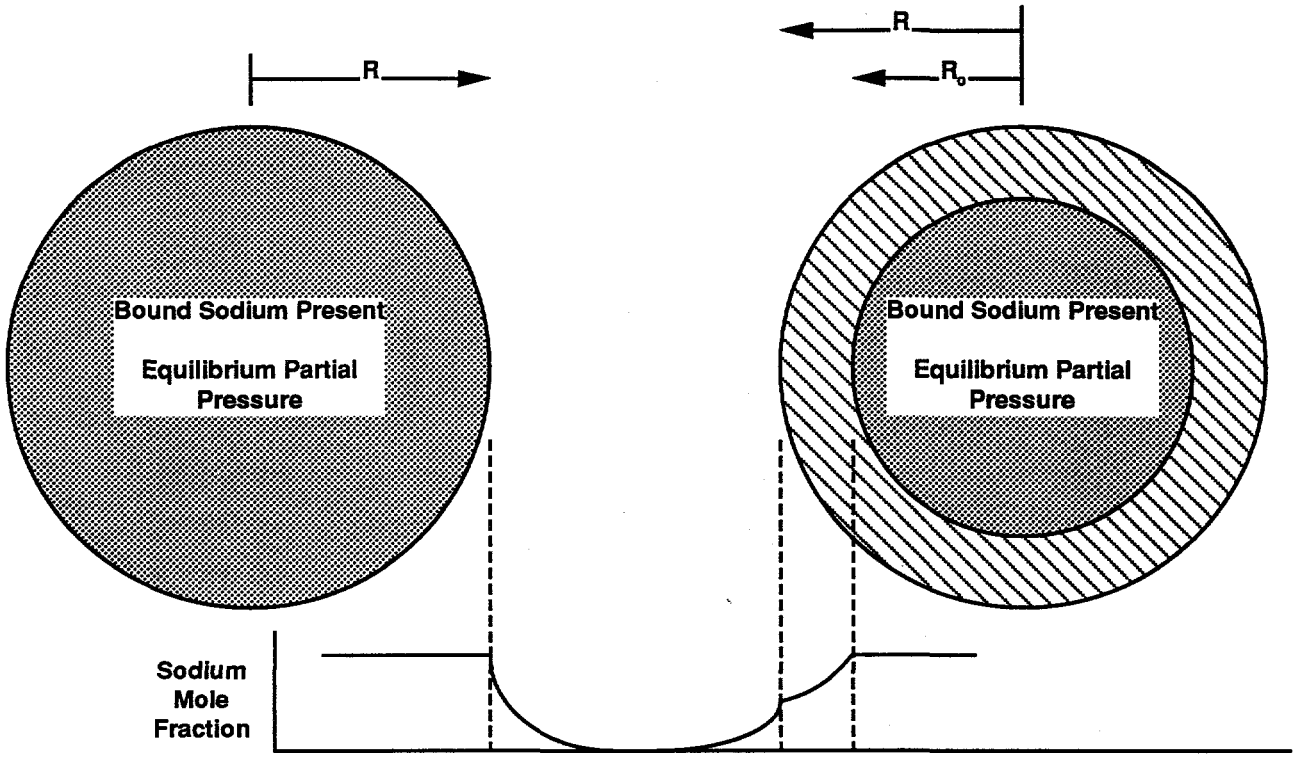

Char particle at start of sodium vaporization. The partial pressure is uniform, and the surface concentration of the sodium is also at the equilibrium value. Vaporization rate is governed by diffusion through the external gas film

Char particle partway into vaporization. Within core partial pressure remains uniform, but within shell the bound sodium is depleted. Vaporization rate is governed by Knudsen diffusion through shell and diffusion through the external gas film

Figure 7-1. Schematic of char particles showing sodium vapor profiles for two stages in the vaporization lifetime.

1. Aluminosilicate inclusions are assumed to be dispersed within the char matrix. Although their effect is local, the large number and uniform dispersion of these particles allows them to treated mathematically as a continuum sink of finite strength dispersed throughout the char. These will be active in both the shell region and in the equilibrium core illustrated in Figure 7-1.

2. Aluminosilicate particles at the edge of the char particle. These can act as sinks for sodium leaving the char particle. These can be handled mathematically by a modification of the boundary conditions at the char surface.

The next section discusses the mathematical formalism.

7.2 Model Formulation

For consistency, we have adopted as much of the nomenclature of Quann and Sarofim (1982) as possible. We first write and solve a conservation equation for sodium vapor within the shell region shown in Figure 7-1. Here the transport of sodium vapor is governed by the following equation:

$$cD_e \frac{1}{r^2} \frac{d}{dr}\left[r^2 \frac{dy_{Na}}{dr}\right] - \rho_{Na} V_{Na} = 0 \qquad (7\text{-}1)$$

where: c = molar density of total gas (kmoles/m^3)
D_e = Knudsen coefficient for diffusion of Na vapor in the porous char (m^2/s)
y_{Na} = mole fraction of Na in vapor
ρ_{Na} = number density of aluminosilicate inclusions (m^{-3})
V_{Na} = rate of absorption of Na by a single inclusion (kmoles/s)

If the mole fraction of sodium vapor at the surface of the inclusions is zero, then the rate of sodium transport to the inclusions will be governed by the rate of diffusion of sodium from the bulk of the char to the surface of the inclusions. This is calculated by integrating the diffusion equation around each inclusion. Assuming no local convective velocity, the transport rate is:

$$V_{Na} = 4\pi R_i c D_e y_{Na} \qquad (7\text{-}2)$$

where R_i is the radius of the inclusion, and y_{Na} is the mole fraction of sodium in the "free stream" vicinity near the inclusion.

Equation 7-1 can be transformed by the substitution $y_{Na} = f/r$ into the following form:

$$\frac{d^2 f}{dr^2} - \lambda^2 f = 0 \qquad (7\text{-}3)$$

where: $\lambda^2 = 4\pi R_i \rho_{Na}$

This has solutions: $f(r) = A \exp(\lambda r) + B \exp(-\lambda r)$, or

$$y_{Na}(r) = \frac{A R_O}{r} \exp(\lambda r) + \frac{B R_O}{r} \exp(-\lambda r) \qquad (7\text{-}4)$$

where A and B are constants. At the inner boundary the mole fraction of sodium is at the local

equilibrium value:

$$\text{at } r = R_o,\ y_{Na} = y_{Na,e} \tag{7-5}$$

The outside boundary condition represents an expression that a portion of the sodium flow arriving at the surface is absorbed by mineral particles and a portion is released as vapor. In words, this boundary condition is stated as:

$$\text{Na flow arriving at inner char surface} = \text{Flow absorbed at the surface} + \text{Flow leaving char particle} \tag{7-6}$$

If we define ε as the fraction of surface covered by minerals, then this boundary condition can be stated mathematically as:

$$0 = [1-\varepsilon]\, c\, D_e \frac{dy_{Na}}{dr} + \frac{D_o}{R} y_{Na} \quad \text{at } r=R \tag{7-7}$$

here, the gradient is on the char side of the surface, and D_O is the ordinary diffusivity. If the surface is entirely coated with aluminosilicate particles, then the surface concentration of sodium is zero, as expressed by:

$$\text{at } r=R,\ y_{Na}=0 \tag{7-8}$$

The assumption is made that the surface mineral matter is sufficiently well dispersed to act in a "finely speckled" absorber of sodium vapor. Here, the radial symmetry of the sodium vapor profile within the char particle is not disturbed, but both the surface concentration and the vapor flux leaving the char are influenced by the fraction of the surface that is covered by minerals. Thus, two solutions exist to this problem. These are approximated by considering the actual solution for the sodium vapor profile within the char to be a linear combination of the following two solutions:

1. $y_{Na,1}$ = solution subject to boundary condition (7-7). This corresponds to either zero coverage or partial coverage of the particle by minerals.

2. $y_{Na,2}$ = solution subject to boundary condition (7-8). This represents zero sodium concentration at the particle surface, which corresponds to complete coverage of the surface by minerals.

These individual solutions require substantial algebraic manipulation, but are straightforward, and are given in final form here:

$$y_{Na,1} = \frac{R_O\, y_{Na,e}}{r} \left\{ \left[1 - \frac{1}{1 + \frac{\lambda-M}{\lambda+M} \exp(-2\lambda R) \exp(2\lambda R_O)} \right] \frac{\exp(\lambda r)}{\exp(\lambda R_O)} \right\} + \left\{ \left[\frac{1}{1 + \frac{\lambda-M}{\lambda+M} \exp(-2\lambda R) \exp(2\lambda R_O)} \right] \frac{\exp(-\lambda r)}{\exp(-\lambda R_O)} \right\} \tag{7-9}$$

here, $$M = \frac{1}{R}\left[\frac{D_o}{c\,D_e\,[1-\varepsilon]} - 1\right]$$

and:

$$y_{Na,2} = \frac{R_O}{r}\left[\frac{\exp(\lambda R_O)}{1 - \exp(2\lambda R_O - 2\lambda R)}\right]\left[\exp(-\lambda r) - \exp(-2\lambda R)\exp(\lambda r)\right] \qquad (7\text{-}10)$$

From this solution, the instantaneous vaporization rate of sodium can be established. The rate at which sodium arrives at the surface from within the char is given as:

$$\text{Rate} = -4\pi R^2\, c\, D_e \frac{dy_{Na}}{dr} \qquad (7\text{-}11)$$

Of the vapor arriving at the surface, only the fraction (1 -ε) escapes, the remaining fraction being captured by the surface minerals. Thus, the final expression for the rate of escape of sodium vapor away from the particle is given by:

$$\text{Vaporization Rate} = 4\pi R^2 (1-\varepsilon)\, c\, D_e \frac{dy_{Na}}{dr} \qquad (7\text{-}12)$$

or in terms of the surface concentration (char side):

$$\text{Vaporization Rate} = 4\pi R (1-\varepsilon)\, c\, D_O \propto y_{Na,s} \qquad (7\text{-}13)$$

This completes the quasi-steady solution for sodium transport out of the particle. Equation 7-13 can be integrated over the time that sodium vaporization is active to yield the total kmoles of sodium that enter the vapor phase around the particle and form aerosol. If this value is normalized against the amount of organically-bound sodium initially present in the particle, the total fraction of original sodium that is vaporized can be obtained.

One additional conservation equation is needed for the bound sodium within the "unreacted" core. In this core, the vapor phase concentration of the sodium is at the local equilibrium value. Locally, however, the aluminosilicate inclusions will continue to absorb sodium out of the vapor phase, as outlined above. This will be replenished by the organically-bound sodium. Thus, as time progresses, the concentration of bound sodium within the core will decrease, even though there is no diffusion of sodium to the boundary of the core. The rate at which the boundary of the core recedes is then set to match the flux of sodium entering the shell where $r>R_O$.

Within the unreacted core, the mass fraction of sodium in the char (x_{Na}) will be governed by the following equation:

$$\frac{dx_{Na}}{dt} = \left(\frac{\rho_{Na}}{\rho_c}\right) M_{Na}\,(4\pi R_i)\, c\, D_e\, y_{Na,e} \qquad (7\text{-}14)$$

where ρ_c = char bulk density (kg/m^3), and M_{Na} = molar mass of Na (kg/kmole). The surface of the unreacted core must recede at a rate which supplies the correct amount of sodium to the shell layer. Thus, the rate at which the surface recedes is set by a sodium flux balance:

$$\frac{dR_O}{dt} = \frac{M_{Na}\, c\, D_e}{x_{Na}\rho_c}\left[\frac{dy_{Na}}{dr}\right] \qquad (7\text{-}15)$$

where dy_{Na}/dr is evaluated from the shell at the inner surface. Note that as the bound sodium is depleted, the shrinking rate of the core will increase to provide the needed sodium for shell. Thus, the shrinkage rate of the core accelerates until the core is completely consumed. At this point, there is no free sodium left in the particle; sodium has either vaporized or has been complexed into aluminosilicate minerals.

7.3 Model Results

The model was coded and tested on the Illinois coal. Before the data plots are presented, some features of the process need discussion.

After devolatilization, the char particle heats towards its steady-state combustion temperature. At approximately 1200-1300 K, the particle quickly goes from a temperature where the equilibrium sodium vapor pressure is negligible to a temperature where it is at one atmosphere. This shows that the sodium vaporization occurs under non-isothermal conditions, although the rapid rate of sodium diffusion relative to particle heating suggests that the quasi steady-state formulation for the sodium vaporization portion of the problem is appropriate. It also illustrates the two-stage release pattern for the sodium: (1) an early rapid release of organically-bound sodium, and (2) a more delayed release of acid-washable sodium, and sodium that was complexed into clay minerals during the organic sodium vaporization.

The conditions reported for the present calculations are as follows: Coal: 8.7% ash, 12% H_2O, 33.5% volatile matter. Elemental sodium represents 0.82% of the ash. For purposes of calculation, the char particle is presumed to consist of the fixed carbon from the proximate analysis, along with the ash. This establishes the mass fraction of sodium and other minerals in the char at the start of char combustion. The char particle diameter was 25 μm.

Figure 7-2 shows the fraction of sodium released into the vapor phase as a function of percent coverage of the char surface. If no mineral inclusions are present in the char, the fraction of sodium released varies proportionally with the fraction of the surface *uncovered* by the surface minerals. For illustration, three cases are shown in which the fixed amount of included mineral matter is divided into a dispersion of monosized particles. As inclusion particle size is reduced (and number density is increased), more of the sodium is retained by the char and less reaches the vapor phase.

The curvature shown by the lines in Figure 7-2 is deceptively complex, and is the result of the combination of two factors:

1. With increased surface coverage, the sodium concentration at the particle surface is reduced. This tends to shorten the time needed to complete sodium release from within the particle. This decreases the time available for the inclusions to absorb sodium, and would tend to increase the amount of sodium vaporized at a given surface coverage. This would tend to make the curves bow upward.

2. Alternately, the reduced surface concentration of sodium will reduce the sodium vapor concentrations throughout the char particle. This will reduce the amount of sodium absorbed into the inclusions. This will reduce the amount of sodium vaporized at a given surface coverage. This tends to make the curves bow downward.

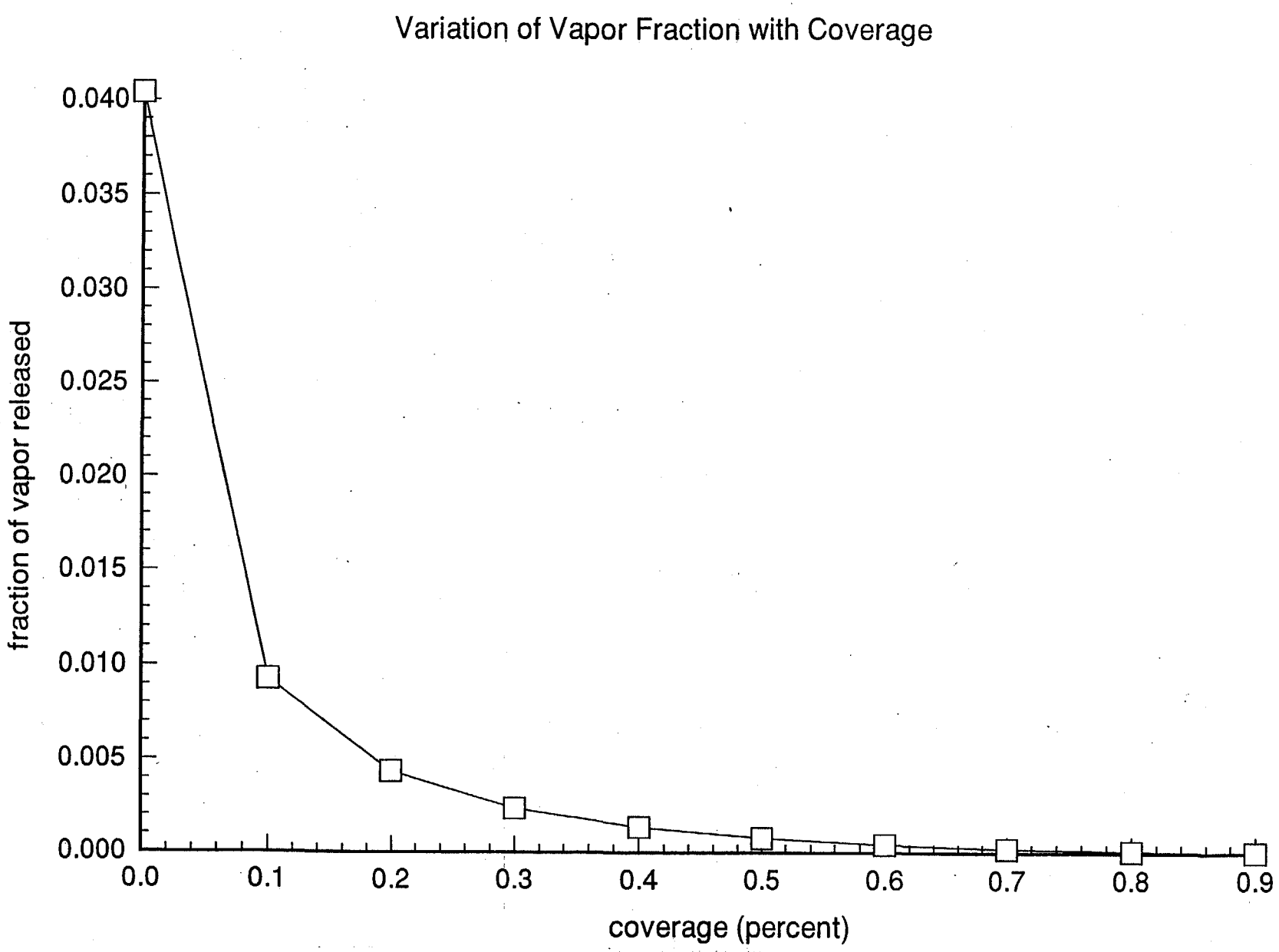

Figure 7-2. Variation of sodium vaporization with fraction of surface covered by excluded mineral matter. Inclusion size is 0.5μm.

Both of these factors combine to yield the behavior shown in Figure 2: A 50% coverage of the surface by minerals leads to a much greater than 50% reduction in sodium vaporization.

Figures 7-3 (a and b) shows the fraction of sodium vaporized as a function of aluminosilicate inclusion radius for 50% surface coverage. (Figures 7-3a and 7-3b are for the same conditions, but cover different ranges of inclusion radius.) The entire plot is for a constant value of inclusion mass, so a reduction in inclusion radius must be matched by an increase in inclusion number density. Thus, reduced inclusion diameter leads to greater inclusion surface area and higher sodium capture efficiencies. Note that for realistic-sized inclusions (0.1-1.0 μm), the amount of sodium released varies proportionally with inclusion size. The vaporization reaches asymptotic behavior only when the inclusion size approaches unrealistic values.

7-4 Discussion

Although the model is not yet completely refined, it does permit the drawing of preliminary conclusions. First, consistent with the suggestion of Gallagher (1992), the proximity of the aluminosilicate inclusions to the sodium being vaporized has a significant influence on the fraction of sodium that leaves the char particle and enters the vapor phase. Second, the potential for the capture of sodium by other minerals leads to potential complex sodium release behavior. Some sodium will be released during primary vaporization, while the release of additional sodium may be delayed due to its capture by aluminosilicate minerals, or by the fact that it was originally bound with other minerals.

In the model, sodium release occurs early in the char combustion sequence, and the fraction of sodium reaching the gas phase depends strongly on the coverage of the char surface by excluded minerals. Thus, the pooling of minerals on the char surface as the char is burned away will not influence the process since the primary sodium vaporization will have already been finished. This means that it is the *initial* state of the char surface that is key to sodium capture by excluded mineral matter.

One limitation of the model is the assumption that transport processes, along with equilibrium chemistry, govern the sodium release rate. For some chars, however, the release of sodium is kinetically-controlled (Srinivasachar *et al.*, 1990a). Also, Gallagher (1992) suggests that a kinetic component may enter into the aluminosilicate capture process. Both of these features need to be included in the model.

Both of these factors combine to yield the behavior shown in Figure 2: A 50% coverage of the surface by minerals leads to a much greater than 50% reduction in sodium vaporization.

Figures 7-3 (a and b) shows the fraction of sodium vaporized as a function of aluminosilicate inclusion radius for 50% surface coverage. (Figures 7-3a and 7-3b are for the same conditions, but cover different ranges of inclusion radius.) The entire plot is for a constant value of inclusion mass, so a reduction in inclusion radius must be matched by an increase in inclusion number density. Thus, reduced inclusion diameter leads to greater inclusion surface area and higher sodium capture efficiencies. Note that for realistic-sized inclusions (0.1-1.0 μm), the amount of sodium released varies proportionally with inclusion size. The vaporization reaches asymptotic behavior only when the inclusion size approaches unrealistic values.

7.4 Discussion

Although the model is not yet completely refined, it does permit the drawing of preliminary conclusions. First, consistent with the suggestion of Gallagher (1992), the proximity of the aluminosilicate inclusions to the sodium being vaporized has a significant influence on the fraction of sodium that leaves the char particle and enters the vapor phase. Second, the potential for the capture of sodium by other minerals leads to potential complex sodium release behavior. Some sodium will be released during primary vaporization, while the release of additional sodium may be delayed due to its capture by aluminosilicate minerals, or by the fact that it was originally bound with other minerals.

In the model, sodium release occurs early in the char combustion sequence, and the fraction of sodium reaching the gas phase depends strongly on the coverage of the char surface by excluded minerals. Thus, the pooling of minerals on the char surface as the char is burned away will not influence the process since the primary sodium vaporization will have already been finished. This means that it is the *initial* state of the char surface that is key to sodium capture by excluded mineral matter.

One limitation of the model is the assumption that transport processes, along with equilibrium chemistry, govern the sodium release rate. For some chars, however, the release of sodium is kinetically-controlled (Srinivasachar *et al.*, 1990a). Also, Gallagher (1992) suggests that a kinetic component may enter into the aluminosilicate capture process. Both of these features need to be included in the model.

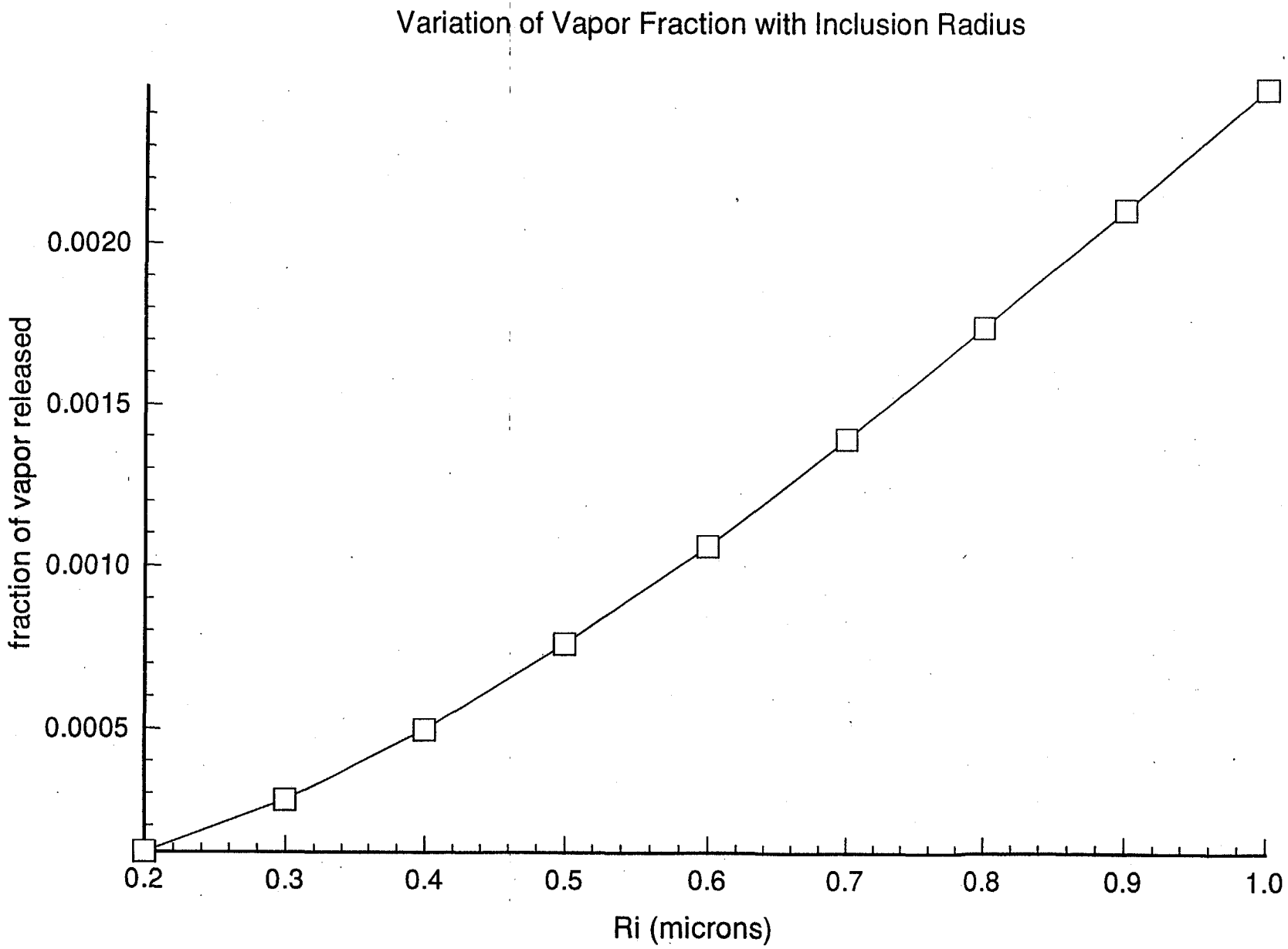

Figure 7-3a. Variation of sodium vaporization with inclusion size for 50% surface coverage. Range is 0.2 - 1.0 μm inclusion size.

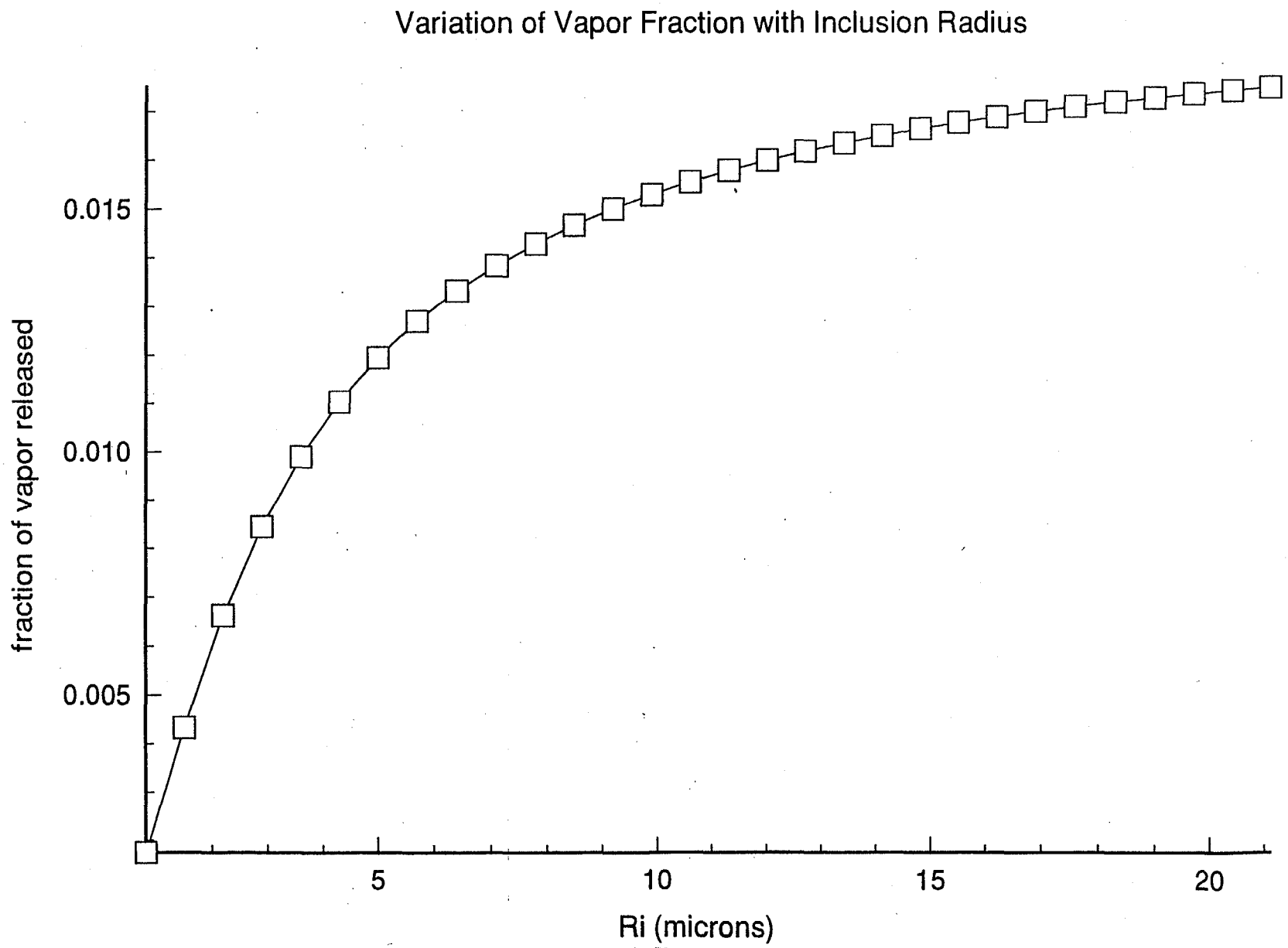

Figure 7-3b. Variation of sodium vaporization with inclusion size for 50% surface coverage. Range is 1.0 - 20.0 μm inclusion size.

8.0 Summary

The research reported here shows that various forms of coal treatment can significantly change ash characteristics. While none of the treatments affected the bulk of the residual ash size distribution significantly, the yield of the ash aerosol mode (d<0.5 μm) and fine residual ash mode (1-4 μm) are changed by the treatments. Specific findings include:

- High alkali coals that are either cleaned or sized by aerodynamic classification tend to generate significantly more aerosol upon combustion that the parent coals.

- Aerosol yields from high alkali coals are suppressed when a small amount of excluded mineral matter extracted during cleaning is mechanically mixed into the coal. This suggests that excluded mineral matter will suppress aerosol yields.

- For low-alkali coals, however, the identical coal cleaning process does not change aerosol yields, although it does lead to an increase in the 1 μm residual ash mode.

- Particle sizing (specifically the firing of larger-sized particles) leads to an increase in aerosol yields for the low alkali coals. Evidence suggests that the sized fraction requires longer to burn, which yields more time for vaporization of refractory oxides. Note that such a trend may not hold for alkali-rich coals where longer burning times may lead to more alkali capture by aluminosilicates. Again, the refractory oxide vapors do not likely react with aluminosilicates.

- The yield of particles in the 1-4 μm range exceeds that predicted by the breakup model. This mode becomes very significant when the original coal particles have small diameters, and is insignificant for larger-sized coal particles. This suggests that this mode is generated by a process that responds to the specific surface area of the original coal. In one interpretation, these particles result from the release of fine inclusions near the surface of the coal during the initial stages of char combustion. This release occurs only briefly before these particles become absorbed into a surface melt. Thus, one obtains a strong dependance on the initial surface/volume ratio.

- As noted above, cleaning of low-alkali coals leads to an increase in the 1-4 μm mode. Aerosol yields from these coals are dominated by vaporized suboxides and elements derived from refractory oxides. These should not be absorbed by excluded mineral matter since aluminosilicates are unlikely to react with these vapors. Thus, no change in aerosol yield is expected. However, the cleaning process will strip the surface clean of excluded mineral matter. This may allow small inclusions near the surface to be liberated to a greater degree during the initial stages of burnout than would occur for the straight coal. This would lead to the increased 1-4 μm mode.

- In artificial char experiments, bentonite was demonstrated to be active towards alkali metal capture. Also, pyrite inclusions were observed to fragment during char combustion, but no evidence of the generation of an aerosol was noted.

- Residual ash breakup number is insensitive to temperature or free stream oxygen concentration, but tends to increase for lower-rank fuels (as previously noted in the literature).

A preliminary model of the alkali vaporization/capture process was developed that is based on mass transport control. While this model replicates some of the trends noted in the experiments, it does not yet include finite rate chemistry, which is known to influence some results.

9.0 References

Baxter, L. L. *Prog. Energy Combust. Sci.* 1990, **16,** 261.

Boni, A. A. Transformations of inorganic coal constitutents in combustion systems. Final Report, DOE Contract No. DE-AC22-86PC90751, Physical Sciences Technology Company, Andover MA (1992).

Damle, A. S., Ensor, D. S., and Ranade, M. B. *Aerosol Sci. Technol.* 1982, **1,** 119.

Field, M. A., Gill, D. W., Morgan, B. B., and Hawksley, P. G. W. *Combustion of Pulverized Coal.* 1967, The British Coal Utilization Research Association.

Flagen, R. C. *Seventeenth Symposium (International) on Combustion* 1979, The Combustion Institute, p. 97.

Flagen, R. C., and Friedlander, S. K. *Recent Developments in Aerosol Science.* (D. T. Shaw, Ed.) 1978, Wiley, Chapter 2.

Friedlander, S. K. *Smoke, Dust and Haze* 1977, Wiley.

Gallagher, N. B. Alkali Metal Partitioning in a Pulverized Coal Combustion Environment. Ph.D. Dissertation, Department of Chemical Engineering, The University of Arizona, Tucson, AZ (1992).

Gallagher, N. B., Bool, L. E., Peterson, T. W., and Wendt, J. O. L. "Fundamental Study of Alkali Evolution in a Self-Sustained Laboratory Pulverized Coal Combustor," in *Transformations of Inorganic Coal Constitutents in Combustion Systems.* Quarterly Report No. 18, DOE Contract No. DE-AC22-86PC90751, Physical Science Technology Company (1991).

Gladney, E. S., Small, J. A., Gordon, G. E., and Zoller, W. H. *Atmos. Environ.* 1976, **10,** 1071.

Graham, K. A., Sarofim, A. F., and Beér, J. M. "Vaporization Results and Modeling," in *Transformations of Inorganic Coal Constitutents in Combustion Systems.* Quarterly Report No. 17, DOE Contract No. DE-AC22-86PC90751, Physical Science Technology Company (1991).

Gupta, R. J. *Radiative Transfer Due to Fly Ash in Coal Fired Furnaces*, Ph.D. Dissertation 1983, University of Newcastle.

Helble, J. J., and Sarofim, A. F. *Combust. Flame* 1989, **76,** 183.

Helble, J. J., Srinivasachar, S., and Boni, A. A. *Prog. Energy Combust. Sci.* 1990, **16,** 267.

Huffman, G. P., Huggins, F. E., Shah, N., and Shah, A. *Prog. Energy Combust. Sci.* 1990, **16,** 267.

Kang, S., Helble J. J., Sarofim A. F., and Beér, J. M. *Twenty-Second Symposium (International) on Combustion* 1988, The Combustion Institute, p. 231.

Kramlich, J. C., and Newton, G. H. *Fuel Proc. Technol.* 1994, **37,** 143.

Linak, W. P., and Peterson, T. W. *Aerosol Sci. Technol.* 1984, **3,** 77.

Linak, W. P., and Peterson, T. W. *Twenty-First Symposium (International) on Combustion* 1986, The Combustion Institute, p. 399.

Linak, W. P., and Wendt, J. O. L. *Prog. Energy Combust.* Sci. 1993, **19,** 145.

Linder, E. R., and Wall, T. F. *Twenty-Third Symposium (International) on Combustion* 1990, The Combustion Institute, p. 1313.

McCain, J. D., Gooch J. P., and Smith, W. B. *Journal of the Air Pollution Control Association* 1975, **25,** 117.

Mitchell, R. E. *Twenty-Third Symposium (International) on Combustion* 1990, The Combustion Institute, p. 1297.

Morrow, P. E. *Amer. Ind. Hyg. Assoc. J.* 1964, **25,** 213.

Neville, M., Quann, R. J., Haynes, B. S., and Sarofim, A. F. *Eighteenth Symposium (International) on Combustion* 1981, The Combustion Institute, p. 1267.

Park, J. Development of Artificial Char for Chal Mineral Transformation Studies. MS Thesis, Department of Mechanical Engineering, University of Washington, Seattle, WA (1995).

Quann, R., Neville, J. M., and Sarofim A. F. *Combust. Sci. Technol.* 1990, **74,** 245.

Quann, R. J., and Sarofim, A. F. *Nineteenth Symposium (International) on Combustion* 1982,

The Combustion Institute, p. 1429.
Raask, E. *Mineral Impurities in Coal Combustion: Behavior, Problems, and Remedial Measures*, Hemisphere (1985).
Sarofim, A. F., Howard, J. B., and Padia, A. S. *Combust. Sci. Technol.*, 1977 **16,** 187.
Senior, C. L., and Flagen, R. C. *Aerosol. Sci. Technol.* 1982, **1,** 371.
Smith, A. H., and Goeden, H. M. *Combust. Sci. Technol.* 1990, **74,** 51.
Srinivasachar, S., Helble, J. J., Ham, D. O., and Domazetis, G. *Prog. Energy Combust. Sci.* 1990a, **16,** 303.
Srinivasachar, S., Helble, J. J., and Boni, A. A. *Prog. Energy Combust. Sci.* 1990b, **16,** 281.
Walsh, P. M., Sayre, A. N., Loehden, D. O., Monroe, L. S., Beér, J. M., and Sarofim, A. F. *Prog. Energy Combust. Sci.* 1990, **16,** 327.
Yuh, S. J., and Wolf, E. E. *Fuel* 1984, **63,** 1604.